

Thesis for Degree of Doctor of Philosophy

**Fabrication of high-quality large-size graphene
and TEM observation of graphene liquid cell**

(高品質大面積グラフェンの合成法の確立と
グラフェン液体セルの透過型電子顕微鏡観察)

Yuki Sasaki

佐々木 祐生

Department of Chemistry, Graduate School of Science

Nagoya University

2016

Chapter 1	1
1. General introduction	1
1-1. Nano-carbon	1
1-2. Graphene.....	3
1-2-1. Electronic properties of graphene	4
1-2-2. Optical properties of graphene	6
1-3. Graphene synthesis	7
1-3-1. Mechanical exfoliation	8
1-3-2. CVD.....	9
1-4. Water	9
1-5. TEM	10
1-5-1. Graphene in TEM observation	11
1-5-2. Environmental cell	12
1-5-3. TEM observation of liquids	13
1-6. Summary.....	14
1-7. References	16
Chapter 2	21
2. Graphene growth	21
2-1. Introduction	21
2-2. Preparation and apparatus.....	23
2-3. Growth mechanism	25
2-4. Pretreatment.....	27
2-5. Reactions	27
2-6. Experimental.....	28
2-7. Results and discussion.....	31
2-8. Conclusion	39
2-9. References	41
Chapter 3	43
3. Graphene transfer and preparation of graphene-sandwiched structure	43
3-1. Introduction	43
3-2. Transfer with polymer support	45
3-3. Transfer without support	46

3-4. Experiment.....	47
3-5. Results of the direct transfer method	50
3-6. Preparation of the grapheme-sandwiched structure.....	53
3-7. Results of the grapheme-sandwiched structure	54
3-8. Conclusion.....	57
3-9. References	58
Chapter 4.....	60
4. TEM observation for liquids.....	60
4-1. Introduction	60
4-2. Water at room temperature	62
4-3. Water at 77 K.....	72
4-4. Aqueous solution of iron nitride	78
4-5. Aqueous solution of calcium chloride.....	87
4-6. Organic solvents.....	90
4-6-1. Trichloromethane	91
4-6-2. Methanol.....	95
4-6-3. 2-Propyl alcohol.....	100
4-7. Phase transitions of liquids.....	105
4-8. DFT calculation of ice with gold	115
4-9. Conclusion.....	120
4-10. References.....	122

Preface

The studies described in this thesis has been carried out under the supervision of Professor Hisanori Shinohara at Department of Chemistry, Graduate School of Science, Nagoya University during April 2013 to January 2016. The present studies focus on the endohedral chemistry of graphene, in particular, TEM observations of liquids and solution-based materials.

Firstly, I would like to express my sincerest gratitude to my supervisor Prof. Hisanori Shinohara for his continuous support of my PhD study and related research, as well as his discussions, encouragement, and patience. Through my research activities in the Shinohara Lab, my interest in science grew progressively until I decided to pursue my original research. I am very lucky to have had Prof. Shinohara as my supervisor, and he will always be my role model.

My sincere thanks also go to Asst. Prof. Haruka Omachi, who is an advisor and superior, for his support and motivation. I could not have imagined having a better advisor and mentor for my PhD study. He was always there whenever I need his help. I wish him success in his future endeavors. I would like to thank Assoc. Prof. Ryo Kitaura and Assoc. Prof. Yasumitsu Miyata (currently at Tokyo Metropolitan University, Japan)

for their insightful comments and challenging questions about my research. Their insights expanded my intellectual views, and helped me improve the qualities of my prepared manuscripts.

I would like to express my deep acknowledgement to all the members in the Shinohara Lab for the fruitful discussions. Dr. Yusuke Nakanishi was a good companion at all times. He always reviewed my considerations and inquiries with smiles, and his kind supports improved the quality of my reports. I am very grateful to Dr. Takashi Yamaguchi for his excellent guidance on performing TEM observations; I learnt from him the fundamentals of TEM, a key technique that will continue to be a key aspect of my future research. Special thanks go to our secretaries Ms. Ogawa and Ms. Hattori, who helped me in many respects.

My PhD study was supported by two scholarships. I am most grateful to the Japan Society for the Promotion of Science (JSPS) for a Research Fellowship for Young Scientists (DC1). I also received financial aid from the Nagoya University Program for Leading Graduate Schools “Integrative Graduate Education and Research Program in Green Natural Sciences (IGER)” of MEXT (Japan). These scholarships allowed me to concentrate on my research activities. Special thanks goes to Enago for editing this thesis in English. They reviewed and modified virtually all parts of this thesis, and their kind cooperation improved the fluency and clarity of the contents.

Last but not the least, I would like to thank my family for supporting me spiritually and financially throughout the writing of this thesis and my life in general. I could not have completed my studies without their support and motivation. In particular, my parents have always given their unreserved love and care to me. I am very grateful for their support.

Yuki Sasaki

Department of Chemistry, Graduate School of Science

Nagoya University

January 2016

Chapter 1

1. General introduction

1-1. Nano-carbon

Nano-carbon materials are low-dimensional carbon clusters such as fullerenes, carbon nanotubes, and graphene. Since fullerene C_{60} was discovered by Kroto in 1985^[1], many people have been attracted to understanding low-dimensional carbon structures and their physical properties^[2-4].

Nano-carbon materials exhibit the various structures shown in Figure 1-1, each of which possesses quite different properties. Fullerene C_{60} has a soccer ball structure^[1], as shown in Figure 1-1 (a). C_{60} is the smallest size carbon cage because it has to satisfy the isolated pentagon rule^[5-7]. The most interesting point for the application of fullerenes is that the carbon cage of fullerenes can encapsulate some atoms inside its internal space. For the interior atom, it is placed in isolated zero-dimensional space. Of course, most internal atoms bond with the carbon cage; however, the less interactive atoms or molecules behave as if they are free-standing in vacuum^[8-10].

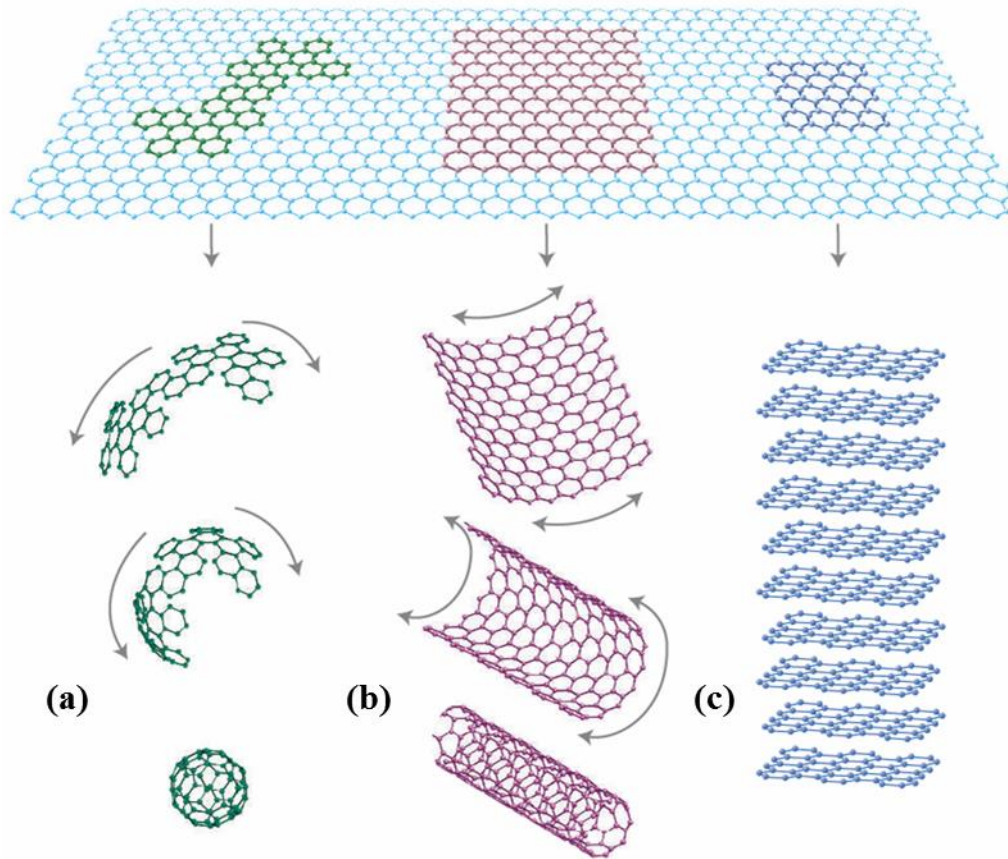


Figure 1-1: Structural images of nano-carbon materials. Fullerene C₆₀, a carbon nanotube, and graphene are shown in (a), (b), and (c), respectively^[11].

On the other hand, carbon nanotubes (CNTs) have a test-tube-like structure, as shown in Figure 1-1 (b)^[2, 12-14]. Interestingly, CNTs show various electronic properties that depend on their structure^[15-17]; therefore, they are expected to be used in thin-film transistors^[18-20]. The way in which the hexagonal carbon network film of graphene is rolled into a CNT is shown Figure 1-1 (c). In recent research, CNTs have not only been applied in electronic devices, but also their inner space has been employed as a nano-sized reactor^[21-27].

1-2. Graphene

Graphene is a monolayer of graphite consisting of a hexagonal network of carbon lying in one plane, as shown in Figure 1-2^[11, 28-29]. Since graphite is assembled from graphene not by chemical bonding but by van der Waals interactions, graphene can be easily exfoliated from bulk graphite^[28]. Graphite and graphene show differences in their electronic,^[30] optical, and mechanical properties because they have different electronic dispersion relations^[31-34].

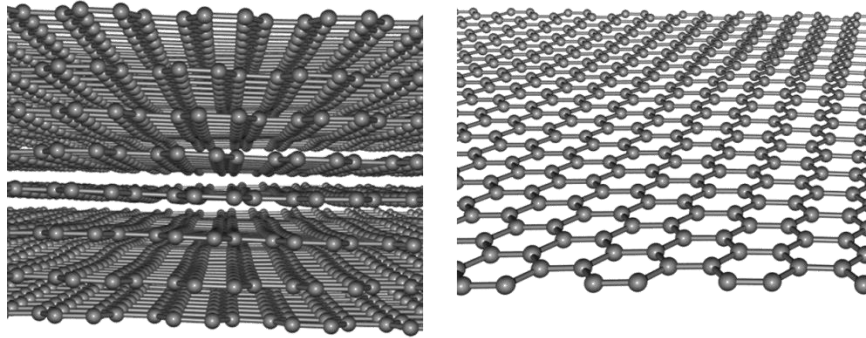


Figure 1-2: Structural images of graphite (left) and graphene (right).

Various unique physical properties of graphene have been suggested by calculations performed by many researchers^[32], but it was not expected that two-dimensional materials could be stable in air before they were actually found in 2004 when the first experimental report about the electronic properties of graphene was published by Geim and Novoselov^[28]. In this paper, graphene was prepared on a SiO_2 substrate by mechanical exfoliation using scotch tape. This was the first experimental demonstration of the 2D crystal. As a consequence, this report spread quickly and had a great impact all over the world. In 2010, Geim and Novoselov were awarded the Nobel Prize for

their work on the confirmation of the properties of graphene. In recent times, many papers relating to graphene are being published every day.

The 2D carbon hexagonal network configuration makes graphene strong and stable. Comparing monolayer graphene with steel of the same thickness, graphene has a breaking strength 200 times that of steel^[30]. It has even been reported that a $1 \times 1 \text{ m}^2$ graphene monolayer can support a cat. Infinitely repeating sp^2 bonds without dangling bonds make graphene chemically stable, and the remaining p orbital electrons behave as free electrons^[29, 32-33]. These free electrons can be regarded as zero-mass Dirac electrons.

1-2-1. Electronic properties of graphene

Graphene has two carbon atoms, A and B, in the unit cell, as shown in Figure 1-3. The coordinates of other atoms are described by the addition of a translation vector^[35].

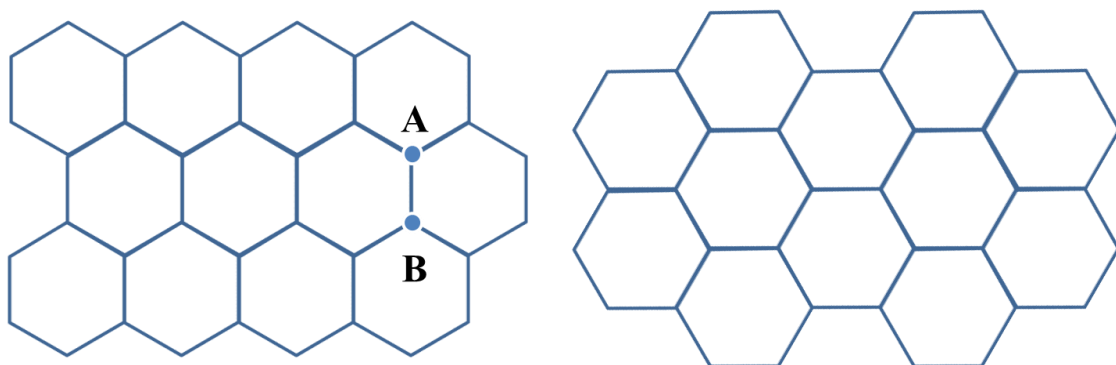


Figure 1-3: Graphene unit cell (left) and its reciprocal lattice images (right).

The π -electrons on the carbon atoms are assumed to be bound strongly by each carbon atom (tight binding method), and the repetition of A and B can be approximated by Bloch functions; the specific functions can be described as follows:

$$\Psi(\mathbf{k}, \mathbf{r}) = C_A(\mathbf{k})\Phi_A(\mathbf{k}, \mathbf{r}) + C_B(\mathbf{k})\Phi_B(\mathbf{k}, \mathbf{r}) \quad (1)$$

$$\Phi_A(\mathbf{k}, \mathbf{r}) = \frac{1}{\sqrt{N}} \sum_{\mathbf{R} \in A} e^{i\mathbf{k}\mathbf{R}} \varphi(\mathbf{r} - \mathbf{R}), \Phi_B(\mathbf{k}, \mathbf{r}) = \frac{1}{\sqrt{N}} \sum_{\mathbf{R} \in B} e^{i\mathbf{k}\mathbf{R}} \varphi(\mathbf{r} - \mathbf{R}) \quad (2)$$

In these equations, $\varphi(\mathbf{r} - \mathbf{R})$ represents the wave function of the π -electrons localized on the carbon atom placed in position \mathbf{R} and N is the number of the crystal lattices. By solving the determinant $|H - ES| = 0$ using the Eigen function, it is possible to determine the energy E . Details will be omitted, but E can be expressed by the following equation:

$$E = \pm \gamma_0 \sqrt{1 + 4 \cos \frac{ak_x}{2} \cos \frac{\sqrt{3}ak_y}{2} + 4(\cos \frac{ak_x}{2})^2} \quad (3)$$

Here, a is the lattice constant of graphene (0.234 nm), and the binding constant γ_0 is approximately 3 eV. According to equation (3), the relation between E and k is as shown in Figure1-4.

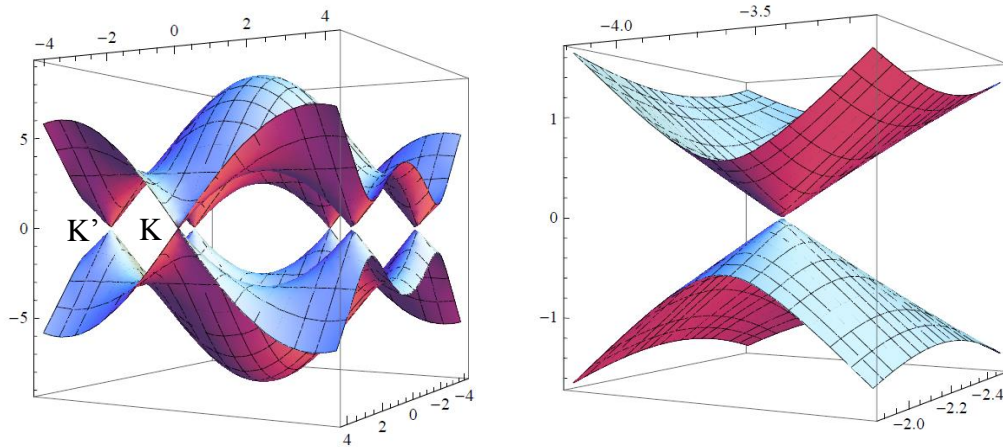


Figure 1-4: Energy band structure of graphene (left) and enlarged view focusing on the K-point (right). The horizontal axis shows E and the vertical axis shows k .

The contact of the upper and lower bands at points K and K' is confirmed in Figure 1-4, which is in agreement with the half-metallic behavior of single-layer graphene. The gradient of the band, E/k , in the vicinity of the K -point is linear according to the enlarged view of Figure 1-4. It suggests that electrons near the Fermi energy continue to move at a constant speed as zero-mass electrons. The constant speed of the electrons is approximately 10^6 m/s^[35-36].

1-2-2. Optical properties of graphene

Surprisingly, graphene can be observed by eye despite its atomic thickness^[31, 37]. Light absorption is generally caused by optical excitation from the valence band to the conduction band, and the vertical light absorption rate is proportional to the real part of dynamic conductivity, which is usually given by a function that depends on frequency.

However, the electronic conductivity of graphene does not depend on scattering frequency, τ , in the vicinity of the graphene's Dirac point. Considering that dynamic conductance and electronic conductivity are described in the same dimension, electronic conductivity should depend on τ if dynamic conductance is dependent on frequency. This is inconsistent; therefore, dynamic conductance should be a constant that does not depend on frequency. Thus, the visible light absorption rate of single-layer graphene is approximately 2.3%. This result can be predicted from the fact that the Dirac cone is linear. Moving away from the Dirac point (i.e., the energy of the excitation light is high), the visible light absorption rate of single-layer graphene starts to become dependent on the frequency and the band structure of graphene ceases to be linear. In contrast, the absorption rate for two-layer graphene dramatically increases after exceeding a threshold value of the frequency, γ . Absorption in the visible light region of multi-layer graphene has a value that increases in discrete steps according to the number of layers; it has been demonstrated to increase by 2.3% each time the number of layers increases. This is a surprising result as the absorption rate of 2.3% seems too large to have arisen from a substance with a thickness of only one layer of atoms.

1-3. **Graphene synthesis**

Having a simple structure, graphene has been successfully synthesized by many methods^[28, 38-42]. It is usually synthesized by three main methods: chemical vapor deposition (CVD) growth on a metal substrate^[38-39], mechanical exfoliation from graphite^[28], and segregation from a SiC substrate. Mechanically exfoliated graphene^[40-41] has high crystallinity but small-sized domains, whereas CVD graphene

has large-sized domains but is not generally of high quality^[38, 43-44]. Graphene segregated from a SiC surface was formed by epitaxial growth through reduction of the SiC substrate. Epitaxial growth of graphene can be used to control its structure and orientation; for example, graphene nanoribbons can be grown on SiC steps. Actually, well-controlled growth of graphene on SiC substrates has been shown previously to yield excellent physical properties, approaching those predicted theoretically^[40-41].

In this work, preparation of highly crystalline and large-scale graphene suspended on a transmission electron microscopy (TEM) grid was required. Therefore, CVD growth was chosen and a new method was developed that could produce highly crystalline, large domains of graphene.

1-3-1. Mechanical exfoliation

In the previously described work by Novoselov *et al.*, repeated exfoliation of graphite with scotch tape yielded several-layer or single-layer graphene^[28]. Previously, graphene was deposited on a silicon substrate by dissolving the scotch tape attached to the graphene pieces, but a more recent method is known in which directly attaching the tape to a silicon substrate and pulling is enough to obtain graphene on a silicon substrate. It is possible to obtain relatively large crystals by the development of this simple method, which does not involve solution. Now, pieces of graphene with sizes on the order of 100 μm can be produced, and larger sizes are becoming possible as the development of polymer stamping methods with PDMS progresses^[45]. Compared with the CVD method, domain sizes produced by the above methods are still small; however, they are inexpensive and high-crystallinity graphene can be obtained easily.

1-3-2. CVD

CVD is a method that results in epitaxial growth on the surface of a metal substrate^[38, 43-44, 46-50]. Various metal substrates work as a catalyst for decomposing many types of carbon sources. The usual choices for metal substrates are nickel and copper. The two metal catalysts have a large difference in growth mechanisms. Nickel can dissolve carbon atoms in its structure at high temperature, but they easily segregate into graphene layers on the substrate at low temperature^[47]. On the other hand, copper cannot dissolve so many carbon atoms, even at high temperature^[47]. Therefore, graphene on the copper substrate is grown through surface reaction. The number of layers of graphene is roughly controlled by utilizing this difference in CVD growth mechanism.

1-4. Water

Water, with the chemical formula H_2O , is a colorless, transparent, tasteless, and odorless fluid, which forms the world's oceans and rain; water is the major constituent of fluids on Earth. It is known that water molecules form strong hydrogen bonds with each other, which cause many differences in the physical properties of water compared to other liquids with weak or absent hydrogen bonds^[51]. For example, the phase diagram of water is shown in Figure 1-6^[52]. The phase transition temperature for the conversion of liquids to solids usually increases with pressure. For water, however, the phase transition temperature for the conversion of liquid water to ice decreases as the pressure increases. This phenomenon is explained by the effects of hydrogen bonding.

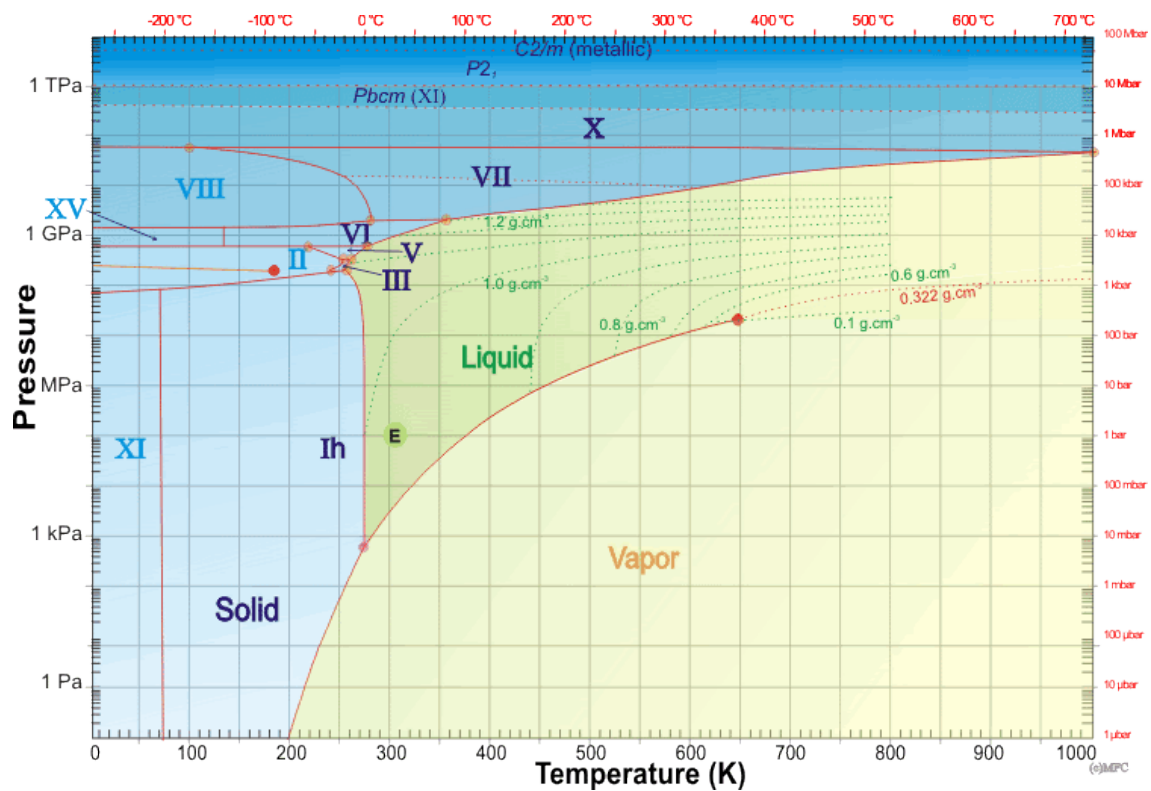


Figure 1-6: Phase diagram of water^[52].

Water as a solvent can dissolve many types of ionic solids and polar liquids. However, it is not clear how these crystals or fluids dissolve or distribute. These phenomena have been studied by various techniques^[53-57], but it is difficult to determine whether their results are consistent with actual phenomena. In order to solve this issue, the solution should be observed with more direct techniques, such as TEM observation.

1-5. TEM

TEM is a type of microscope that uses electron beam irradiation and is one of the most powerful observation techniques for nanosized materials^[2, 58-63]. In TEM

observation, an image is obtained by transmitting an electron beam, which provides a direct observation of the sample with atomic resolution. TEM observation allows us not only to get images with atomic resolution but also to perform electron energy loss spectroscopy (EELS) and energy dispersive X-ray spectroscopy (EDX)^[62, 64-70], which enable elemental analysis, at the same time. In addition, it is possible to carry out structural analysis in detail by recording electron diffraction patterns^[71]. In this study, JEM-2100F and JEM-2010, which belong to the Alex group (University of California, Berkeley), were used for observations. JEM-2100F adopts an electron gun assisted by electric field emission and JEM-2010 adopts a filament as the electron gun.

With both TEM instruments, the observation is basically possible in the same way. The filament type emits electrons near the Fermi energy as an electron beam by supplying a voltage to the filament. In the field emission type, the potential is increased by applying an electric field to the electron beam source, which works to reduce, to some extent, the voltage necessary for electron emission.

The accelerating voltage was 80 kV for both instruments used in this study^[72]. At higher acceleration voltages, the transparency of the sample, which also depends on its thickness, and the image resolution should be improved. However, destruction of the carbon-carbon bonds is often observed with increasing voltage. Accelerated electrons at 80 kV, which are known not to knock on the carbon, are generally used in TEM observation of carbon-based materials^[72].

1-5-1. Graphene in TEM observation

Graphene, as an atomically thick sheet, provides an ultimate low-contrast image in

TEM observation^[73-77]. Graphene has excellent electron transfer characteristics, mechanical strength, and chemical stability; therefore, it is very suitable as a support for the sample. According to the above characteristics, it is possible to carry out TEM observation by placing the sample on a sheet of graphene. In addition, clear contrast in observation of samples, similar to that for free-standing samples in vacuum, is possible due to the low contrast of graphene^[76, 78]. We expect that the lattice of graphene will work as a ruler in TEM. Measuring the exact length in TEM observation is very important in order to ensure the certainty of observation. In usual observation, we need to correct the length in advance by observing a material having known lattice constants, such as gold particles. However, it is also possible to accurately measure lengths by utilizing graphene film as a reference. Therefore, we expect graphene to be very appropriate as a support for TEM observation.

1-5-2. Environmental cell

In TEM observation, samples have to be placed under high vacuum. Therefore, it is impossible to observe samples containing a liquid or gas because such samples vaporize immediately in vacuum systems^[79-84]. By using a structure such as that shown in Figure 1-7^[85], direct observation of liquid- and gas-based samples in the environment of a natural system is possible. This ideal structure is named an environmental cell and is primarily intended for use in the observation of a metal in a liquid or gaseous atmosphere. However, since the membranes used as walls and windows of the environmental cell require sufficient strength, the membranes are hardly transparent to the electron beam. In case of the observation of targeted light elements, environmental

cells do not provide enough contrast to obtain the target materials for determining the structure and dynamics in detail. Therefore, TEM observation assisted by environmental cells is limited to observing heavy elements in recent research.

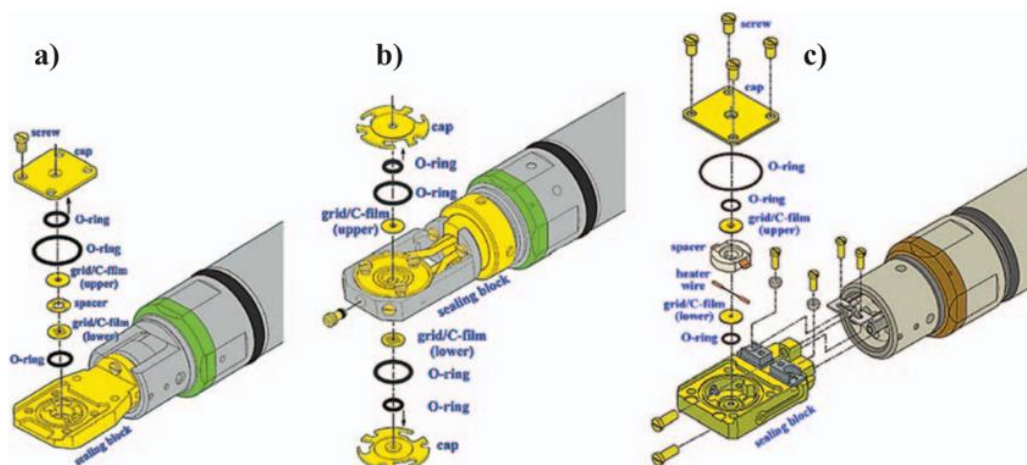


Figure 1-7: Image of environmental cells^[85]. (a) Observation with gases, (b) with liquids and (c) with heating.

1-5-3. TEM observation of liquids

TEM observation applied to liquids or solution-based materials, if realized, would be quite an effective technique for elucidating the detailed structure and various reaction mechanisms. If we succeed in confirming the chemical reaction processes and molecular design, it is expected that operations such as conditioning chemical reactions, which take a long time, will be drastically shortened. TEM observation of liquids is also expected to be applied to the development of effective drugs. However, liquids and solution-based materials have not been directly observed in previous studies, with the

exception of solidified solutions. Studies examining the mechanisms of various structures and reactions in the liquid phase have been performed only by calculation and spectral analysis by soft X-ray spectroscopy^[56, 86-87]. The reason for not being observed directly by electron microscopes for liquids is described in the Environmental cell section (1-5-2). Thus, we previously did not have the means to observe liquids directly. However, in 2013, the TEM observation of liquids by sandwiching an aqueous solution between two layers of graphene was experimentally shown by Jong Min Yuk belonging to Alex Zettl's group at the University of California Berkeley^[80]. Zettl's research group demonstrated that much higher-contrast TEM images revealing the growth process of a metal salt were provided by sandwiching an aqueous solution of a metal salt between graphene layers, which are named graphene liquid cells. However, since their observations have not been focused on liquids, or the contrast of the liquids was too strong because a large amount of aqueous solutions was sandwiched between the graphene layers, they have paid attention to the dynamics of the metal salt or metal^[66, 80, 88-90].

1-6. Summary

Various electric devices developed utilizing the electronic properties of graphene have been pursued actively since the discovery of graphene. However, the graphene utilized in device applications is basically produced by mechanical exfoliation. There are not many examples demonstrating high performance by utilizing a CVD-grown graphene. Therefore, it is important to establish the synthesis conditions of CVD-grown graphene that yield a large size and high-quality grain, in order to expand the range of

graphene applications. We should develop graphene transfer techniques that do not lead to damages or involve too many steps.

Furthermore, the TEM observation is an important technique for measurement and characterization of liquids, which provide innovative information corresponding to chemical reactions and coordination of liquids to biomaterials. If it was realized, characterization by TEM observation of liquids could become a necessary observation technique for a wide range of fields of science in the near future. By using graphene in place of conventional silicon membranes, we expect to obtain clear TEM images of liquids while suppressing undesirable effects such as vibration caused by charging. Assuming that graphene liquid cells will be broadly applied for general liquid observation, research into confinement effects resulting from the use of graphene liquid cells and how observations are actually made, is required.

In this study, we present three chapters on the development of TEM observation techniques for liquids. We report on the development of high-quality graphene synthesis methods in Chapter 2 and on the development of a new transfer method for subsequent use in Chapter 3. Fabrication and actual observation of various substances sandwiched between two graphene layers are presented in Chapter 4.

1-7. **References**

- [1] H. W. Kroto, J. R. Heath, S. C. O'Brien, R. F. Curl, R. E. Smalley, *Nature* **1985**, *318*, 162-163.
- [2] S. Iijima, *Nature* **1991**, *354*, 56-58.
- [3] R. Saito, M. Fujita, G. Dresselhaus, M. S. Dresselhaus, *PhRvB* **1992**, *46*, 1804-1811.
- [4] K. Tanaka, K. Okahara, M. Okada, T. Yamabe, *Chem. Phys. Lett.* **1992**, *191*, 469-472.
- [5] F. Diederich, R. L. Whetten, C. Thilgen, R. Ettl, I. T. O. Chao, M. M. Alvarez, *Science* **1991**, *254*, 1768-1770.
- [6] P. W. Dunk, M. Mulet-Gas, Y. Nakanishi, N. K. Kaiser, A. Rodriguez-Forteza, H. Shinohara, J. M. Poblet, A. G. Marshall, H. W. Kroto, *Nat Commun* **2014**, *5*, 5844.
- [7] P. W. Dunk, N. K. Kaiser, C. L. Hendrickson, J. P. Quinn, C. P. Ewels, Y. Nakanishi, Y. Sasaki, H. Shinohara, A. G. Marshall, H. W. Kroto, *Nat Commun* **2012**, *3*, 855.
- [8] D. W. Cagle, S. J. Kennel, S. Mirzadeh, J. M. Alford, L. J. Wilson, *Proc. Natl. Acad. Sci. U.S.A.* **1999**, *96*, 5182-5187.
- [9] T. Akasaka, T. Wakahara, S. Nagase, K. Kobayashi, M. Waelchli, K. Yamamoto, M. Kondo, S. Shirakura, S. Okubo, Y. Maeda, T. Kato, M. Kako, Y. Nakadaira, R. Nagahata, X. Gao, E. Van Caemelbecke, K. M. Kadish, *J. Am. Chem. Soc.* **2000**, *122*, 9316-9317.
- [10] H. Shinohara, *Rep. Prog. Phys.* **2000**, *63*, 843.
- [11] A. K. Geim, K. S. Novoselov, *Nature materials* **2007**, *6*, 183-191.
- [12] D. S. Bethune, C. H. Klang, M. S. de Vries, G. Gorman, R. Savoy, J. Vazquez, R. Beyers, *Nature* **1993**, *363*, 605-607.
- [13] S. J. Tans, A. R. Verschueren, C. Dekker, *Nature* **1998**, *393*, 49-52.
- [14] S. Iijima, T. Ichihashi, *Nature* **1993**, *363*, 603-605.
- [15] R. Martel, T. Schmidt, H. Shea, T. Hertel, P. Avouris, *Appl. Phys. Lett.* **1998**, *73*, 2447-2449.
- [16] A. Thess, R. Lee, P. Nikolaev, H. Dai, P. Petit, J. Robert, C. Xu, Y. H. Lee, S. G. Kim, A. G. Rinzler, *Science-AAAS-Weekly Paper Edition* **1996**, *273*, 483-487.
- [17] R. Saito, G. Dresselhaus, M. S. Dresselhaus, *Physical properties of carbon nanotubes*, World Scientific, Imperial College Press, London, **1998**.
- [18] T. Shimada, T. Okazaki, R. Taniguchi, T. Sugai, H. Shinohara, K. Suenaga, Y. Ohno, S. Mizuno, S. Kishimoto, T. Mizutani, *Appl. Phys. Lett.* **2002**, *81*,

4067-4069.

- [19] A. D. Franklin, M. Luisier, S.-J. Han, G. Tulevski, C. M. Breslin, L. Gignac, M. S. Lundstrom, W. Haensch, *Nano Lett.* **2012**, *12*, 758-762.
- [20] A. D. Franklin, G. S. Tulevski, S.-J. Han, D. Shahrjerdi, Q. Cao, H.-Y. Chen, H. S. P. Wong, W. Haensch, *ACS Nano* **2012**, *6*, 1109-1115.
- [21] Z. Wang, K. Zhao, H. Li, Z. Liu, Z. Shi, J. Lu, K. Suenaga, S.-K. Joung, T. Okazaki, Z. Jin, Z. Gu, Z. Gao, S. Iijima, *J. Mater. Chem.* **2011**, *21*, 171-180.
- [22] A. I. Chernov, P. V. Fedotov, A. V. Talyzin, I. Suarez Lopez, I. V. Anoshkin, A. G. Nasibulin, E. I. Kauppinen, E. D. Obratsova, *ACS Nano* **2013**, *7*, 6346-6353.
- [23] T. Shimada, Y. Ohno, T. Okazaki, T. Sugai, K. Suenaga, S. Kishimoto, T. Mizutani, T. Inoue, R. Taniguchi, N. Fukui, H. Okubo, H. Shinohara, *Physica E: Low-dimensional Systems and Nanostructures* **2004**, *21*, 1089-1092.
- [24] L.-J. Li, A. N. Khlobystov, J. G. Wiltshire, G. A. D. Briggs, R. J. Nicholas, *Nat Mater* **2005**, *4*, 481-485.
- [25] R. Nakanishi, R. Kitaura, J. H. Warner, Y. Yamamoto, S. Arai, Y. Miyata, H. Shinohara, *Scientific reports* **2013**, *3*.
- [26] R. Nakanishi, R. Kitaura, P. Ayala, H. Shiozawa, K. de Blauwe, P. Hoffmann, D. Choi, Y. Miyata, T. Pichler, H. Shinohara, *PhRvB* **2012**, *86*, 115445.
- [27] P. Ayala, R. Kitaura, R. Nakanishi, H. Shiozawa, D. Ogawa, P. Hoffmann, H. Shinohara, T. Pichler, *PhRvB* **2011**, *83*, 085407.
- [28] K. S. Novoselov, A. K. Geim, S. V. Morozov, D. Jiang, Y. Zhang, S. V. Dubonos, I. V. Grigorieva, A. A. Firsov, *Science* **2004**, *306*, 666-669.
- [29] J. C. Meyer, A. K. Geim, M. Katsnelson, K. Novoselov, T. Booth, S. Roth, *Nature* **2007**, *446*, 60-63.
- [30] C. Lee, X. Wei, J. W. Kysar, J. Hone, *Science* **2008**, *321*, 385-388.
- [31] A. Kuzmenko, E. Van Heumen, F. Carbone, D. Van Der Marel, *Phys. Rev. Lett.* **2008**, *100*, 117401.
- [32] P. R. Wallace, *Phys. Rev.* **1947**, *71*, 622.
- [33] J.-C. Charlier, P. Eklund, J. Zhu, A. Ferrari, in *Carbon nanotubes*, Springer, **2008**, pp. 673-709.
- [34] J.-H. Chen, C. Jang, S. Xiao, M. Ishigami, M. S. Fuhrer, *Nature nanotech.* **2008**, *3*, 206-209.
- [35] G. W. Semenoff, *Phys. Rev. Lett.* **1984**, *53*, 2449.
- [36] P. Avouris, Z. Chen, V. Perebeinos, *Nature nanotech.* **2007**, *2*, 605-615.
- [37] R. Nair, P. Blake, A. Grigorenko, K. Novoselov, T. Booth, T. Stauber, N. Peres, A. Geim, *Science* **2008**, *320*, 1308-1308.

- [38] X. Li, W. Cai, J. An, S. Kim, J. Nah, D. Yang, R. Piner, A. Velamakanni, I. Jung, E. Tutuc, *Science* **2009**, *324*, 1312-1314.
- [39] G. H. Han, F. Güneş, J. J. Bae, E. S. Kim, S. J. Chae, H.-J. Shin, J.-Y. Choi, D. Pribat, Y. H. Lee, *Nano Lett.* **2011**, *11*, 4144-4148.
- [40] T. Ohta, A. Bostwick, J. L. McChesney, T. Seyller, K. Horn, E. Rotenberg, *Phys. Rev. Lett.* **2007**, *98*, 206802.
- [41] A. Bostwick, T. Ohta, J. L. McChesney, K. V. Emtsev, T. Seyller, K. Horn, E. Rotenberg, *NJPh* **2007**, *9*, 385.
- [42] S. Amini, J. Garay, G. Liu, A. A. Balandin, R. Abbaschian, *J. Appl. Phys.* **2010**, *108*, 094321.
- [43] A. Reina, X. Jia, J. Ho, D. Nezich, H. Son, V. Bulovic, M. S. Dresselhaus, J. Kong, *Nano Lett.* **2009**, *9*, 30-35.
- [44] K. S. Kim, Y. Zhao, H. Jang, S. Y. Lee, J. M. Kim, K. S. Kim, J.-H. Ahn, P. Kim, J.-Y. Choi, B. H. Hong, *Nature* **2009**, *457*, 706-710.
- [45] T. Uwannu, Y. Hattori, T. Taniguchi, K. Watanabe, K. Nagashio, *2D Materials* **2015**, *2*, 041002.
- [46] X. Liang, B. A. Sperling, I. Calizo, G. Cheng, C. A. Hacker, Q. Zhang, Y. Obeng, K. Yan, H. Peng, Q. Li, X. Zhu, H. Yuan, A. R. Hight Walker, Z. Liu, L.-m. Peng, C. A. Richter, *ACS Nano* **2011**, *5*, 9144-9153.
- [47] C. Mattevi, H. Kim, M. Chhowalla, *J. Mater. Chem.* **2011**, *21*, 3324-3334.
- [48] L. Zhao, K. T. Rim, H. Zhou, R. He, T. F. Heinz, A. Pinczuk, G. W. Flynn, A. N. Pasupathy, *Solid State Commun.* **2011**, *151*, 509-513.
- [49] V. I. Artyukhov, Y. Hao, R. S. Ruoff, B. I. Yakobson, *Phys. Rev. Lett.* **2015**, *114*, 115502.
- [50] N. R. Wilson, A. J. Marsden, M. Saghir, C. J. Bromley, R. Schaub, G. Costantini, T. W. White, C. Partridge, A. Barinov, P. Dudin, *Nano Res.* **2013**, *6*, 99-112.
- [51] L. Guildner, D. Johnson, F. Jones, *J. Res. Natl. Bur. Stand. A* **1976**, *80*, 505-521.
- [52] M. Chaplin, *Water Phase Diagram*, **2016**, http://www1.lsbu.ac.uk/water/water_phase_diagram.html, 1/19/2016.
- [53] R. Ludwig, *Angew. Chem. Int. Ed.* **2001**, *40*, 1808-1827.
- [54] D. Prendergast, G. Galli, *Phys. Rev. Lett.* **2006**, *96*, 215502.
- [55] E. M. Choi, Y. H. Yoon, S. Lee, H. Kang, *Phys. Rev. Lett.* **2005**, *95*, 085701.
- [56] C. Huang, K. T. Wikfeldt, T. Tokushima, D. Nordlund, Y. Harada, U. Bergmann, M. Niebuhr, T. Weiss, Y. Horikawa, M. Leetmaa, *Proc. Natl. Acad. Sci.* **2009**, *106*, 15214-15218.
- [57] X. Lin, A. Groß, *Surf Sci.* **2012**, *606*, 886-891.

- [58] P. Batson, N. Dellby, O. Krivanek, *Nature* **2002**, *418*, 617-620.
- [59] J. Sloan, J. Hammer, M. Zwiefka-Sibley, M. L. H. Green, J. Sloan, *Chem. Commun.* **1998**, 347-348.
- [60] R. R. Meyer, J. Sloan, R. E. Dunin-Borkowski, A. I. Kirkland, M. C. Novotny, S. R. Bailey, J. L. Hutchison, M. L. H. Green, *Science* **2000**, *289*, 1324-1326.
- [61] T. Sasaki, H. Sawada, F. Hosokawa, Y. Sato, K. Suenaga, *Ultmi* **2014**, *145*, 50-55.
- [62] R. Senga, H.-P. Komsa, Z. Liu, K. Hirose-Takai, A. V. Krasheninnikov, K. Suenaga, *Nat Mater* **2014**, *13*, 1050-1054.
- [63] J. Zhang, Z. Zhu, Y. Feng, H. Ishiwata, Y. Miyata, R. Kitaura, J. E. P. Dahl, R. M. K. Carlson, N. A. Fokina, P. R. Schreiner, D. Tománek, H. Shinohara, *Angew. Chem. Int. Ed.* **2013**, *52*, 3717-3721.
- [64] E. Boyes, P. Gai, *Ultmi* **1997**, *67*, 219-232.
- [65] Z. Liu, K. Suenaga, Z. Wang, Z. Shi, E. Okunishi, S. Iijima, *Nat Commun* **2011**, *2*, 213.
- [66] C. Wang, Q. Qiao, T. Shokuhfar, R. F. Klie, *Adv. Mater.* **2014**, *26*, 3410-3414.
- [67] Y.-C. Lin, D. O. Dumcenco, Y.-S. Huang, K. Suenaga, *Nat Nano* **2014**, *9*, 391-396.
- [68] Y. Chen, J. Xi, D. O. Dumcenco, Z. Liu, K. Suenaga, D. Wang, Z. Shuai, Y.-S. Huang, L. Xie, *ACS Nano* **2013**, *7*, 4610-4616.
- [69] B. A. Sexton, *Surf Sci.* **1981**, *102*, 271-281.
- [70] S. Iijima, M. Yudasaka, R. Yamada, S. Bandow, K. Suenaga, F. Kokai, K. Takahashi, *Chem. Phys. Lett.* **1999**, *309*, 165-170.
- [71] K. Hirahara, S. Bandow, K. Suenaga, H. Kato, T. Okazaki, H. Shinohara, S. Iijima, *PhRvB* **2001**, *64*, 115420.
- [72] B. W. Smith, D. E. Luzzi, *J. Appl. Phys.* **2001**, *90*, 3509-3515.
- [73] A. Hashimoto, K. Suenaga, A. Gloter, K. Urita, S. Iijima, *Nature* **2004**, *430*, 870-873.
- [74] J. C. Meyer, A. K. Geim, M. I. Katsnelson, K. S. Novoselov, T. J. Booth, S. Roth, *Nature* **2007**, *446*, 60-63.
- [75] J. H. Warner, M. H. Rummeli, T. Gemming, B. Büchner, G. A. D. Briggs, *Nano Lett.* **2009**, *9*, 102-106.
- [76] B. Li, H. Cao, J. Shao, M. Qu, J. H. Warner, *J. Mater. Chem.* **2011**, *21*, 5069-5075.
- [77] A. W. Robertson, C. S. Allen, Y. A. Wu, K. He, J. Olivier, J. Neethling, A. I. Kirkland, J. H. Warner, *Nat Commun* **2012**, *3*, 1144.

- [78] J. C. Meyer, C. O. Girit, M. F. Crommie, A. Zettl, *Nature* **2008**, *454*, 319-322.
- [79] N. De Jonge, D. B. Peckys, G. Kremers, D. Piston, *Proc. Natl. Acad. Sci.* **2009**, *106*, 2159-2164.
- [80] J. M. Yuk, J. Park, P. Ercius, K. Kim, D. J. Hellebusch, M. F. Crommie, J. Y. Lee, A. Zettl, A. P. Alivisatos, *Science* **2012**, *336*, 61-64.
- [81] D. Parsons, *Science* **1974**, *186*, 407-414.
- [82] K.-L. Liu, C.-C. Wu, Y.-J. Huang, H.-L. Peng, H.-Y. Chang, P. Chang, L. Hsu, T.-R. Yew, *LChip* **2008**, *8*, 1915-1921.
- [83] H.-G. Liao, D. Zherebetsky, H. Xin, C. Czarnik, P. Ercius, H. Elmlund, M. Pan, L.-W. Wang, H. Zheng, *Science* **2014**, *345*, 916-919.
- [84] J. Wu, W. Gao, J. Wen, D. J. Miller, P. Lu, J.-M. Zuo, H. Yang, *Nano Lett.* **2015**, *15*, 2711-2715.
- [85] A. Ishikawa, *顯微鏡* **2008**, *43*.
- [86] T. Tokushima, Y. Harada, O. Takahashi, Y. Senba, H. Ohashi, L. G. Pettersson, A. Nilsson, S. Shin, *Chem. Phys. Lett.* **2008**, *460*, 387-400.
- [87] T. Tokushima, Y. Horikawa, O. Takahashi, H. Arai, K. Sadakane, Y. Harada, Y. Takata, S. Shin, *PCCP* **2014**, *16*, 10753-10761.
- [88] J. M. Yuk, Q. Zhou, J. Chang, P. Ercius, A. P. Alivisatos, A. Zettl, *ACS Nano* **2015**.
- [89] M. Jeong, J. M. Yuk, J. Y. Lee, *Chem. Mater.* **2015**, *27*, 3200-3202.
- [90] J. M. Yuk, H. K. Seo, J. W. Choi, J. Y. Lee, *ACS nano* **2014**, *8*, 7478-7485.

Chapter 2

2. Graphene growth

2-1. Introduction

In order to sandwich the liquids between two graphene layers and observe by TEM, high-quality graphene with sufficient strength and size is required^[1-2]. Therefore, it is necessary to produce monocrystalline graphene by a CVD method. Although graphene produced by mechanical exfoliation is of perfect quality, thus-produced graphene has a small grain size. In addition, it is technically difficult to reproducibly suspend the graphene onto a TEM grid by a mechanical exfoliation process.

However, there is a problem to be solved with the CVD method. CVD synthesis of grapheme, which is monocrystalline or single domain, has not been achieved^[1, 3-9]. Graphene with grain boundaries needs a polymer support to transfer it to the substrate or TEM grid, because less-bonded graphene does not have enough strength^[10-13]. However, when preparing grapheme-sandwiched structures with polymer support, a poor yield of graphene liquid cells is obtained. Furthermore, polymers cannot be removed completely.

The main cause of the occurrence of grain boundaries in graphene is that there is a boundary on the surface of the copper foil, which is the substrate of the epitaxial growth^[3, 6, 14-16]. Graphene grows with very different orientations from complex crystal surfaces having boundaries, and weakly bonded seven-membered or five-membered rings are formed when collision between growing graphene sheets occurs^[4, 17]. In other words, boundary-less graphene is obtainable if a single-crystal copper surface is possible. Images representing the relation between the direction of two sheets of graphene and the boundary are shown in Figure 2-1.

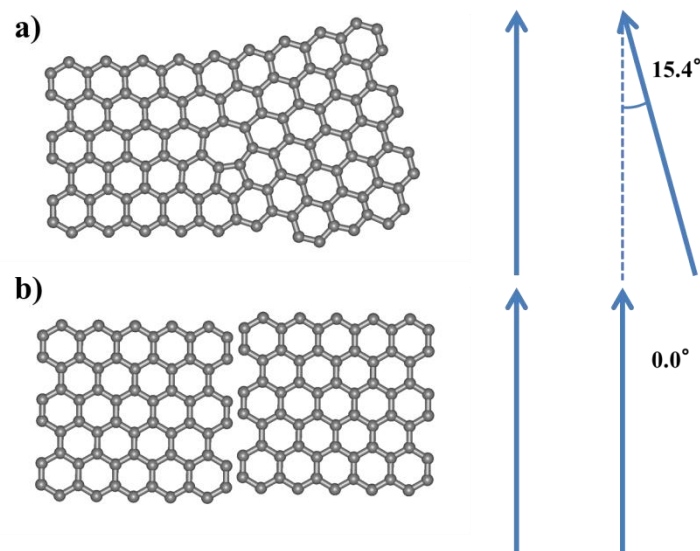


Figure 2-1: Structure images of graphene boundary.

The arrows in Figure 2-1 represent the deviation of the angle of graphene. Figure 2-1 a) is an image in which graphene sheets rotated by 15.4° with respect to each other have collided. Figure 2-1 b) shows no angular deviation but instead a translation. In Figure 2-1 a), five-membered and seven-membered rings can be seen, in addition to

six-membered rings. In Figure 2-1 b), most terminal carbon atoms are coupled to a substrate such as copper foil, and thus, strong bonds between each carbon atom cannot exist. As seen from Figure 2-1, even in the collision of graphene sheets facing the same direction, a boundary occurs. Furthermore, coupling graphene of different orientations is more difficult. An ideal combination of all grains of graphene is difficult, even if there was some correction to the translational displacement by the liquid-like phase of the copper substrate surface. To briefly conclude, the state in which graphene single grains are grown on a large area has the most ideal structure.

However, it is difficult to accurately control the number of grains at long growth times, which is necessary for growing single grains^[18-19]. Moreover, control of the graphene layer number at long reaction times is difficult. Therefore, as a compromise, we tried to align the surface of the copper foil to form a pseudo-single surface, and graphene was grown on the single-crystalline copper surface in a relatively short time in the same orientation. Apparently, graphene has many boundaries, but in fact, it is possible to obtain graphene with strong boundaries, or boundary-less graphene, by adding hydrogen to the copper foil.

2-2. Preparation and apparatus

The apparatus shown in Figure 2-2 were prepared for graphene CVD growth. A quartz ($\phi 26-30 \times 1000$ mm) or alumina (SSA-S, $\phi 26-30 \times 1000$ mm) tube is heated by an electric furnace, and a gauge adapter connects the tube to the gas line. The gas line has five mass flow controllers and five gases. Pure H₂, pure methane, pure Ar, Ar/3% H₂, and Ar/3% H₂/0.01% CH₄ are introduced to the quartz tube through this gas line and gas

passed through the tube is guided to the exhaust line. An O_2 detector is placed at the end of the tube. The quartz boat shown in Figure 2-3 makes the substrate available for introduction into the heated quartz or alumina tube, and is available for ejection of the substrate to facilitate rapid cooling after the reaction.

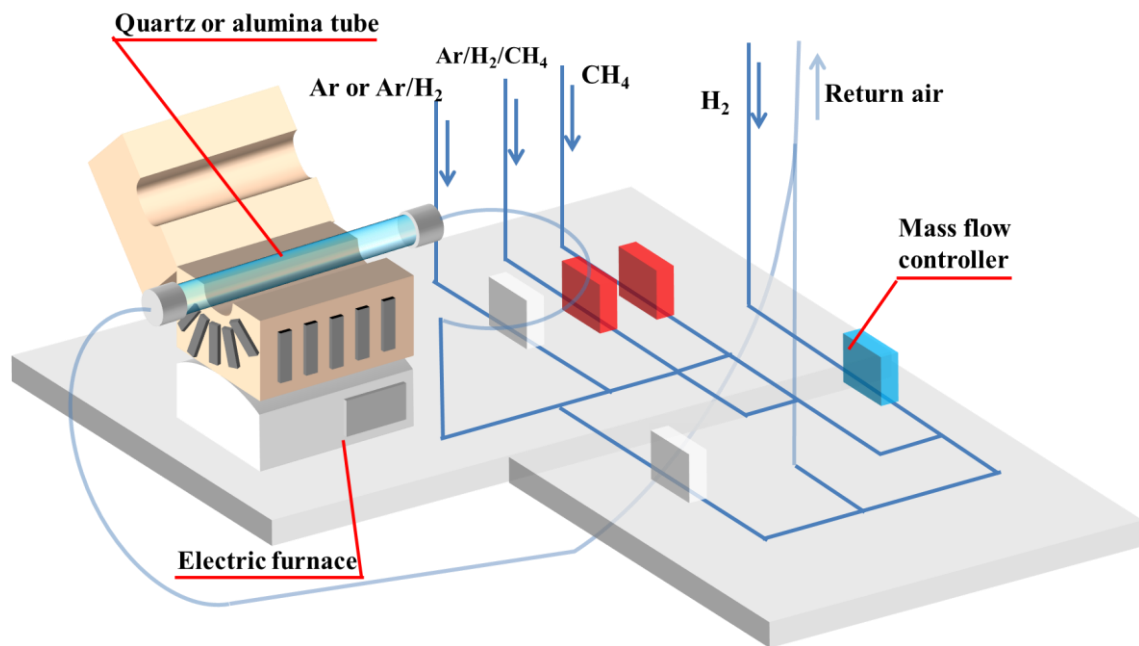


Figure 2-2: Schematic image of the CVD apparatus.

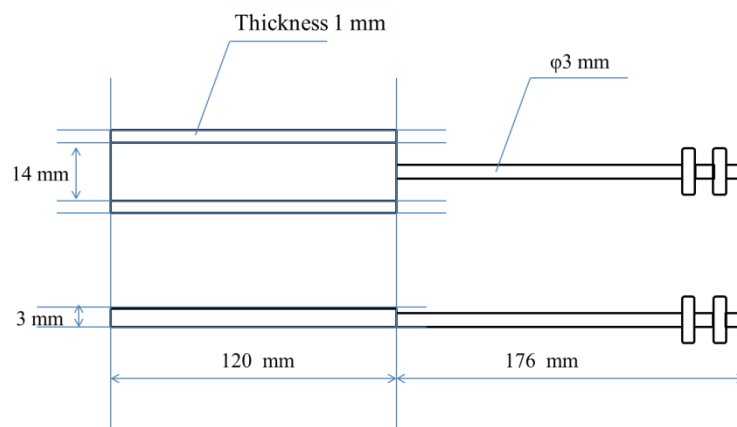


Figure 2-3: Schematic image of a quartz boat.

In this work, copper foil (Nilaco, 99.9%) is more suitable than other metal substrates because it is easy to control for producing the mono- or few-layer graphene. The solubility of carbon atoms in the copper substrate is lower than that in other metals, about 0.01% at 1273K. In the usual CVD method, deposition is performed in a vacuum system for monolayer graphene growth because of reduced carbon solubility. However, it is not the only method for realizing monolayer graphene in a vacuum CVD chamber. In our work, monolayer graphene can be produced at atmospheric pressure with a minute amount of carbon source and a large amount of argon as buffer gas.

2-3. **Growth mechanism**

According to much research^[6, 8, 20], graphene on copper substrates is grown by dispersing carbon atoms on the copper surface. The density of graphene domains depends on the density of nucleation sites on the copper surface. This is true if the copper surface has many defects and boundary layers, or if carbon atoms are present in small enough amounts not to encounter other carbon atoms. An image depicting graphene nucleation sites on a copper surface is shown in Figure 2-4. This figure suggests that we should atomically clean the copper surface in order to control the graphene domain density and orientation.

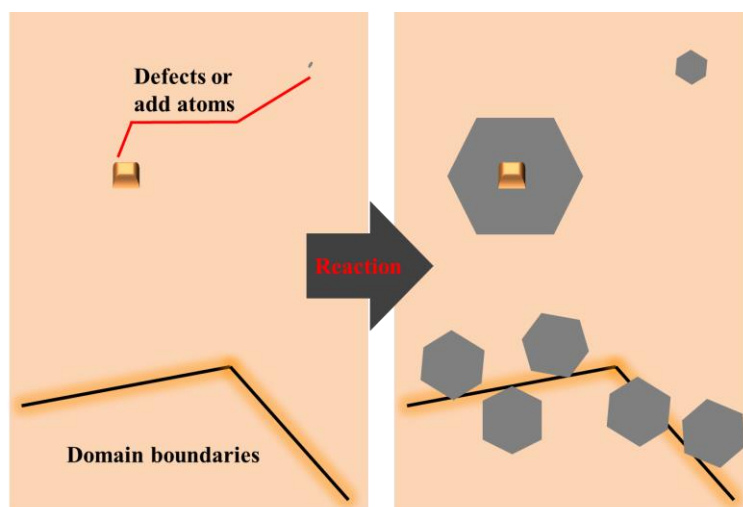


Figure2-4: Image depicting graphene nucleation sites.

At the moment of nucleation, the carbon source and copper substrate are decomposed to carbon atoms and copper hydrate, and then carbon atoms move around the copper surface. When carbon atoms encounter other reactive atoms, carbon atoms will bond with the other atoms. Repeating this process, carbon atoms will chain together, becoming longer and longer. At the same time, chained carbon atoms are etched by hydrogen gas or by dissolved hydrogen in the copper substrate. Weakly bonded carbon atoms, which are often located on the edge of the graphene or are misplaced from the hexagonal structure, are easier to remove than carbon atoms in the hexagonal structure. Therefore, a graphitic structure can be produced on the copper surface so that the copper surface is finally covered by graphene. When graphene covers the surface, individual domains bond together. If domains grow in the same orientation, their bonding will result in a hexagonal structure. In contrast, if domains grow in different orientations, bonding will result in a more defective structure. During the growth, the driving force for reconstruction is etching by dissolved hydrogen atoms in the copper; it is not only

provided by hydrogen from the gas phase.

2-4. **Pretreatment**

CVD growth of graphene is strongly influenced by the substrate, and the (111) surface of copper is known to be a suitable surface to grow well-orientated graphene. To prepare the (111) surface, high-temperature preheating of the copper foil under pure H₂ flow at atmospheric pressure was utilized. After the pretreatment, almost the entire surface of the copper foil turned into the (111) surface, and grain boundaries in the copper foil almost disappeared, which is one difference compared with typical pretreatments using 3% H₂/Ar gas. The largest difference between the two pretreatments is found in the mechanical strength of the graphene sheets, due to differences in reconstruction of the graphene domain boundaries.

Graphene can also be grown on a copper oxide surface in the same way. Graphene can be obtained by pretreatment in minute amounts of oxygen gas instead of hydrogen gas. About 1.2% O₂ was introduced to an Ar atmosphere, and a 4 min annealing process provided a well-inactivated copper surface. Unfortunately, graphene domains grown in this oxidation method do not seem to connect with each other. However, the fairly low density of graphene domains inhibited nucleation by oxidation, and can promote the formation of large-sized single-domain graphene, which reached 1 × 1 cm² in recent research.

2-5. **Reactions**

In this work, reactions are performed at ordinary pressure and with a low

concentration of methane gas as the carbon source, which is added to a H₂/Ar atmosphere. Heating at 1323 K induces decomposition of methane. The growth rate is dependent on the total amount of carbon atoms, but is independent of the carbon/hydrogen ratio. The only influence of the carbon/hydrogen ratio is to create the carbon hexagonal network while breaking weak structures. As long as the amount of carbon does not decrease significantly, the amount of nucleation sites exhibits the same tendency as the growth rate.

2-6. Experimental

First, the quartz tube ($\phi 26\text{--}30 \times 1000$ mm) CVD chamber was heated by an electric furnace to 1323 K. The air inside of the quartz tube was then completely exchanged with Argon gas (99.99%) after placing a piece of copper foil (niraco, 99.9%, $10 \times 100 \times 0.02$ mm³) into the quartz boat. The atmosphere was then exchanged with hydrogen gas (99.999%) and the copper foil in the quartz boat was moved into the furnace and annealed for 50 min. In this pretreatment, the copper surface forms a single-crystalline (111) plane and a critical amount of hydrogen atoms dissolves inside the copper foil. These hydrogen atoms support reconstruction of graphene domain boundaries, which is one of the key steps required for the preparation of high-quality graphene films. Excessive hydrogen gas pressure will prevent decomposition of methane as the carbon source due to a loss in catalysis. After the pretreatment, the pure hydrogen gas was quickly exchanged with an Ar/H₂/CH₄ mixture (Ar; 97%, H₂; 3%, CH₄; 0.002%). The graphene growth time was 8-16 h and was dependent on the state of the copper surface before pretreatment. Finally, the quartz boat was dragged out from the furnace to

quench. At the same time, the flow gas was exchanged for pure Ar to stop the reaction completely. As a result, large-scale oriented monolayer graphene covered both sides of the copper foil.

In other experiments, pretreatment in an oxygen atmosphere (Ar; 98.9%, O₂; 1.1%) was performed for 4 min, followed by reduction by an Ar/H₂ mixed gas for 60 min. The growth conditions were the same as those for the hydrogen annealing method. To investigate the effect of the different pretreatment methods on film growth, copper foils annealed in each of the following conditions were prepared: pure H₂, Ar/H₂, and Ar/O₂ atmospheres. Graphene was then grown on each copper foil following the procedure given above. The effect of the pretreatment was evaluated by studying the density of nuclei and the shape of the graphene edge using scanning electron microscopy (SEM) and optical images.

Next, the effect of the reaction gas ratio on graphene growth on copper foil substrates that had been annealed in pure H₂ gas was investigated. The growth conditions are shown in Table 1.

Name	Ar (sccm)	H ₂ (sccm)	CH ₄ (sccm)
Sample A	145.5	4.5	0.005
Sample B	145.0	5.0	0.005
Sample C	141.0	9.0	0.005
Sample D	291.0	9.0	0.010
Sample E	295.5	4.5	0.0005

Table 1: Reaction gas composition during graphene growth.

Finally, graphene for TEM observation was synthesized under conditions that were optimized such that the reaction stopped when the graphene exactly covered the copper foil.

2-7. Results and discussion

Figures 2-5A, 2-5B, and 2-5C show typical SEM images of each sample, which were annealed in pure H₂, Ar/H₂, and Ar/O₂ atmospheres, respectively.

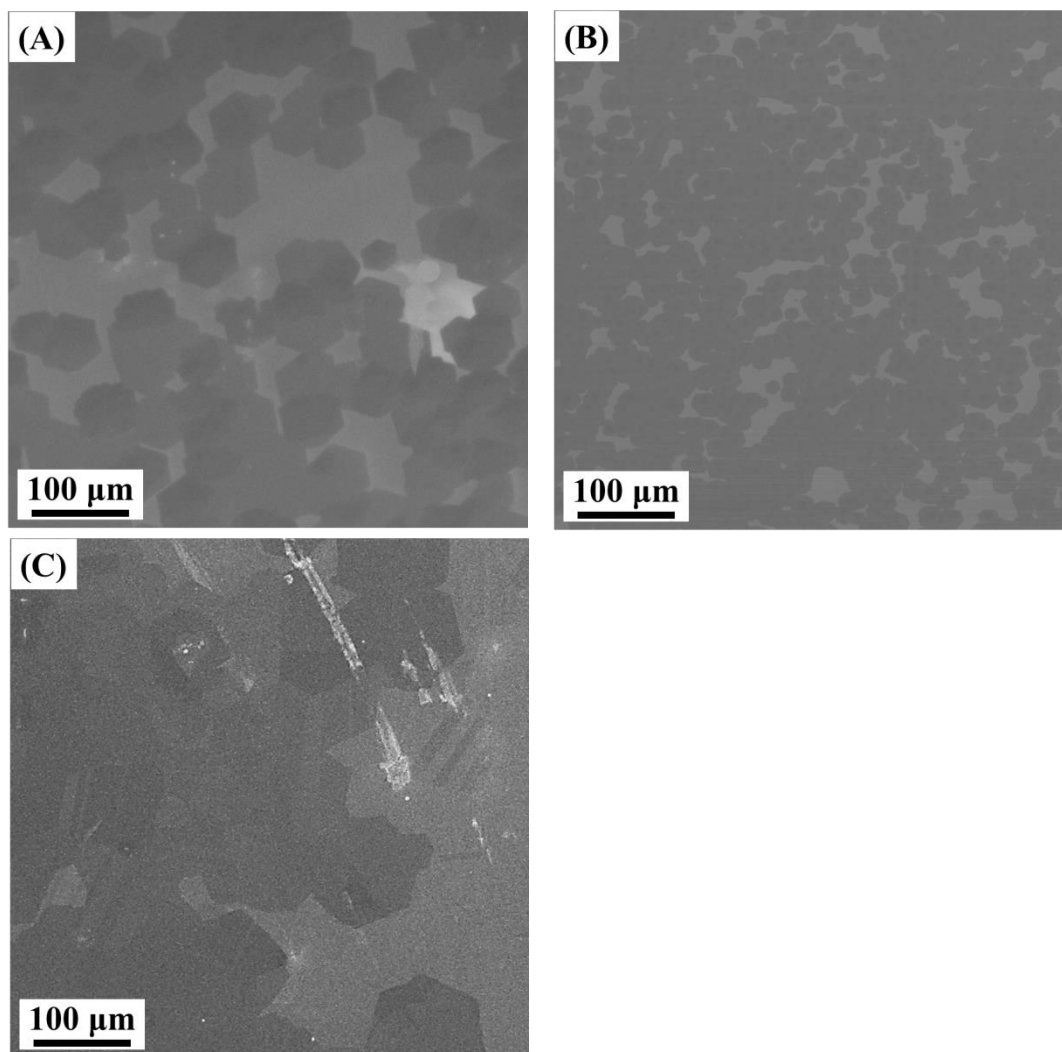


Figure 2-5: Typical SEM images of copper foils prepared by annealing in pure H₂ (A), Ar/H₂ (B), and Ar/O₂ (C) atmospheres.

Graphene annealed in pure hydrogen gas is shown in Figure 2-5A, which shows that there is preferential orientation and alignment of the hexagonally shaped graphene

sheets. Such alignment is not seen, however, in the other images shown in Figures 2-5B and 2-5C. The other difference between these three samples according to SEM observation is the density of the graphene domains. The density of the domains indicates the number of nucleation sites that existed on the copper surface. To further investigate the difference between Ar/H₂ and H₂ annealing, the domain size of the copper surface was studied. Figures 2-6A and 2-6B demonstrate how the domain size of the copper surface depends on the preparation method. Optical microscope observation can be used to visualize the domains of the copper surface, colored by the oxidization of copper. Oxidization was performed at approximately 500 K in air using a heating plate.

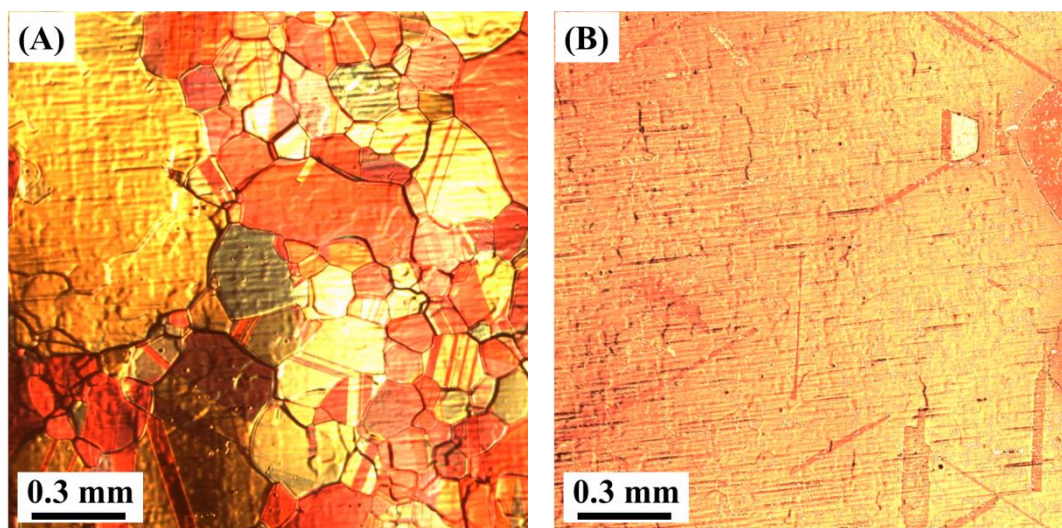


Figure 2-6: Optical microscope images of copper oxide surfaces.

The Ar/H₂-annealed copper surface shown in Figure 2-6A has several domains. On the other hand, the H₂-annealed copper surface shown in Figure 2-6B has few domains. This trend will dramatically influence graphene nucleation. The usual crystal surface of copper at high temperature is (111), but domain boundaries cause many types of crystal

surfaces to form. Figure 2-7 suggests that one boundary of the copper surface has the possibility to induce the formation of misoriented graphene domains. The growth speed of graphene is dependent on each plane and each orientation; thus, for planes near boundaries, graphene domains will grow rapidly, while others will grow in different orientations to those grown on the (111) surface. Therefore, H₂-annealed samples result in well-aligned graphene and less domains than Ar/H₂-annealed samples.

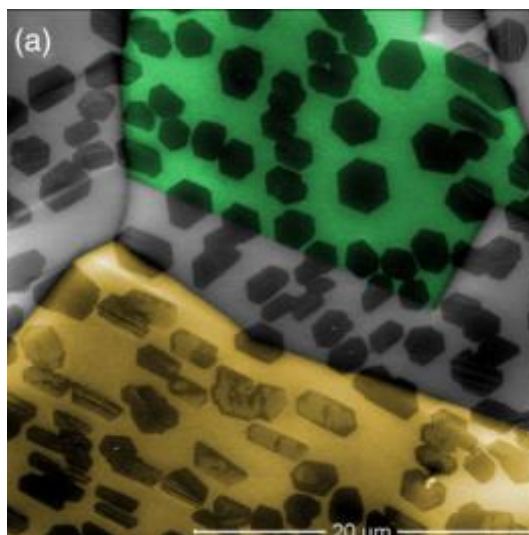


Figure 2-7: SEM image of copper domain boundaries, as confirmed by many crystal surfaces^[16].

On the other hand, our pretreatment with H₂ gas provides a flat and single-crystalline copper surface, in agreement with Figure 2-8(b). This image was obtained by the electron back scattering diffraction (EBSD) mapping technique. Figure 2-8(a) shows an SEM image observed on the same region of copper surface as in Figure 2-8(b). This mapping image suggests that the majority of the region has a (111) surface. The minor regions showing a (100) surface are caused by vaporization. There are no

domain boundaries.

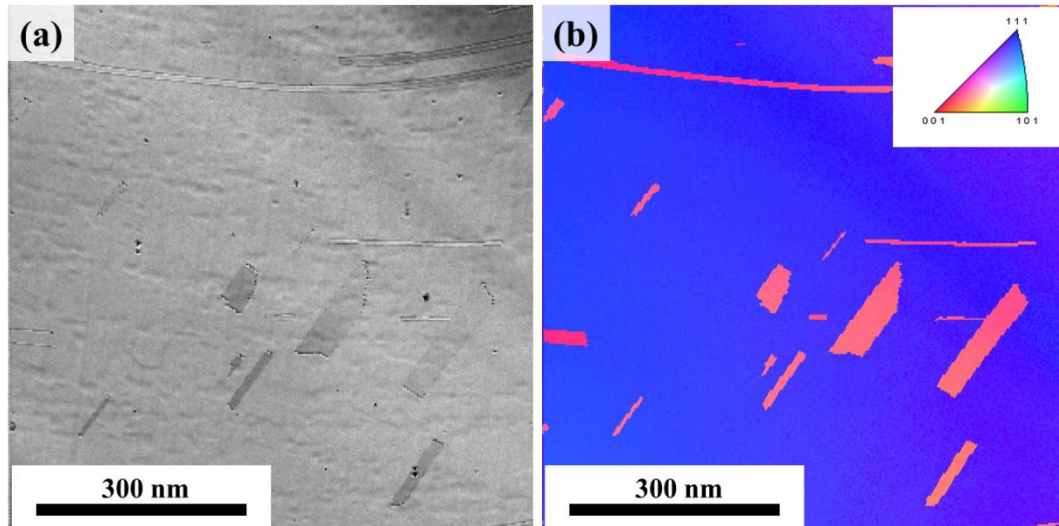


Figure 2-8: SEM (a) and EBSD (b) mapping images of a copper surface prepared with the hydrogen annealing method.

Copper oxide growth induces a low concentration of domains, as shown by the SEM image in Figure 2-5C. This phenomenon can be explained by the deactivation of nucleation sites by oxidation. In Figure 2-9, sphere-like contrasts were observed in SEM images of the oxidized copper foil. The spheres are created from copper, which suggests that oxygen inclusion in copper was excluded due to the bubbling of water vapor.

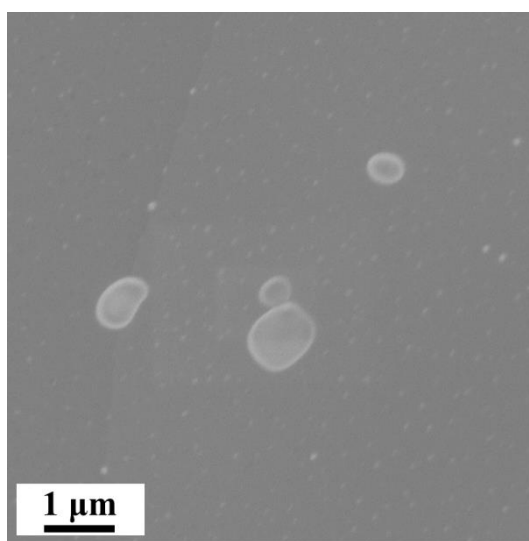
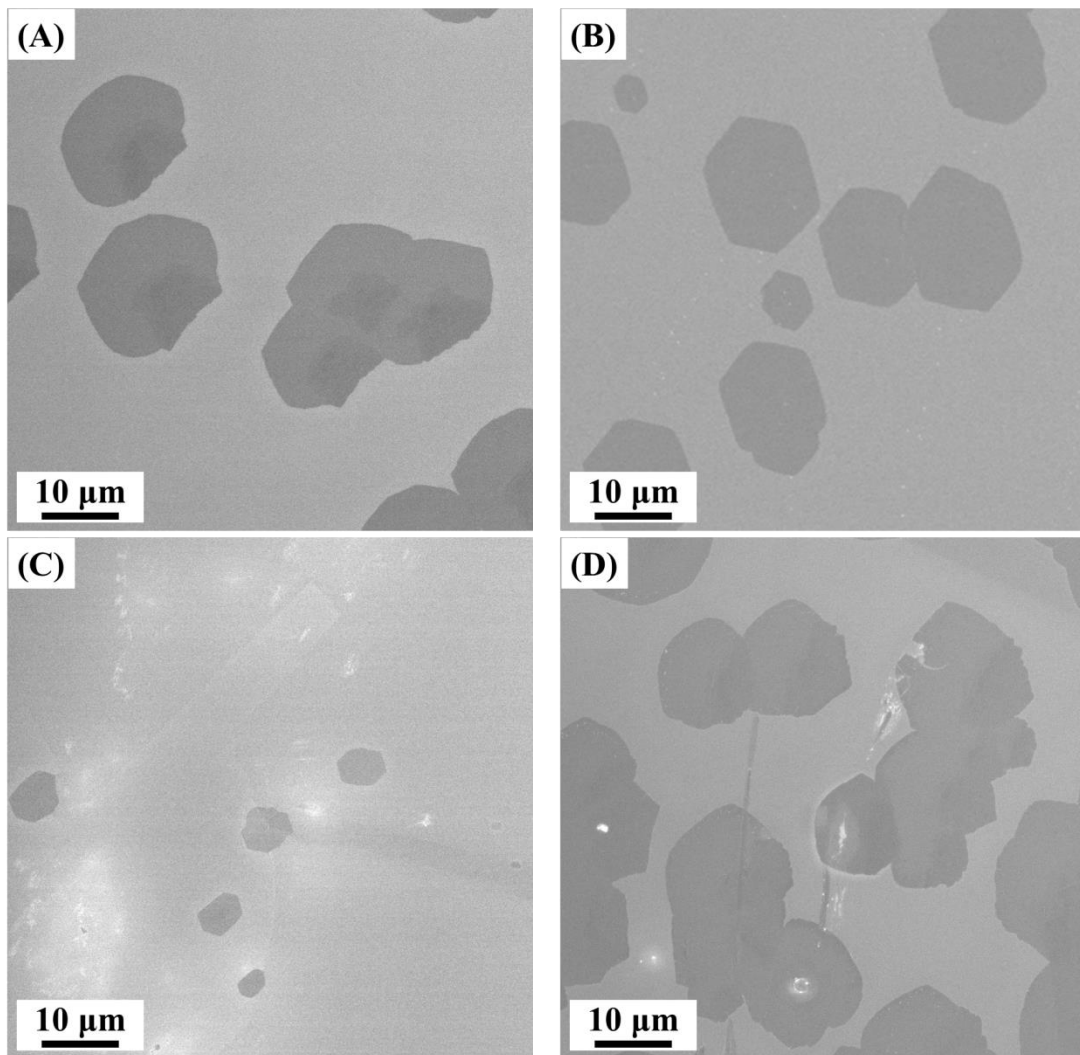


Figure 2-8: Magnified SEM image of a copper surface prepared by the oxidation pretreatment method.

Figures 2-10A, 2-10B, 2-10C, 2-10D, and 2-10E show typical SEM images of each sample; the conditions used for sample preparation are given in Table 1. Comparing Figures 2-10A and 2-10B, it is found that the ratio of hydrogen to carbon has no effect on the nucleation of graphene. The correct ratio of H_2/CH_4 is required for achieving the desired reconstruction of the graphene edge. When the carbon supply is much slower than the hydrogen etching speed, as in Figure 2-10C, large-scale graphene is not

produced, rather the number of domains is reduced. Comparing Figures 2-10A and 2-10D yields information about the relation between the carbon source flow rate and the domain nucleation properties. The amount of carbon source directly influenced the number of graphene domains and their growth rate. In sample E, argon gas was introduced for determining the flow rate of the buffer gas in our CVD setup. As shown Figure 2-10E, there is no change compared to Sample A, which means that a buffer gas flow rate of 150 sccm is sufficient for 0.0005 sccm methane.



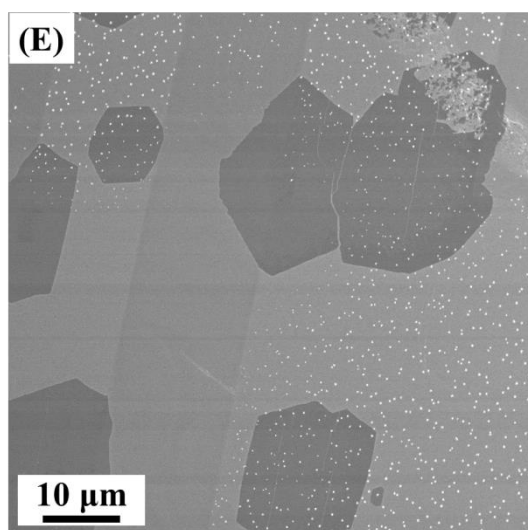


Figure 2-10: Typical SEM images of graphene grown on copper hydride.

Figure 2-10E indicates that there are many white spots that are localized on the upper and right sides of the SEM image. A magnification of these white spots is shown in Figure 2-11. It was determined by EELS and EDX analysis that these flower-like contaminations are made from silicon oxide. They come from the quartz tube, which is damaged by hydrogen embrittlement during the pretreatment.

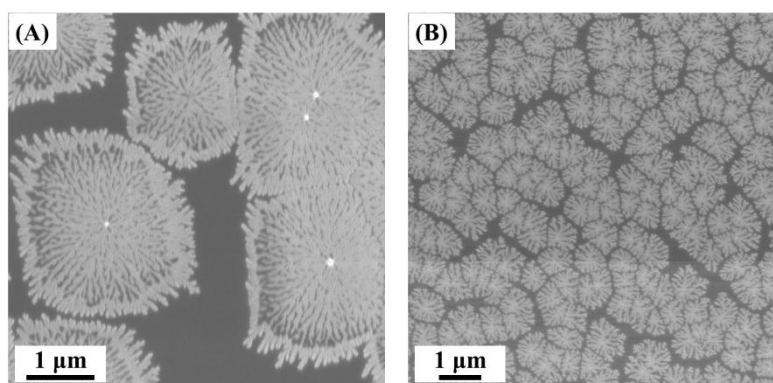


Figure 2-11: SEM images of contamination on copper and graphene surfaces.

Such silicon dioxide contamination, which inhibits graphene growth and reconstruction of domain boundaries, was frequently encountered when using a quartz tube. Silicon oxide contamination on the deposited graphene often integrated with the carbon atoms of the graphene, and silicon oxide on the copper interfered with the diffusion of carbon atoms. As a result, the graphene domains could not connect to each other and the graphene sheets that were finally obtained had many defects.

In an attempt to overcome this problem, an alumina tube was used as the CVD chamber to remove the possibility of silicon oxide contamination. However, in this case, alumina particle contamination was found to originate from the tube. In this work, we succeeded in reducing the number of particles by heating under vacuum overnight after CVD growth.

Finally, boundary-less graphene sheets with low levels of contamination were obtained, as shown in Figure 2-12. The SEM images include regions of uncovered copper surface for visualization of the shape of the graphene sheets. It is difficult to observe the covered surface because graphene has a flat contrast. Optical images suggest that the copper surface is completely covered by the boundary-less graphene sheet.

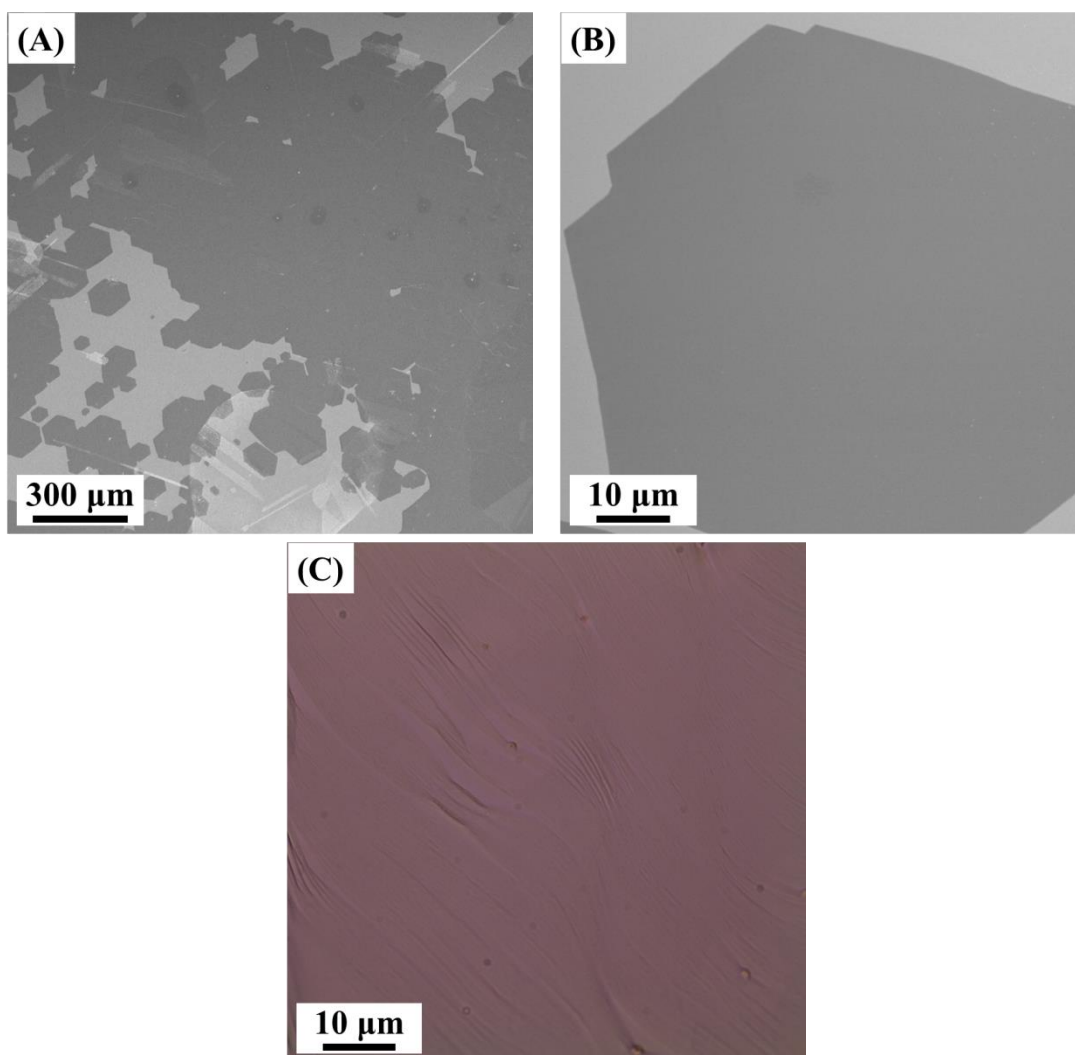


Figure 2-12: SEM images (A and B) of the graphene sheet and an optical image (C) of copper foil after heating in air.

2-8. Conclusion

In conclusion, we succeeded in obtaining highly crystalline large-area graphene sheets. By utilizing the graphene grown in this chapter, graphene liquid cells could be constructed, which is the focus of the following chapters. Producing single-crystal graphene on a commercially available copper foil substrate is an important achievement.

However, we found that the key to the process was using single-crystal copper foils, which were obtained by hydrogen annealing. Gases involved in the reaction needed for graphene growth, such as methane, and the copper foil as a catalyst, significantly degraded the quartz tube serving as a CVD chamber. Finally, by using an alumina tube as the CVD chamber, it became possible to obtain high-quality graphene with good reproducibility, provided that vacuum heating was performed overnight after each reaction.

2-9. References

- [1] G.-H. Lee, R. C. Cooper, S. J. An, S. Lee, A. van der Zande, N. Petrone, A. G. Hammerberg, C. Lee, B. Crawford, W. Oliver, *Science* **2013**, *340*, 1073-1076.
- [2] C. Lee, X. Wei, J. W. Kysar, J. Hone, *Science* **2008**, *321*, 385-388.
- [3] N. R. Wilson, A. J. Marsden, M. Saghir, C. J. Bromley, R. Schaub, G. Costantini, T. W. White, C. Partridge, A. Barinov, P. Dudin, *Nano Res.* **2013**, *6*, 99-112.
- [4] K. Kim, Z. Lee, W. Regan, C. Kisielowski, M. F. Crommie, A. Zettl, *ACS Nano* **2011**, *5*, 2142-2146.
- [5] G. H. Han, F. Güneş, J. J. Bae, E. S. Kim, S. J. Chae, H.-J. Shin, J.-Y. Choi, D. Pribat, Y. H. Lee, *Nano Lett.* **2011**, *11*, 4144-4148.
- [6] L. Zhao, K. T. Rim, H. Zhou, R. He, T. F. Heinz, A. Pinczuk, G. W. Flynn, A. N. Pasupathy, *Solid State Commun.* **2011**, *151*, 509-513.
- [7] X. Li, C. W. Magnuson, A. Venugopal, R. M. Tromp, J. B. Hannon, E. M. Vogel, L. Colombo, R. S. Ruoff, *J. Am. Chem. Soc.* **2011**, *133*, 2816-2819.
- [8] S. Bhaviripudi, X. Jia, M. S. Dresselhaus, J. Kong, *Nano Lett.* **2010**, *10*, 4128-4133.
- [9] S. Bae, H. Kim, Y. Lee, X. Xu, J.-S. Park, Y. Zheng, J. Balakrishnan, T. Lei, H. Ri Kim, Y. I. Song, Y.-J. Kim, K. S. Kim, B. Ozyilmaz, J.-H. Ahn, B. H. Hong, S. Iijima, *Nat Nano* **2010**, *5*, 574-578.
- [10] V. P. Verma, S. Das, I. Lahiri, W. Choi, *Appl. Phys. Lett.* **2010**, *96*, 203108.
- [11] X. Liang, B. A. Sperling, I. Calizo, G. Cheng, C. A. Hacker, Q. Zhang, Y. Obeng, K. Yan, H. Peng, Q. Li, X. Zhu, H. Yuan, A. R. Hight Walker, Z. Liu, L.-m. Peng, C. A. Richter, *ACS Nano* **2011**, *5*, 9144-9153.
- [12] Y. Lee, S. Bae, H. Jang, S. Jang, S.-E. Zhu, S. H. Sim, Y. I. Song, B. H. Hong, J.-H. Ahn, *Nano Lett.* **2010**, *10*, 490-493.
- [13] X. Li, Y. Zhu, W. Cai, M. Borysiak, B. Han, D. Chen, R. D. Piner, L. Colombo, R. S. Ruoff, *Nano Lett.* **2009**, *9*, 4359-4363.
- [14] L. Tao, J. Lee, H. Chou, M. Holt, R. S. Ruoff, D. Akinwande, *ACS Nano* **2012**, *6*, 2319-2325.
- [15] Y. Hao, M. S. Bharathi, L. Wang, Y. Liu, H. Chen, S. Nie, X. Wang, H. Chou, C. Tan, B. Fallahazad, H. Ramanarayan, C. W. Magnuson, E. Tutuc, B. I. Yakobson, K. F. McCarty, Y.-W. Zhang, P. Kim, J. Hone, L. Colombo, R. S. Ruoff, *Science* **2013**, *342*, 720-723.
- [16] V. I. Artyukhov, Y. Hao, R. S. Ruoff, B. I. Yakobson, *Phys. Rev. Lett.* **2015**, *114*, 115502.
- [17] A. W. Robertson, C. S. Allen, Y. A. Wu, K. He, J. Olivier, J. Neethling, A. I.

- Kirkland, J. H. Warner, *Nat Commun* **2012**, *3*, 1144.
- [18] K. S. Kim, Y. Zhao, H. Jang, S. Y. Lee, J. M. Kim, K. S. Kim, J.-H. Ahn, P. Kim, J.-Y. Choi, B. H. Hong, *Nature* **2009**, *457*, 706-710.
- [19] X. Li, W. Cai, J. An, S. Kim, J. Nah, D. Yang, R. Piner, A. Velamakanni, I. Jung, E. Tutuc, *Science* **2009**, *324*, 1312-1314.
- [20] C. Mattevi, H. Kim, M. Chhowalla, *J. Mater. Chem.* **2011**, *21*, 3324-3334.

Chapter 3

3. Graphene transfer and preparation of graphene-sandwiched structure

3-1. Introduction

Usually, graphene is grown on metal substrates^[1-13], and it is difficult to directly synthesize graphene suspended over holes (i.e., without a substrate)^[14]. Because of this issue, graphene grown on the metal substrate is transferred to another substrate or a TEM grid. To do this, graphene must be separated from the copper foil as an atomic layer. It is particularly difficult to determine by eye whether the graphene sheet contains domain boundaries. Graphene sheets containing domain boundaries will immediately disperse into pieces.

However, we can find graphene sheets containing domain boundaries by covering the graphene surface with a polymer^[2, 7]. The polymer also works as a support for preventing the graphene domains from dispersing into pieces, even if removed from the metal substrate. The difference between removing the metal substrate from a graphene sheet containing domain boundaries, with and without a polymer covering is illustrated

in Figure 3-1. Figure 3-2 shows photographs corresponding to each step in removing the metal substrate from graphene sheets containing domain boundaries, with and without a polymer covering. It is clear that the polymer works very well for transferring graphene to other substrates or a TEM grid.

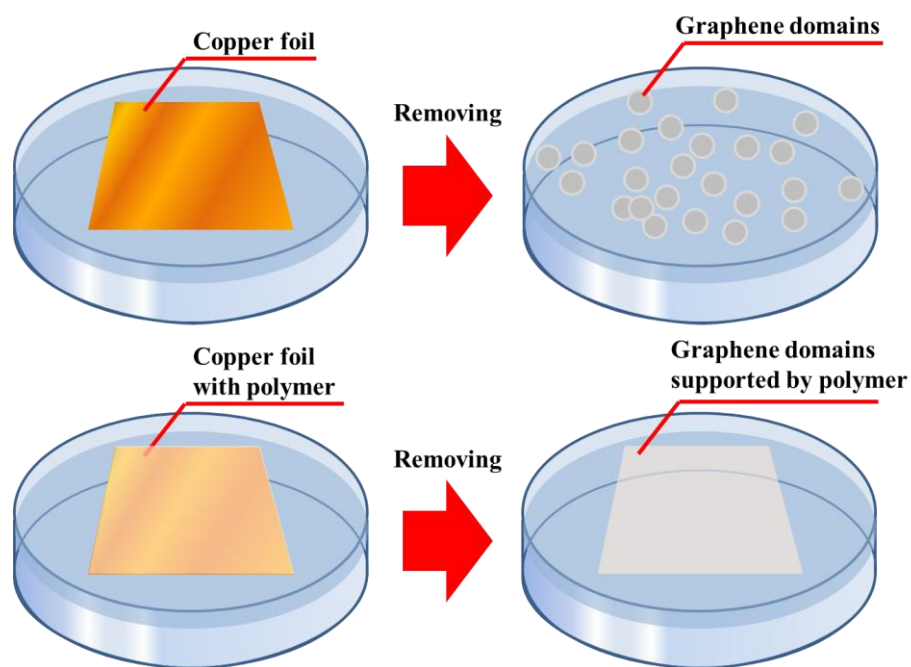


Figure 3-1: Images showing removal of the copper substrate. (A) shows graphene with domain boundaries and (B) shows graphene with domain boundaries supported by a polymer.

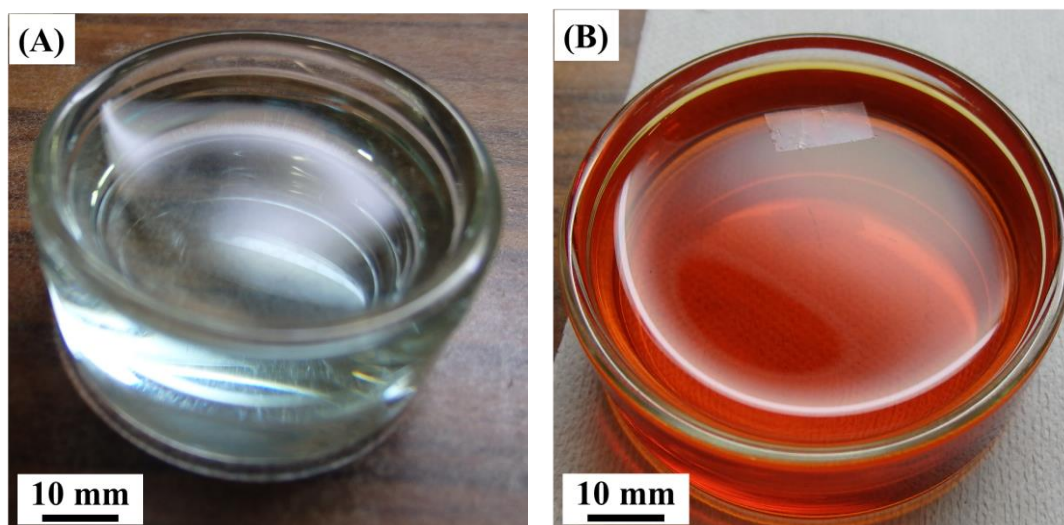


Figure 3-2: Photographs of the steps illustrated in Figure 3-1.

To date, synthesis of graphene directly onto a silicon substrate has been achieved. However, examples of the synthesis of graphene sheets directly suspended over slits in the substrate are negligible. It is extremely rare that the metal substrate disappears during graphene growth, forming the shape of a slit. Using these methods, it is difficult to apply the synthesized graphene as a liquid cell with a sandwich structure. Therefore, a transfer process is needed for the development of a graphene liquid cell for TEM observation of liquids.

3-2. **Transfer with polymer support**

We usually use poly(methyl methacrylate) and polycarbonate as the supporting polymer for transfer of graphene^[2, 15]. The two polymers can be removed easily because they have good solubility in many organic solvents. We use polymers in order to

evaluate the quality of the CVD-grown graphene, with the anticipation that the polymers will work as a graphene transfer support without cracking or creasing, even if the graphene does not cover the entire copper surface. In particular, we use the polymer transfer technique for analysis by Raman spectroscopy and electrical device measurements.

However, the polymer transfer technique has some critical issues that must be overcome before it is utilized industrially: the polymer cannot be completely removed, and the use of an organic solvent defiles the graphene surface. These problems may degrade the excellent properties of graphene. Currently, many researchers use mechanical exfoliation of graphite as a dry transfer technique for electric device fabrication since it is found that polymers damage CVD-grown graphene. Thus far, we have not succeeded in applying the dry transfer technique to CVD-grown graphene. Therefore, we have encountered difficulties in utilizing CVD-grown graphene due to issues with removing the polymer covering and the cost of wet transfer methods.

3-3. Transfer without support

To resolve the issues of the polymer transfer technique, we developed a new CVD-grown graphene transfer method that does not employ a polymer support. CVD-grown graphene is immediately dispersed into pieces upon removing the metal substrate if the graphene grains are not connected with each other. Previously, we believed that graphene could not be located by eye in order to be trapped on a substrate without a polymer, because our initially synthesized grains of graphene were too small to be observed.

However, we have now confirmed that free-standing graphene in the etching solution, without a polymer support, can be located due to the development of our pure hydrogen preannealing CVD method, which produces large, high-quality graphene sheets^[16-17]. By illuminating with a fluorescent lamp, we were able to distinguish the graphene surface from the etching solution surface due to their different reflectance. In the new transfer method, the transfer operation is completed by directly placing the substrate or TEM grid onto the graphene. Graphene prepared in this way has a clean surface with only a few contaminants that adhered to the graphene during CVD growth; no contamination arises from the transfer process.

3-4. **Experiment**

In the first stage of the transfer process, graphene on the backside of the copper foil (referred to as “backside graphene”) prepared by the above CVD growth method is removed by etching in $\text{Fe}(\text{NO}_3)_2$ aqueous solution. High-quality CVD-grown graphene usually covers the entire copper surface unless oxidization of a single side of the copper foil is performed or a silicon covering is added. As a result, backside graphene rolls up and adheres to the frontside graphene if the backside graphene remains on the copper surface. As high-quality graphene was usually produced, this trend was frequently observed. In addition, backside graphene often contains some of the etching solution. This is an undesirable consequence for TEM observation of liquids using graphene liquid cells, as the etching solution is observed in addition to the desired sample. The removal process is shown in following flowchart.

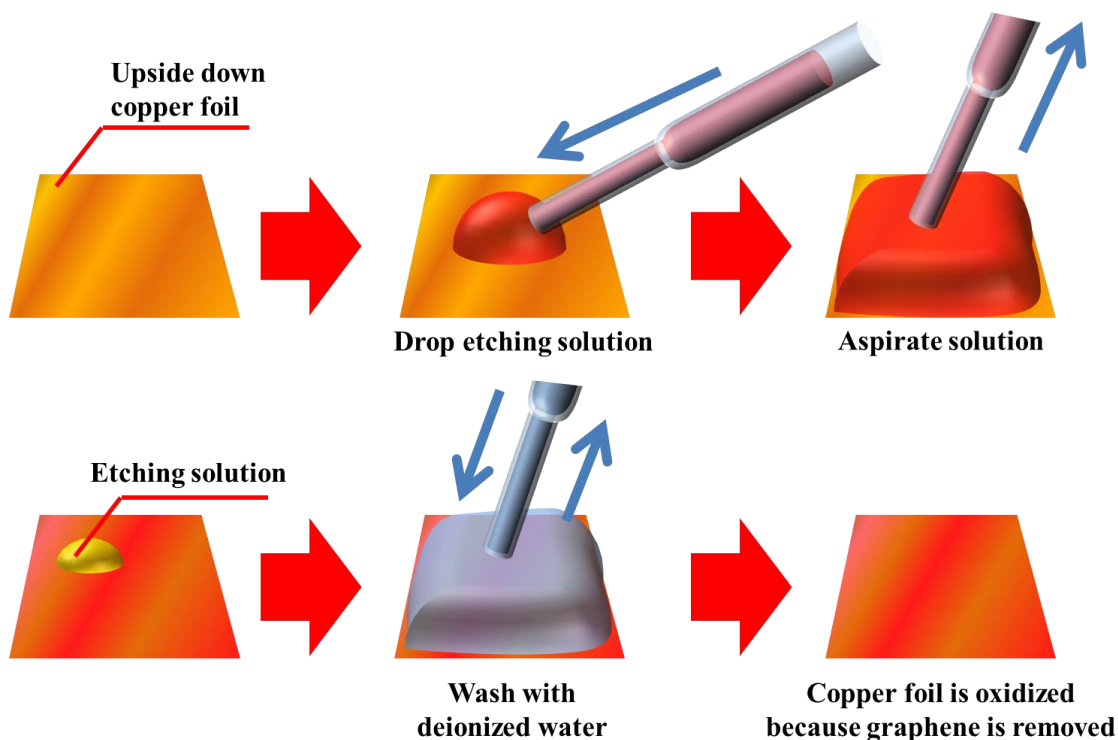


Figure 3-3: Flowchart illustrating the process of removing backside graphene.

First, the copper foil covered by graphene is put onto a piece of cotton upside down. Then 1.5 mol/L $\text{Fe}(\text{NO}_3)_2$ aqueous solution is carefully placed onto the back side of the copper foil by a Pasteur pipette to etch the copper surface. The etching solution invades the copper surface through graphene boundaries and damaged graphene at the same time. Graphene that has been separated from the substrate rises to the surface of the solution immediately. As graphene separates from the copper surface, the copper surface is oxidized by the etching solution. Almost all of the solution is aspirated by the Pasteur pipette in order to remove the metal residue that originated from the substrate and the solution. To completely remove the metal residue, deionized water is placed onto the copper surface in the same way as the etching solution. After repeated dropping and

aspiration with deionized water using the Pasteur pipette, the water changes color and becomes transparent. Finally, cotton is carefully placed onto the copper foil to dry the copper surface.

3-5. Results of the direct transfer method

To remove the copper substrate, a copper foil with a continuous film of graphene on the surface was placed in an aqueous solution of ammonium peroxodisulfate (1 mol/L) for 12 h. This process can remove the copper foil almost completely, leading to the graphene film floating on the surface of the etching solution. The graphene sheet floating on the etching solution is shown in Figure 3-4. The backside graphene was already removed by the technique described above. The graphene film was picked up by a SiN TEM grid, and then carefully placed into an aqueous solution of hydrochloric acid to remove copper residues.

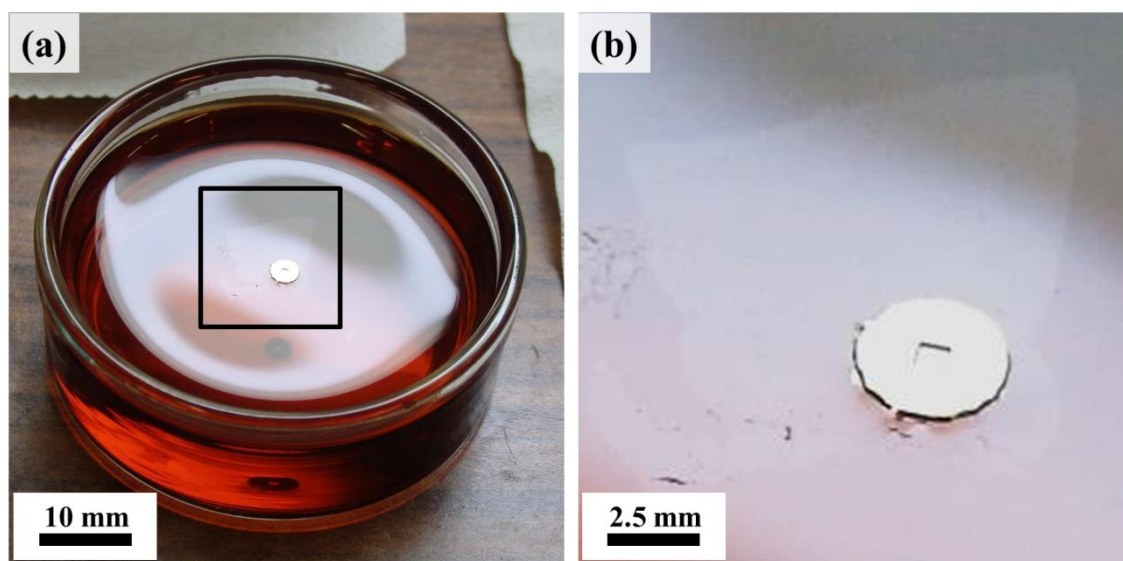


Figure 3-4: Photographs of the direct transfer process (a) and an enlarged view of the graphene monolayer floating on the etching solution (b) after removing the backside graphene.

The round yellow object is the TEM grid, which is placed onto the graphene sheet. It can be seen that the graphene sheet is approximately $10 \times 10 \text{ mm}^2$. For this figure, the graphene sheet was prepared using an aqueous solution of $\text{Fe}(\text{NO}_3)_2$ for demonstration,

instead of an ammonium peroxodisulfate solution. It is difficult to find, but there is a square graphene sheet on the solution.

Here, typical TEM images and electron diffraction patterns of the graphene obtained earlier by the direct transfer method are shown. In the low magnification image shown in Figure 3-5, regularly arranged holes in the SiN membrane can be seen. The diameter of the holes is 2 μm . Figure 3-5 is obtained by connecting the low magnification images. The SiN membrane suspended on the window of the grid can be seen. The graphene introduces no contrast compared with vacuum, but the cracked edges of the graphene can be observed. The linear cracks show the remaining backside graphene.

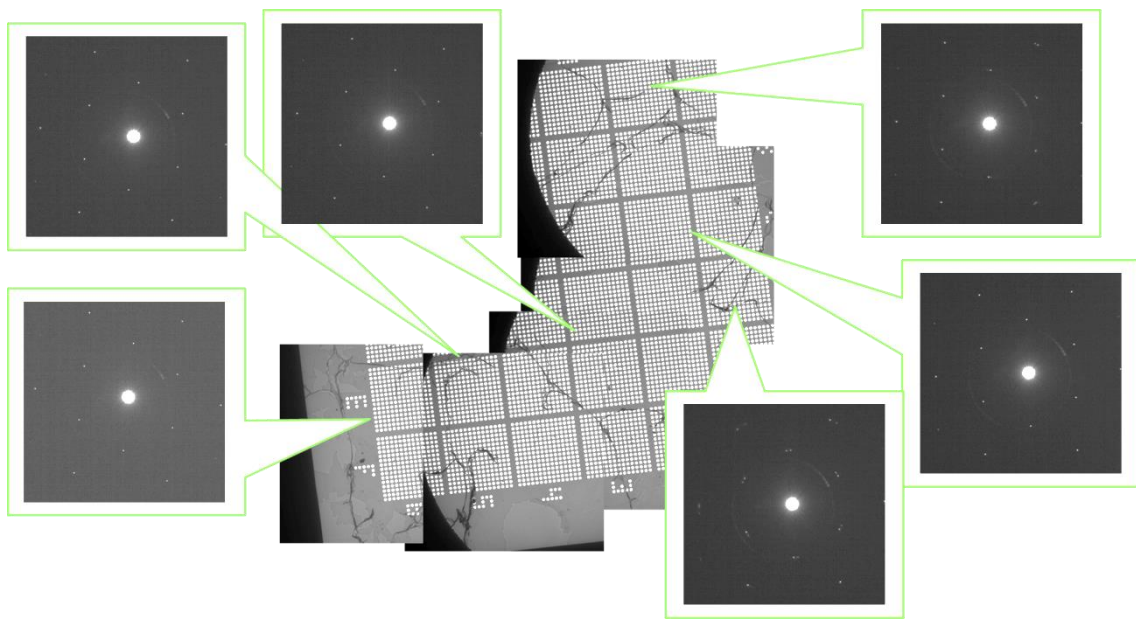


Figure 3-5: TEM images of graphene on a SiN grid and the corresponding electron diffraction patterns.

The electron diffraction patterns shown in Figure 3-5 exhibit six-fold symmetry, which confirms that large-sized single-layer graphene sheets were transferred to the TEM grid. The high-magnification images show that the graphene is clean and has almost no

contrast, except for some network-like amorphous carbon, as shown in Figure 3-6.

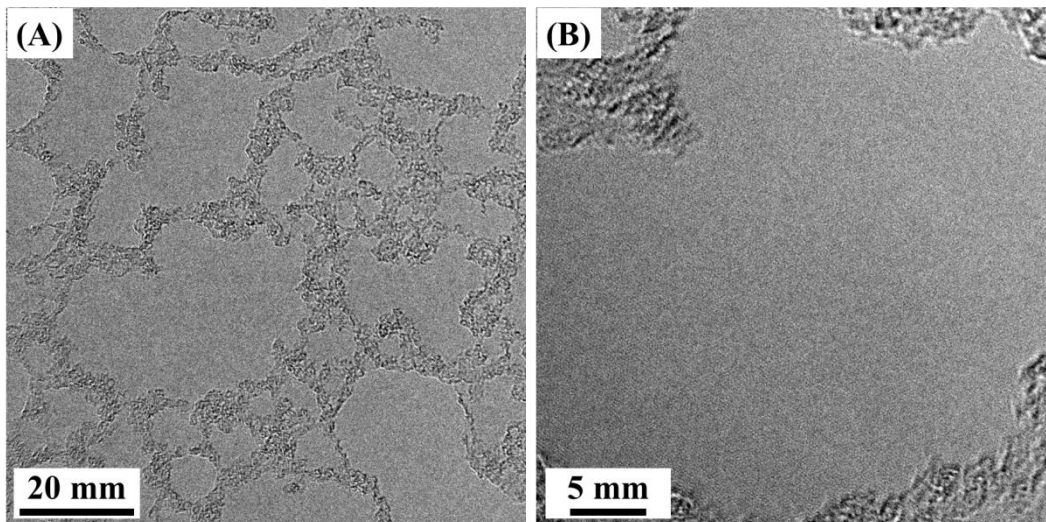


Figure 3-6: High-magnification images of graphene.

Figures 3-7A and 3-7B show EDX and EELS data for the graphene shown in Figure 3-6. We confirmed the carbon atom k-edge peak from each analysis and a few metal peaks were found in the EDX data. The silicon peak in the EDX data originates from the SiN TEM grid. Compared with EELS analysis, EDX yields information from a larger sampling area; hence, the EDX analysis covers not only the graphene but also the SiN membrane.

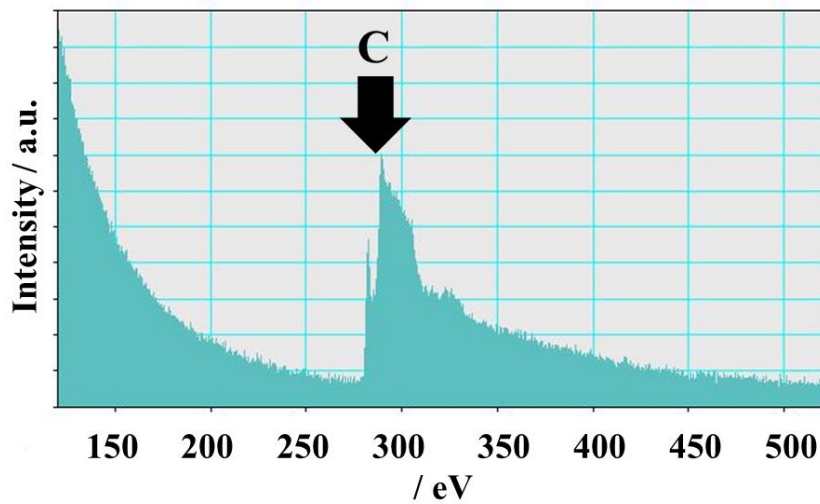
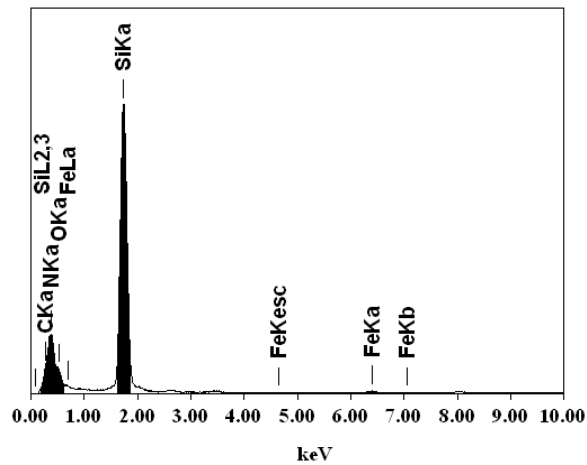


Figure 3-7: EDX and EELS data for the same region of Figure 3-6.

3-6. Preparation of the graphene-sandwiched structure

Our strategy for preparing a graphene liquid cell is a simple and direct sandwiching of CVD-grown graphene using the direct transfer technique. Figure 3-8 shows the preparation scheme for the graphene liquid cell.

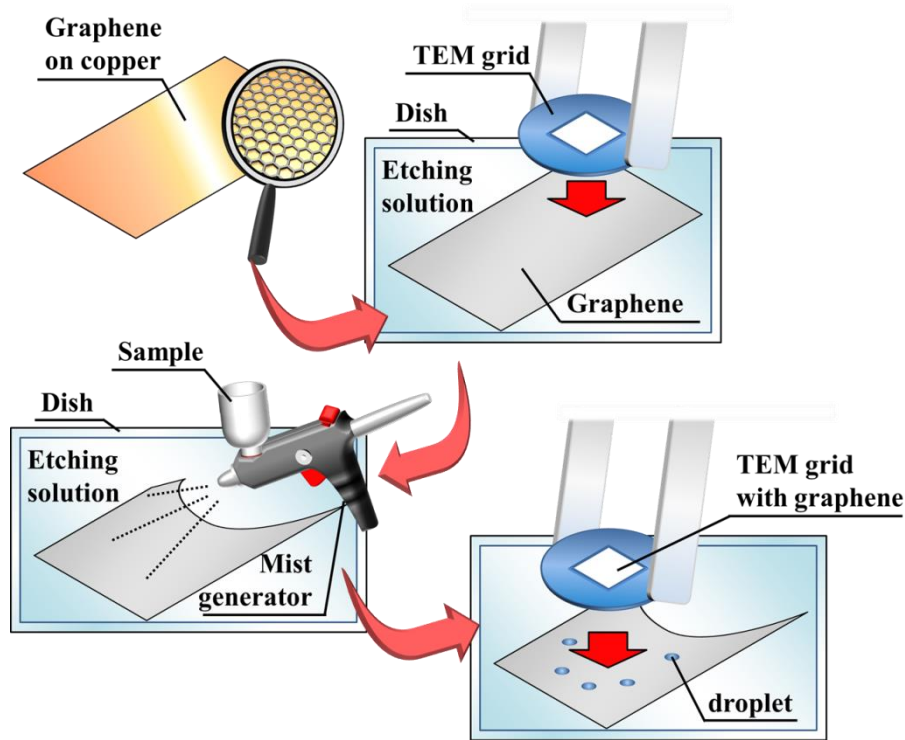


Figure 3-8: Preparation scheme for the grapheme-sandwiched structure.

First, CVD-grown graphene is transferred onto a SiN membrane grid with 2 μm holes penetrating through the membrane. Second, using a mist generator, various solutions are sprayed onto another graphene specimen floating on the etching solution. Third, to form a grapheme-sandwiched liquid cell, the deposited micro-size droplets of the solution are covered by the graphene-coated TEM grid. In the preparation of the graphene liquid cell, incorporation of large-area and seamless graphene layers is essential to realizing the successful encapsulation of solutions.

3-7. Results of the grapheme-sandwiched structure

The present preparation of the graphene liquid cell enables us to perform TEM

observations of the encapsulated liquids. Figure 3-9A shows a typical TEM image of a graphene liquid cell using the CVD-grown large-area graphene, where pure water droplets are used as the liquid encapsulated between the two single layers of graphene. The dark contrast region corresponds to the graphene–water-sandwiched area, with a lateral size of 160–300 nm. An estimated average thickness of the sandwiched region is 10–20 water molecule layers. Black spots seen in the TEM image are due to the copper nanoparticle residues, which were formed and deposited during the transfer process.

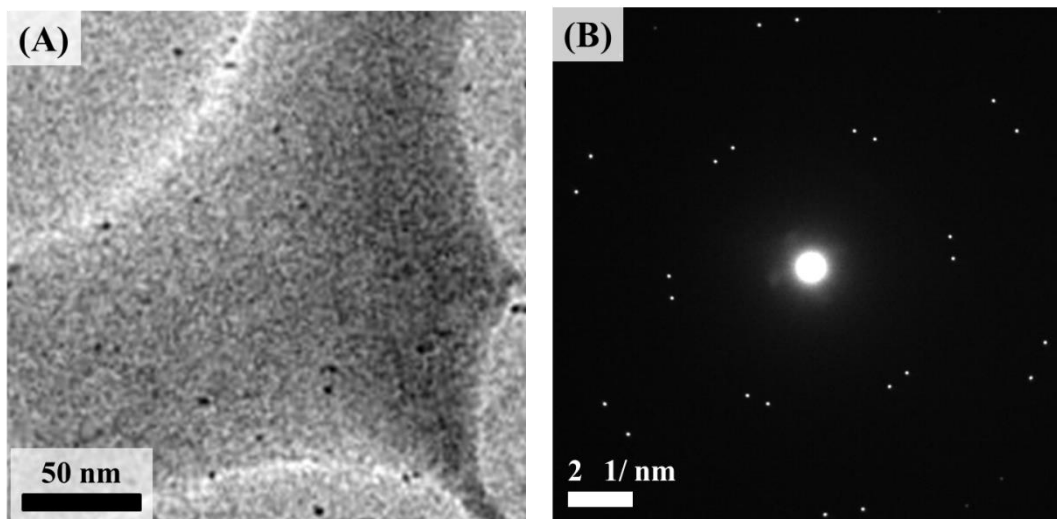


Figure 3-9: A typical room-temperature TEM image (A) of water sandwiched between two sheets of single-layer graphene (dark contrast region) and the corresponding electron diffraction pattern (B).

The corresponding electron diffraction pattern shown in Figure 3-9B exhibits two sets of diffraction spots with six-fold symmetry, which confirms the successful preparation of the graphene-sandwiched structure. The electron diffraction shows diffraction spots originating only from the graphene layers and not from the water droplet, suggesting a

liquid state of the droplet. The relative angle of the two hexagonal patterns is about 5° , indicating that two graphene sheets with a relative angle of 5° stack to form the graphene liquid cell. The relative angles in graphene liquid cells are found to vary from one sample to another due to random stacking caused by the manual stacking procedure used in the present preparation of graphene liquid cells.

To confirm the presence of the water droplet in the sandwiched structure, we performed EELS measurements on the sandwiched region. Figure 3-10 shows an EELS spectrum corresponding to the water-containing region shown in Figure 3-9A. The observed EELS peaks at $284^{[18]}$ and $540\text{ eV}^{[19-20]}$ originate from the core loss of carbon and oxygen, respectively. The existence of the EELS peak at 540 eV clearly illustrates the successful encapsulation of water molecules between the graphene layers.

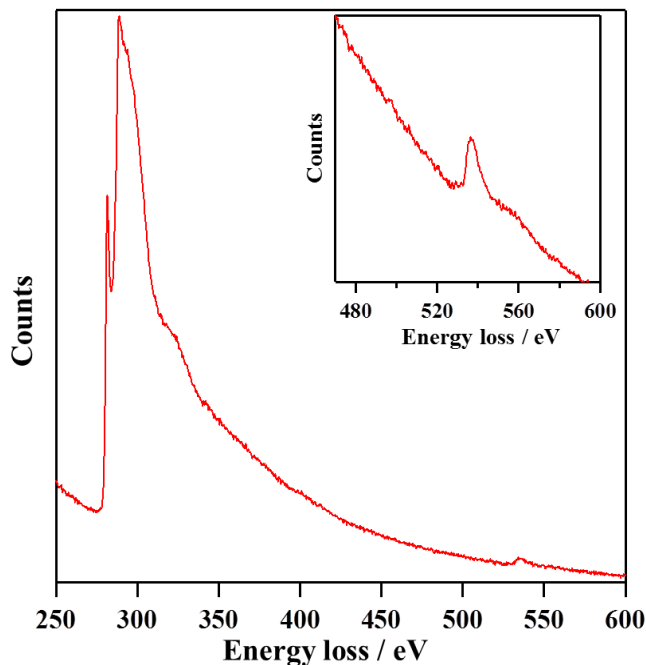


Figure 3-10: EELS spectrum with a selector aperture acquired for the graphene–water-sandwiched area in Figure 3-9.

3-8. **Conclusion**

In conclusion, we successfully fabricated a graphene-sandwiched structure by developing a direct transfer technique for use with high-quality graphene grown using the pure hydrogen treatment described previously. Compared with previously reported methods, we succeeded in simplifying the preparation process and improved the yield of graphene liquid cells. By utilizing our preparation technique for water, we were able to encapsulate water between the graphene layers. Similar sandwiching technique was reported by Yuk and Algara-Siller but our sandwiching process provides higher yield and smaller pockets of graphene liquid cell than their technique^[21-26]. Typically, small sandwiched droplets as small as 100 – 300 nm in size are observed by TEM. In our preparation, we found the average counts of small droplets is 10.2 per μm^2 and we confirmed that one TEM grid have approximately 224000 pockets in our preparation.

3-9. References

- [1] X. Li, W. Cai, J. An, S. Kim, J. Nah, D. Yang, R. Piner, A. Velamakanni, I. Jung, E. Tutuc, *Science* **2009**, *324*, 1312-1314.
- [2] X. Li, Y. Zhu, W. Cai, M. Borysiak, B. Han, D. Chen, R. D. Piner, L. Colombo, R. S. Ruoff, *Nano Lett.* **2009**, *9*, 4359-4363.
- [3] S. Bhaviripudi, X. Jia, M. S. Dresselhaus, J. Kong, *Nano Lett.* **2010**, *10*, 4128-4133.
- [4] Y. Lee, S. Bae, H. Jang, S. Jang, S.-E. Zhu, S. H. Sim, Y. I. Song, B. H. Hong, J.-H. Ahn, *Nano Lett.* **2010**, *10*, 490-493.
- [5] G. H. Han, F. Güneş, J. J. Bae, E. S. Kim, S. J. Chae, H.-J. Shin, J.-Y. Choi, D. Pribat, Y. H. Lee, *Nano Lett.* **2011**, *11*, 4144-4148.
- [6] X. Li, C. W. Magnuson, A. Venugopal, R. M. Tromp, J. B. Hannon, E. M. Vogel, L. Colombo, R. S. Ruoff, *J. Am. Chem. Soc.* **2011**, *133*, 2816-2819.
- [7] X. Liang, B. A. Sperling, I. Calizo, G. Cheng, C. A. Hacker, Q. Zhang, Y. Obeng, K. Yan, H. Peng, Q. Li, X. Zhu, H. Yuan, A. R. Hight Walker, Z. Liu, L.-m. Peng, C. A. Richter, *ACS Nano* **2011**, *5*, 9144-9153.
- [8] C. Mattevi, H. Kim, M. Chhowalla, *J. Mater. Chem.* **2011**, *21*, 3324-3334.
- [9] L. Zhao, K. T. Rim, H. Zhou, R. He, T. F. Heinz, A. Pinczuk, G. W. Flynn, A. N. Pasupathy, *Solid State Commun.* **2011**, *151*, 509-513.
- [10] L. Tao, J. Lee, H. Chou, M. Holt, R. S. Ruoff, D. Akinwande, *ACS Nano* **2012**, *6*, 2319-2325.
- [11] Y.-C. Chen, D. G. de Oteyza, Z. Pedramrazi, C. Chen, F. R. Fischer, M. F. Crommie, *ACS Nano* **2013**, *7*, 6123-6128.
- [12] Y. Hao, M. S. Bharathi, L. Wang, Y. Liu, H. Chen, S. Nie, X. Wang, H. Chou, C. Tan, B. Fallahazad, H. Ramanarayan, C. W. Magnuson, E. Tutuc, B. I. Yakobson, K. F. McCarty, Y.-W. Zhang, P. Kim, J. Hone, L. Colombo, R. S. Ruoff, *Science* **2013**, *342*, 720-723.
- [13] G.-H. Lee, R. C. Cooper, S. J. An, S. Lee, A. van der Zande, N. Petrone, A. G. Hammerberg, C. Lee, B. Crawford, W. Oliver, *Science* **2013**, *340*, 1073-1076.
- [14] K. Kim, Z. Lee, W. Regan, C. Kisielowski, M. F. Crommie, A. Zettl, *ACS Nano* **2011**, *5*, 2142-2146.
- [15] V. P. Verma, S. Das, I. Lahiri, W. Choi, *Appl. Phys. Lett.* **2010**, *96*, 203108.
- [16] Y. Sasaki, R. Kitaura, Y. Yamamoto, S. Arai, S. Suzuki, Y. Miyata, H. Shinohara, *Appl. Phys. Express* **2012**, *5*, 065103.
- [17] W. Regan, N. Alem, B. Alemán, B. Geng, Ç. Girit, L. Maserati, F. Wang, M. Crommie, A. Zettl, *Appl. Phys. Lett.* **2010**, *96*, 113102.

- [18] K. Suenaga, M. Koshino, *Nature* **2010**, *468*, 1088-1090.
- [19] U. Bergmann, P. Wernet, P. Glatzel, M. Cavalleri, L. Pettersson, A. Nilsson, S. Cramer, *PhRvB* **2002**, *66*, 092107.
- [20] C. Huang, K. T. Wikfeldt, T. Tokushima, D. Nordlund, Y. Harada, U. Bergmann, M. Niebuhr, T. Weiss, Y. Horikawa, M. Leetmaa, *Proc. Natl. Acad. Sci.* **2009**, *106*, 15214-15218.
- [21] G. Algara-Siller, O. Lehtinen, F. Wang, R. Nair, U. Kaiser, H. Wu, A. Geim, I. Grigorieva, *Nature* **2015**, *519*, 443-445.
- [22] J. M. Yuk, J. Park, P. Ercius, K. Kim, D. J. Hellebusch, M. F. Crommie, J. Y. Lee, A. Zettl, A. P. Alivisatos, *Science* **2012**, *336*, 61-64.
- [23] J. M. Yuk, Q. Zhou, J. Chang, P. Ercius, A. P. Alivisatos, A. Zettl, *ACS nano* **2015**.
- [24] M. Jeong, J. M. Yuk, J. Y. Lee, *Chem. Mater.* **2015**, *27*, 3200-3202.
- [25] C. Wang, Q. Qiao, T. Shokuhfar, R. F. Klie, *Adv. Mater.* **2014**, *26*, 3410-3414.
- [26] J. M. Yuk, H. K. Seo, J. W. Choi, J. Y. Lee, *ACS nano* **2014**, *8*, 7478-7485.

Chapter 4

4. TEM observation for liquids

4-1. Introduction

Electron microscope observation of liquids and solution-based materials is an important goal in nanometer-scale sciences^[1-20]. Direct structural information can give insights into fields such as biochemistry; for example, it can reveal the structures and motions of proteins in water. There have been observations of biomolecules that were quickly frozen in cryo-TEM^[21-25]. TEM combined with sophisticated 3D imaging techniques has revealed various functions of molecules, demonstrating that TEM observation is an effective new tool in biomolecular research. TEM has also enabled important studies in which real-time processes such as dissolution, precipitation, and reconstruction were observed. Using TEM to support these observations allows the capture of real-time, atomic-scale images, which makes it a powerful analysis tool for nanosized materials. Recent developments in aberration correction techniques have allowed atomic-scale observations with an acceleration voltage as low as 15 kV^[26], which is low enough not to destroy the sample. Electron microscopes require samples to

be placed in an ultrahigh vacuum, making it difficult to observe solutions that generally have a non-zero vapor pressure. In recent years, developments in cryo-holders and environmental cells have gradually made it possible to observe materials in solutions^[7, 27-28]. We have been developing a method for easily obtaining images of liquids with clearer contrast by using graphene liquid cells. In a previous report, we demonstrated the possibility of real-time TEM observation of nanosized ultrapure water droplets in vacuum by sandwiching them between graphene layers. In the studies with the graphene liquid cell, we occasionally observed hexagonal ice lattices. When bubbles are generated as the water vaporizes, the trace amount of water in the corners of a cell pocket turned into ice. The structure of the ice is different from that of the cubic ice reported by Algara-Siller *et al.*^[29], and there are few materials with similar crystal structures^[30-31], indicating with high probability that ice is produced. Interestingly, the observation was conducted at room temperature and it is surprising that the water turns into hexagonal ice even under heating caused by the electron beam. The ice was not observed when ultrapure water was encapsulated, but only when water of a relatively low purity was used, such as deionized water, in which the existence of impurities at a relatively high concentration was confirmed. We thus hypothesized that this ice is stabilized by metals, and examined the phenomenon both experimentally and with calculations. We investigated the mystery of water solidification by comparing two types of water encapsulated between the graphene layers: ultrapure water and water mixed with gold, which is hardly oxidized and expected to cause charge transport.

4-2. Water at room temperature

First, we show TEM images of pure water encapsulated inside a graphene pocket, which confirms our success in producing the grapheme-sandwiched structure. Figure 4-1 shows a time series of magnified TEM images of a sandwiched water droplet at room temperature.

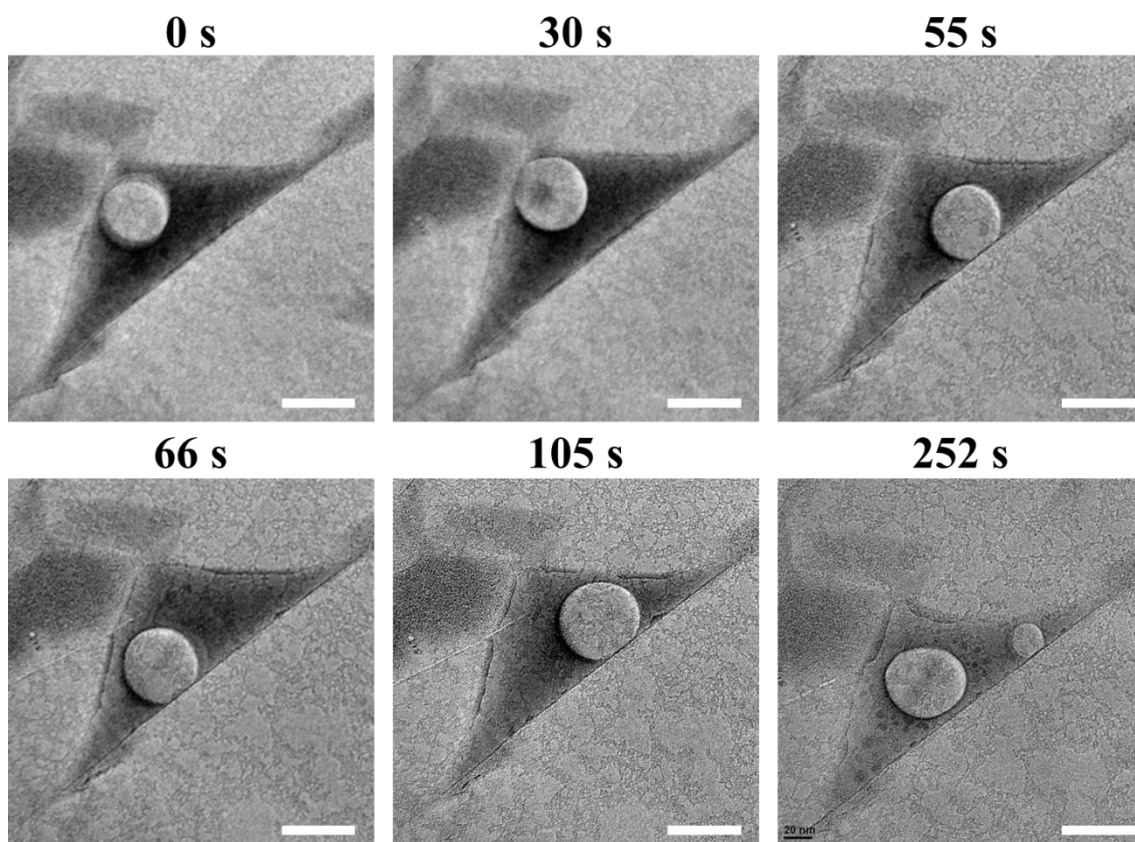


Figure 4-1: Time series of room-temperature TEM images of water sandwiched between graphene sheets (triangular dark contrast area) with a scale bar of 50 nm.

The triangular dark contrasts shown in the figure correspond to the water droplet sandwiched between two sheets of graphene. The electron diffraction image in Figure

4-2 shows spots originating only from the graphene layers, which is consistent with the liquid state of the encapsulated water. Importantly, the contrast in the water-sandwiched region decreases with time due to the increasing extent of vaporization of the water droplet (due to electron-beam-induced radiolysis) in the graphene pocket^[3]. As seen in these TEM images, a bubble corresponding to the circular low-contrast area, which is presumably generated by electron beam irradiation, is observed in the sandwiched region. At 252 s, a second (smaller) bubble appears in the sandwiched region. These bubbles are frequently observed in the water-sandwiched regions during the course of TEM observations. The TEM observation shown here demonstrates that the time-dependent dynamics of liquid water droplets can be observed at the nanometer scale using the graphene-sandwiched structure.

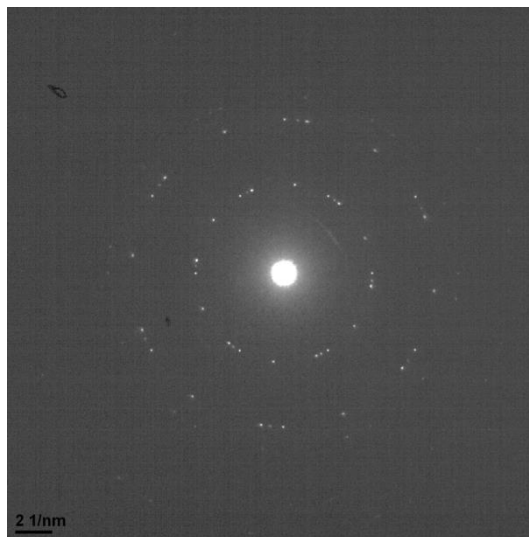
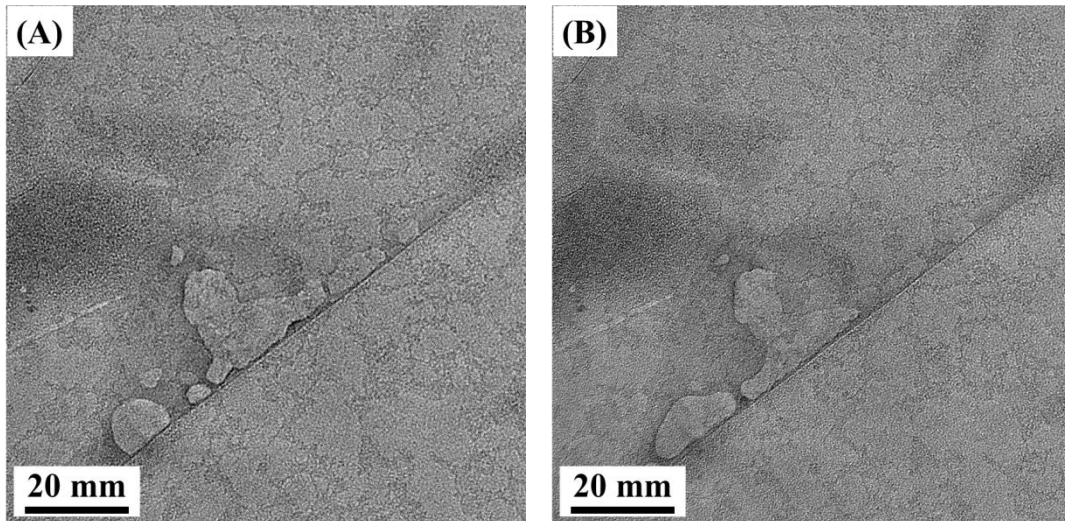


Figure 4-2: Electron diffraction image of the graphene liquid cell shown in Figure 4-1.

We also found some residues from the liquid cell, as shown in Figure 4-3. These

images were acquired 7 min later when we started to observe Figure 4-1. The contrast located in the pocket in Figure 4-3B is different from that in the pocket in Figure 4-3A due to the existence of water inside the pocket. The detailed structure of the residues is clearly observed in Figure 4-3B because there is less water in the pocket. According to the EELS spectrum in Figure 4-3B, these residues consist of carbon and some oxygen atoms. It is reasonable to consider that the amorphous carbon network on the graphene was introduced as a residue during the grapheme-sandwiching process.



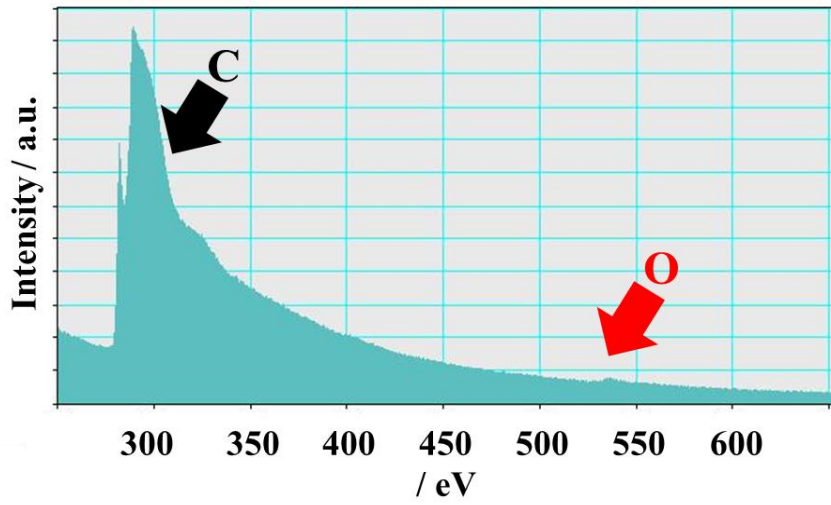
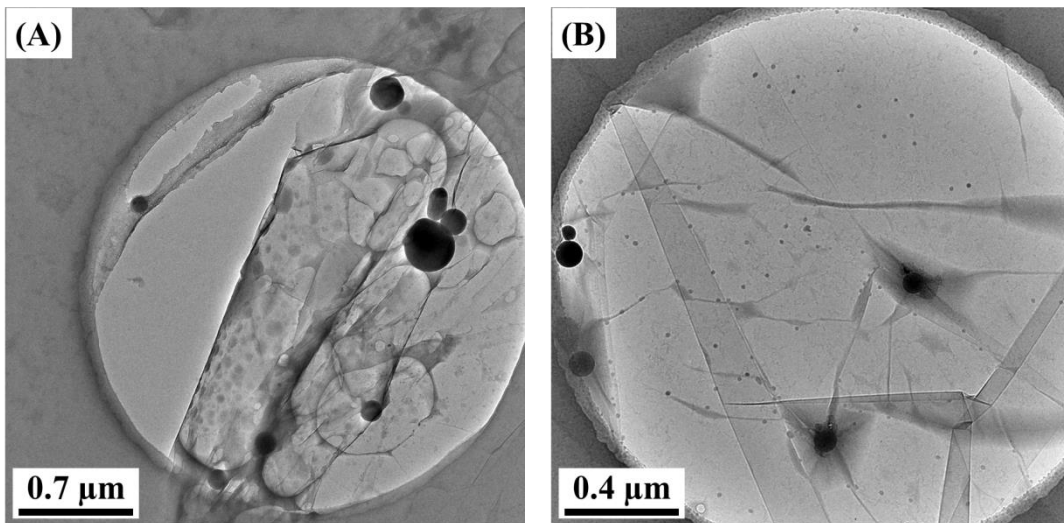
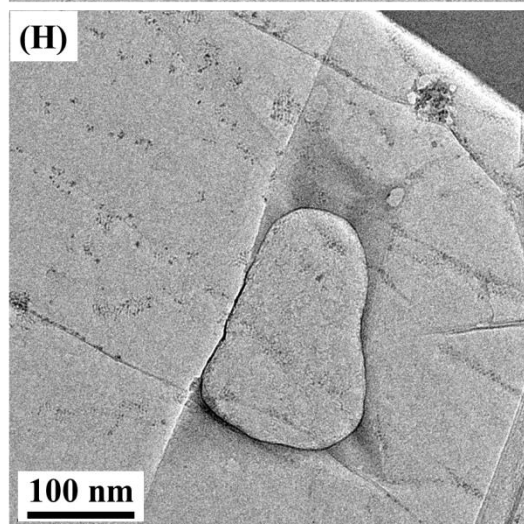
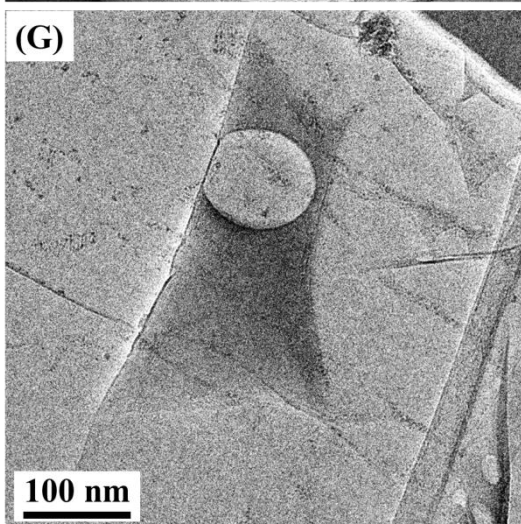
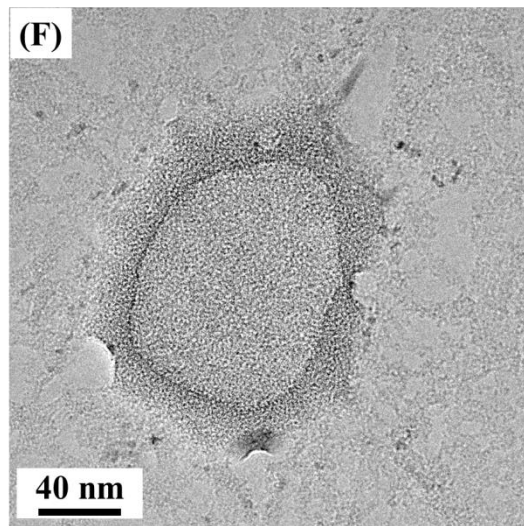
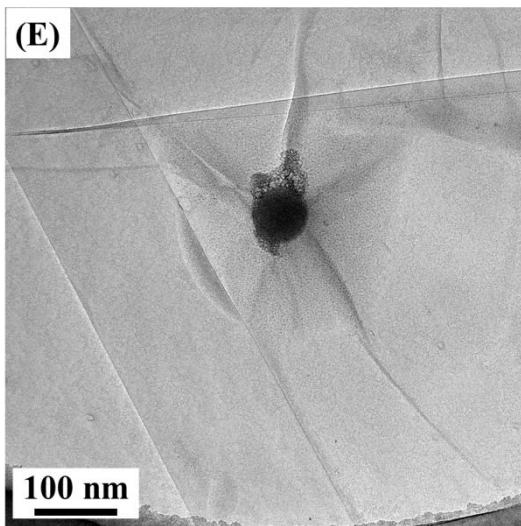
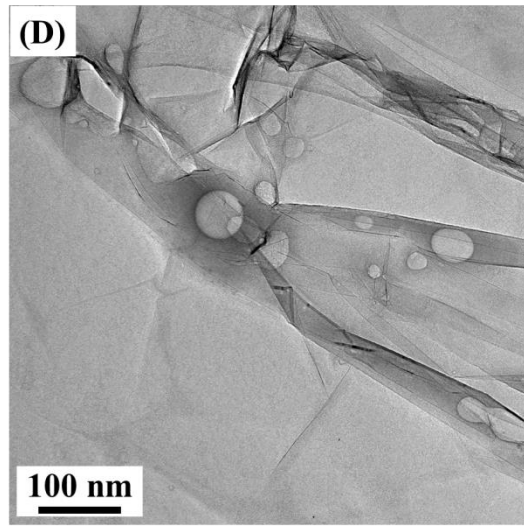
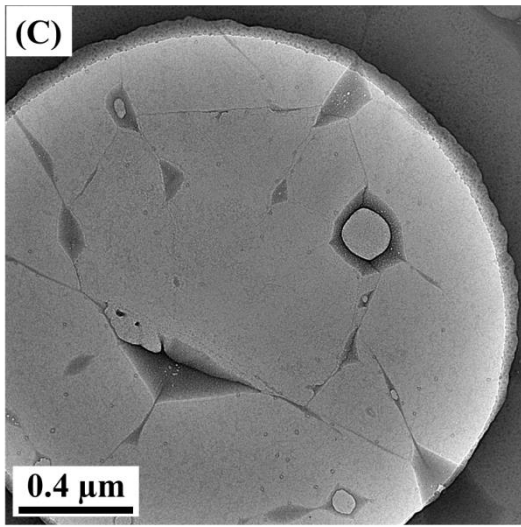


Figure 4-3: Residues of Figure 4-1 after vaporization of water and the EELS spectrum of Figure 4-3B.

Other typical TEM images of water encapsulated in the graphene liquid cells are shown in Figure 4-4. Various shapes of liquid cells were observed, and they often left some residue after vaporization induced by electron beam irradiation.





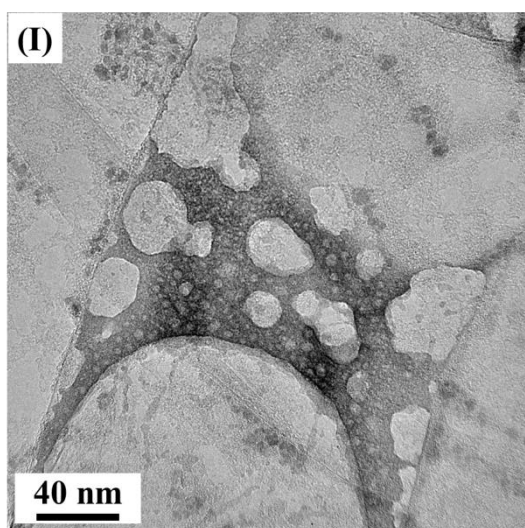


Figure 4-4: Typical TEM images of water encapsulated in graphene liquid cells.

Figures 4-4G, 4-4H, and 4-4I show the typical vaporization of water inside graphene liquid cells. The amorphous structure observed in Figure 4-4I is similar to that observed in Figure 4-3B, but Figure 4-4I shows stronger contrast compared with Figure 4-3B. We found that the region shown in Figure 4-4I contained copper residue, which originated from the substrate of the CVD growth, which is observed as the dark contrast in Figure 4-4I. In rare cases, we found no vaporization residue, as shown in Figure 4-5.

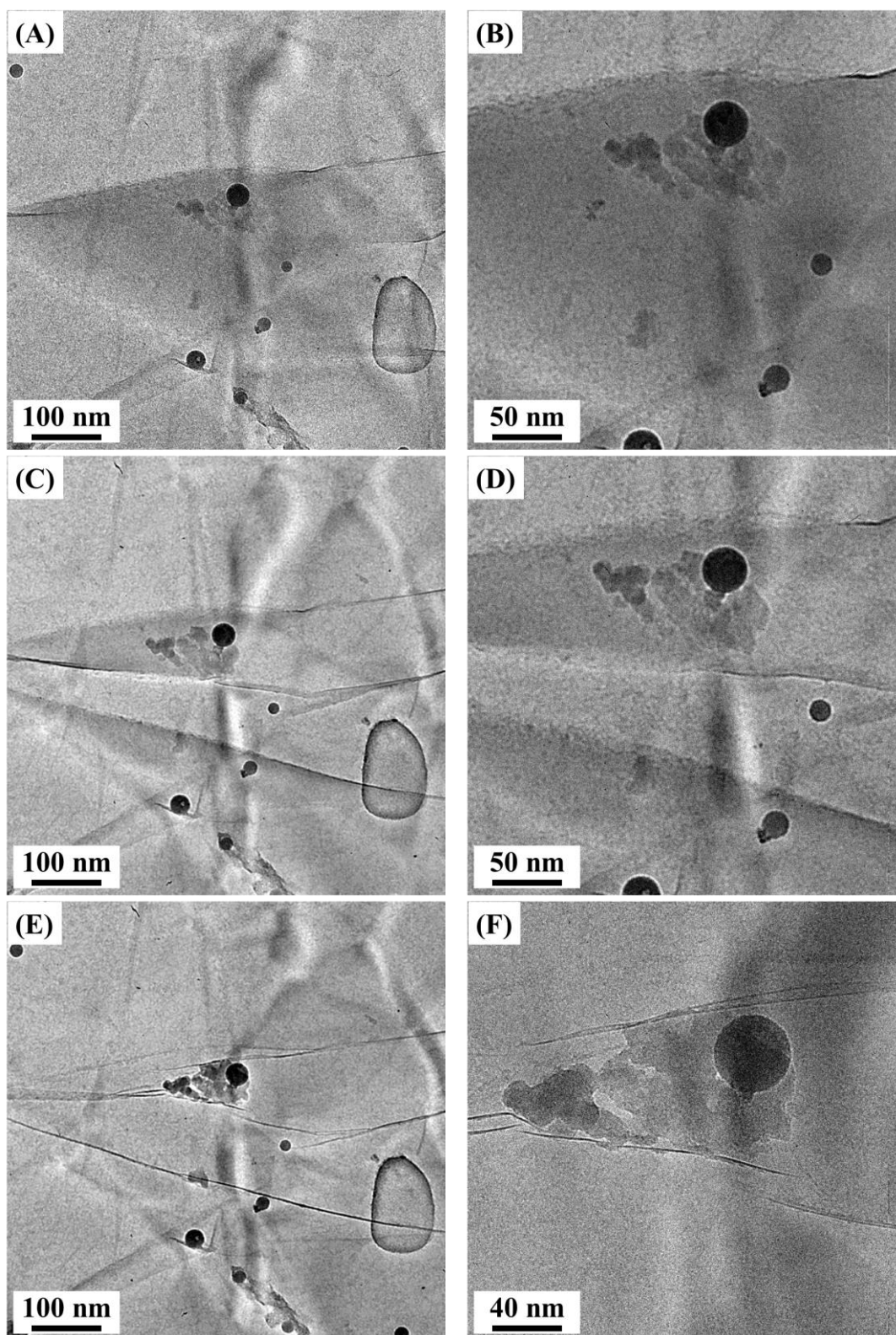


Figure 4-5: TEM images of a graphene liquid cell.

These images are all acquired at the same position. Figures 4-5A, 4-5C, and 4-5E show low-magnification images and Figures 4-5B, 4-5D, and 4-5F show higher-magnification images. Figures 4-5A and 4-5B, 4-5C and 4-5D, and 4-5E and 4-5F are, respectively, acquired at the same moment. In Figures 4-5C and 4-5D, the top and bottom graphene layers located at the center of the images were stacked on top of each other because the filling water has gone away through the small gap between the two graphene layers. In Figures 4-5E and 4-5F, almost all of the water has disappeared. The dark contrast, which appears as a sphere, was determined by EELS to be silicon oxide and was left between the graphene layers. Finally, the graphene formed a tent-like shape so as to surround the sphere of silicon oxide. According to Figure 4-5F, no residues with amorphous structure formed in the graphene pocket in this liquid cell.

Relating to the environmental condition, we consider about pressure inside graphene liquid cell. The pressure between graphene layers should be caused from van der Waals interaction of two graphene layers. We guessed pressure of liquid cells with considering van der Waals interaction as shown in figure 4-6. The energy by attractive force is shown in purple line and the energy by repulsive force is shown in green line. The red line means summation of attractive and repulsive energies. The blue line is obtained by differentiating of the red line. By changing graphene-graphene distance and by scanning the pocket size, we estimate the pressure in graphene layer without water molecules. In following graphs, we illustrate the cross section image of bilayer graphene in figure 4-7.

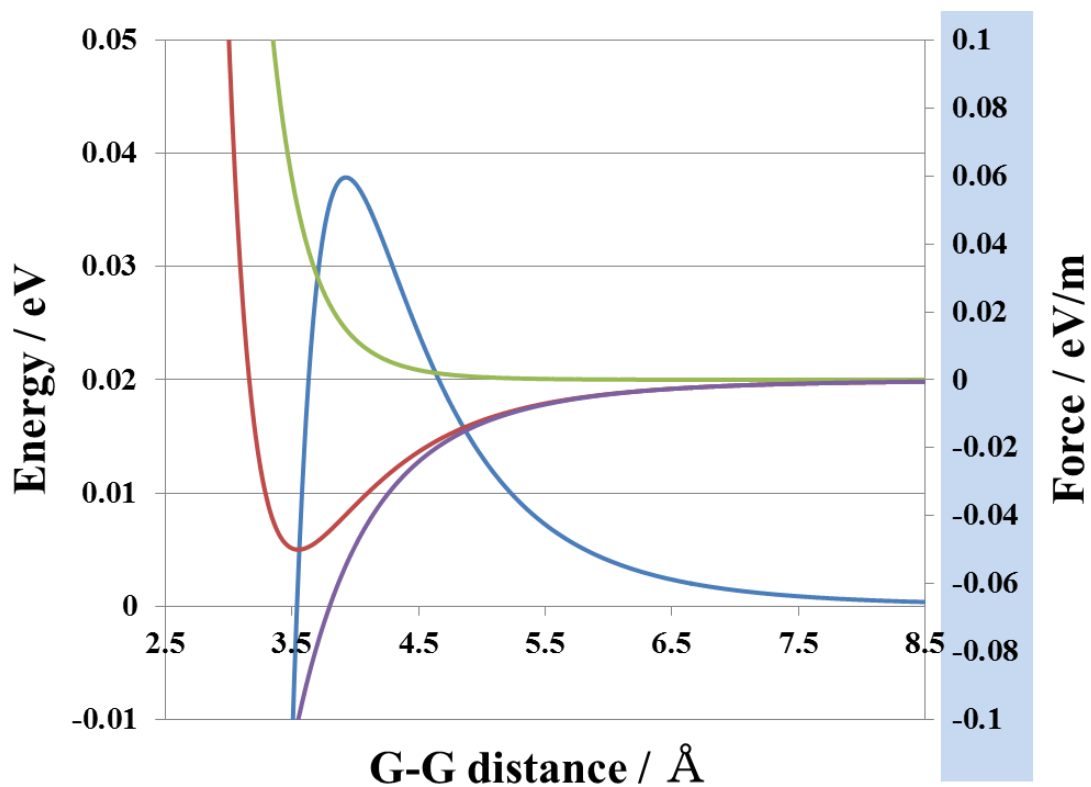
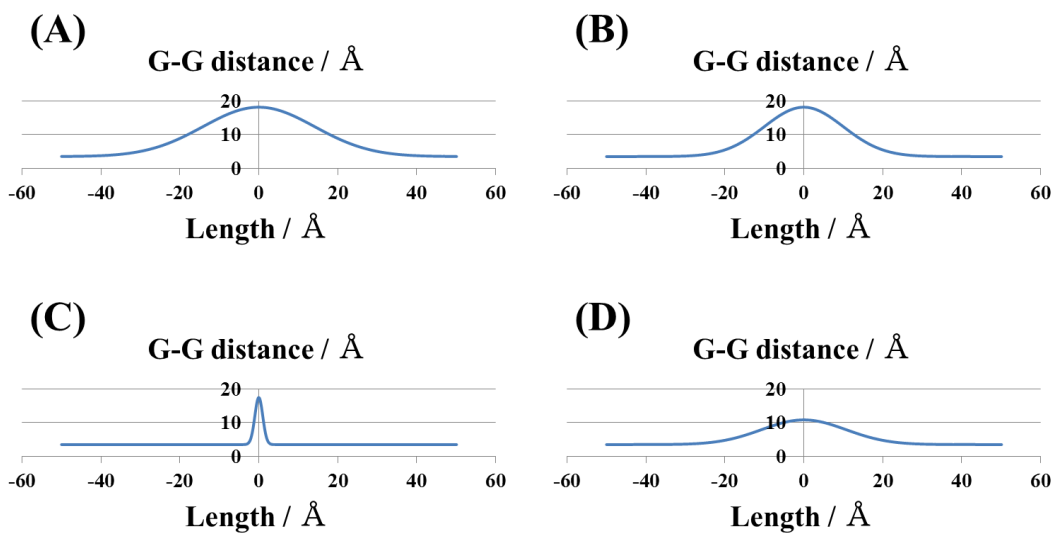


Figure 4-6 : Poetical energy of graphene layers by van der Waals interaction.



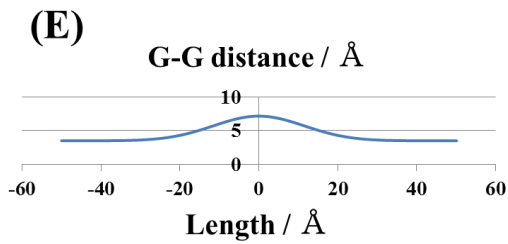


Figure 4-7 : Cross section of bilayer graphene having various thickness and half width, which means size of graphene liquid cells.

We calculated the pressure regarding each graph with van der Waals interaction. In the results, graph A is calculated 415 MPa, B is 435 MPa, C is 466 MPa, D is 530 MPa, and E is 613 MPa, respectively. In this result, we got the graph, which shows the relationship between the graphene-graphene distance and pressure as shown in figure 4-8. Importantly, the pressure is 700 MPa at the highest estimate.

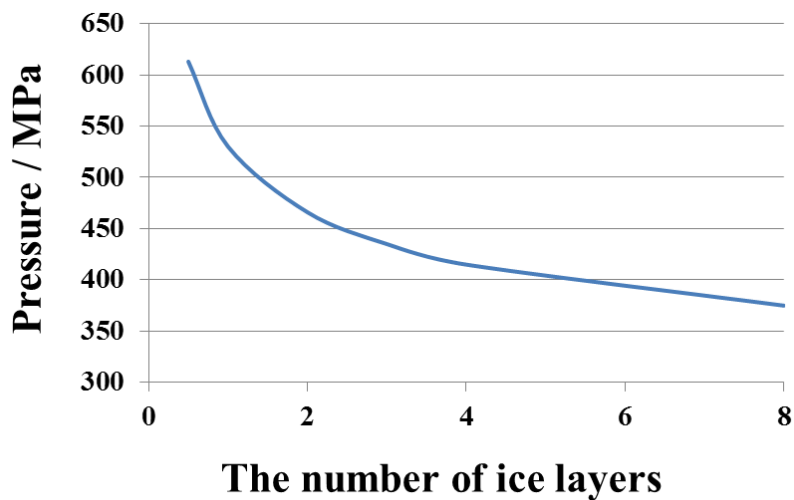
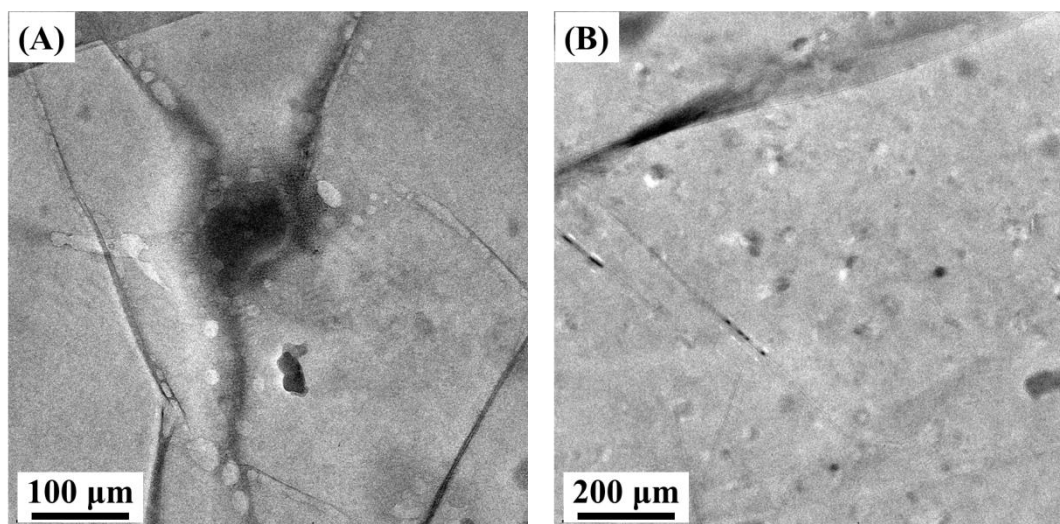


Figure 4-8 : Relationship of graphene-graphene distance and pressure inside graphene liquid cell.

4-3. Water at 77 K

At 273 K and atmospheric pressure normal water should freeze immediately. We expect that water encapsulated inside a graphene-sandwiched liquid cell freezes at low temperature, and observations were performed assisted by the cooling TEM holder. The cooling TEM holder conducts heat from the TEM grid to the bottle, which is stored in a liquid nitrogen refrigerant. Thus, we can observe samples at approximately 77 K, which is the boiling point of liquid nitrogen. Here, we show typical images of graphene liquid cells at 77 K in Figure 4-9.



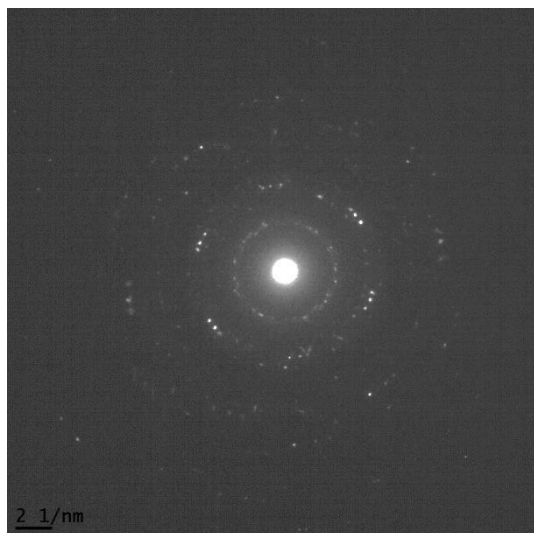
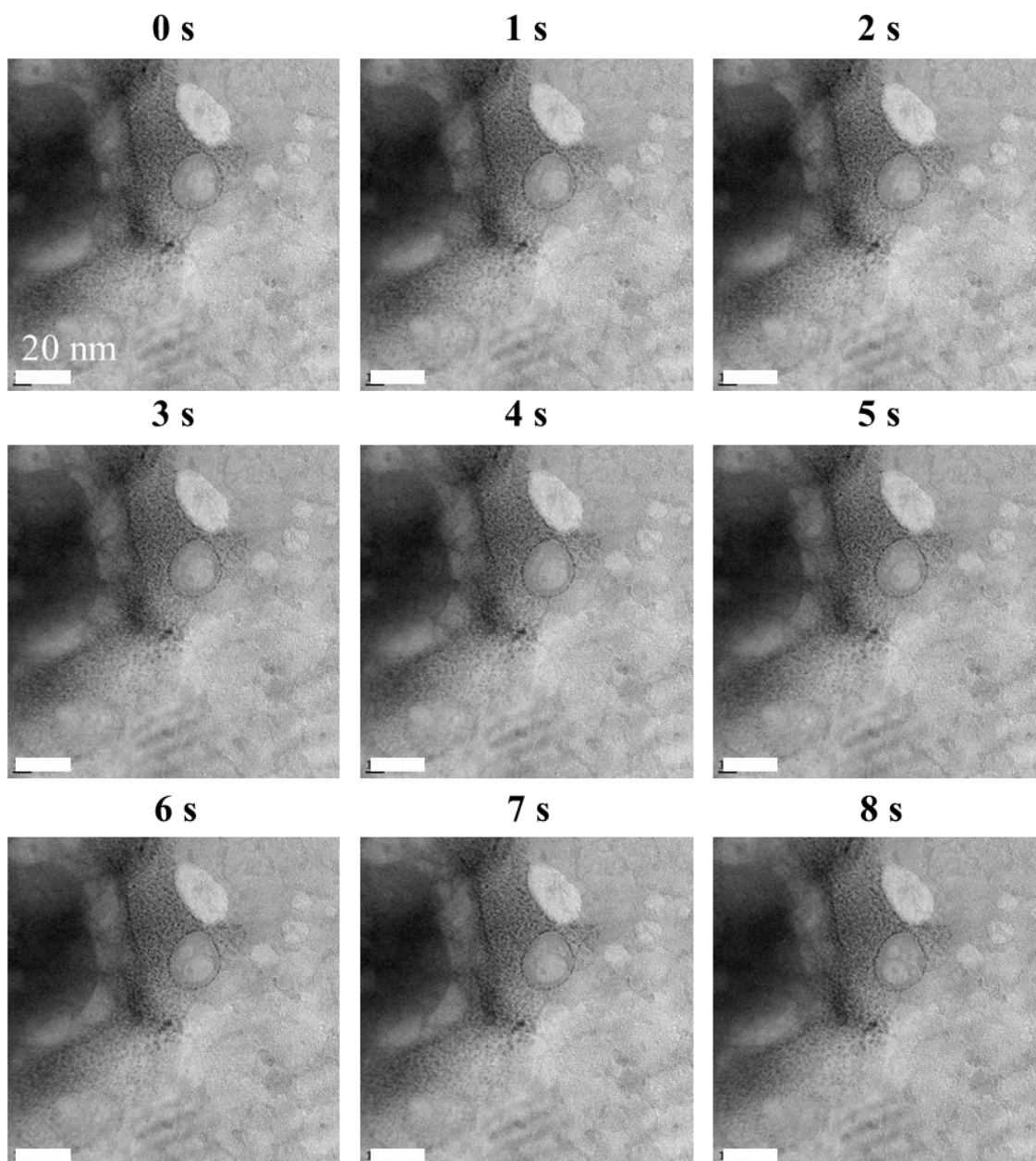


Figure 4-9: Typical TEM images of liquid cells at 77 K and the electron diffraction pattern of B.

We found that some ice crystals appeared from the TEM lens barrel. This ice is not inside the graphene liquid cell, but on the graphene layer, because it can be removed more easily than water encapsulated inside the graphene liquid cell by electron beam irradiation. The existence of ice suggests that the TEM grid was cooled to at least 250 K, according to the phase diagram of water at 10^{-5} Pa.

Figure 4-10 shows the time series of magnified images from Figure 4-9A. The exposure time was 0.5 s, and each image was acquired once per one second. Images were arranged in order of increasing time starting from the left. Importantly, we found that water inside the graphene liquid cell does not form ice, which has a lattice structure. Dark spots of contamination moved slowly due to the high current density of the electron beam. Bubbles from the water disappeared when we lowered the electron beam brightness, as shown in Figure 4-10 parts 16, 17, and 18. There is a possibility that liquid water inside the graphene liquid cell freezes to ice at 77 K, but ice is melted by

electron beam irradiation during the TEM observation. However, we do not have any analysis technique that can confirm the existence of microscopic amounts of ice without using electron beam irradiation.



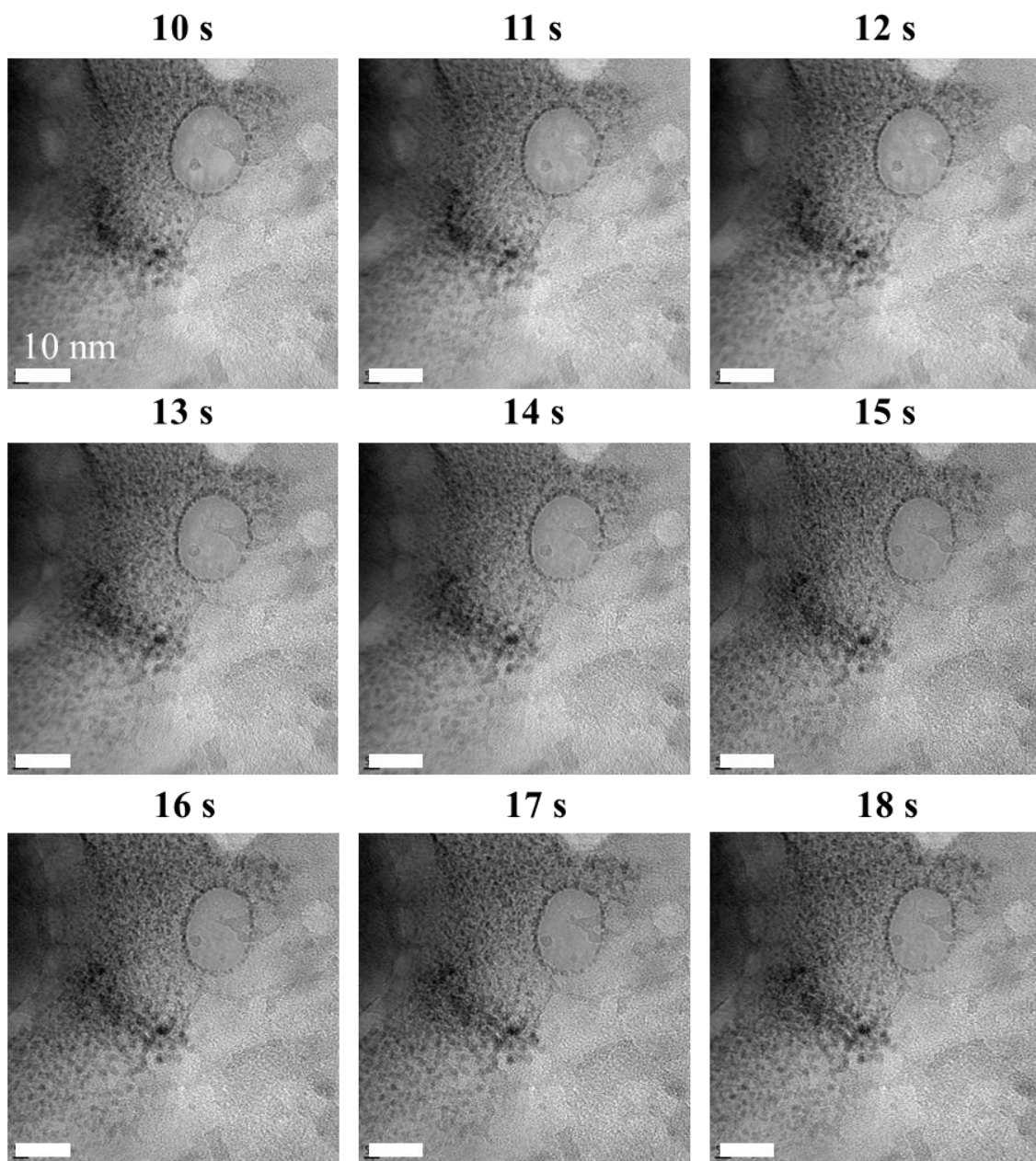


Figure 4-10: Time series of liquid cells at 77 K.

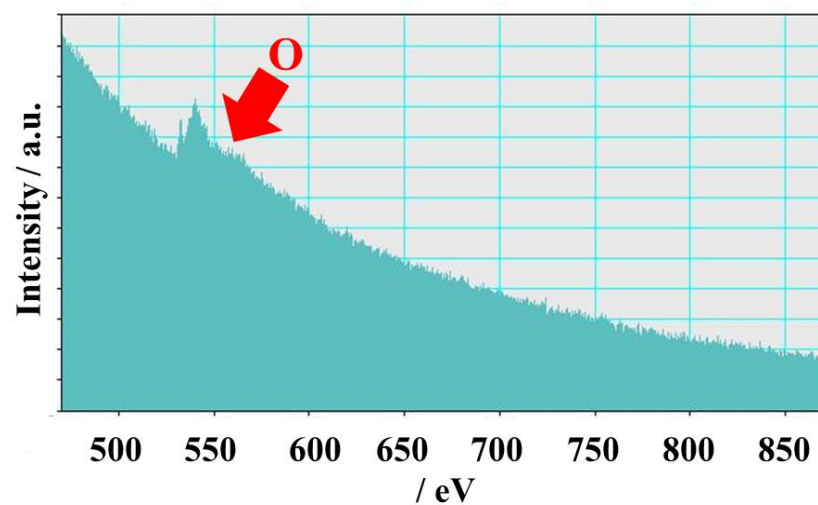


Figure 4-11: EELS spectrum corresponding to Figure 4-9A.

The EELS spectrum corresponding to Figure 4-9A is shown in Figure 4-11. We found that the oxygen k-edge peaks at higher energy than in the normal liquid cell shown in Figures 3-10 and 4-3 because this sample has normal ice on the graphene. It is consistent with the X-ray analysis of ice and water^[19, 32-33].

In Figure 4-12, other TEM images show clusters that have no lattice structure or constant in the same liquid cell shown in Figure 4-9A. A large cluster with dark contrast is found at the center of the images, and smaller clusters that repeatedly appear and disappear are localized at the left side of the larger cluster. These clusters seem like crystals but they do not have any lattice pattern according to the TEM images and the electron diffraction patterns. Presumably, these clusters are composed of metal ion hydrate crystals, quickly exchanging their water molecules with each other. It is quite difficult to prevent contamination, even if we prepare samples carefully using ultrapure water. Therefore, a small number of crystal nuclei that cannot be detected by EELS

analysis can contaminate the graphene liquid cell.

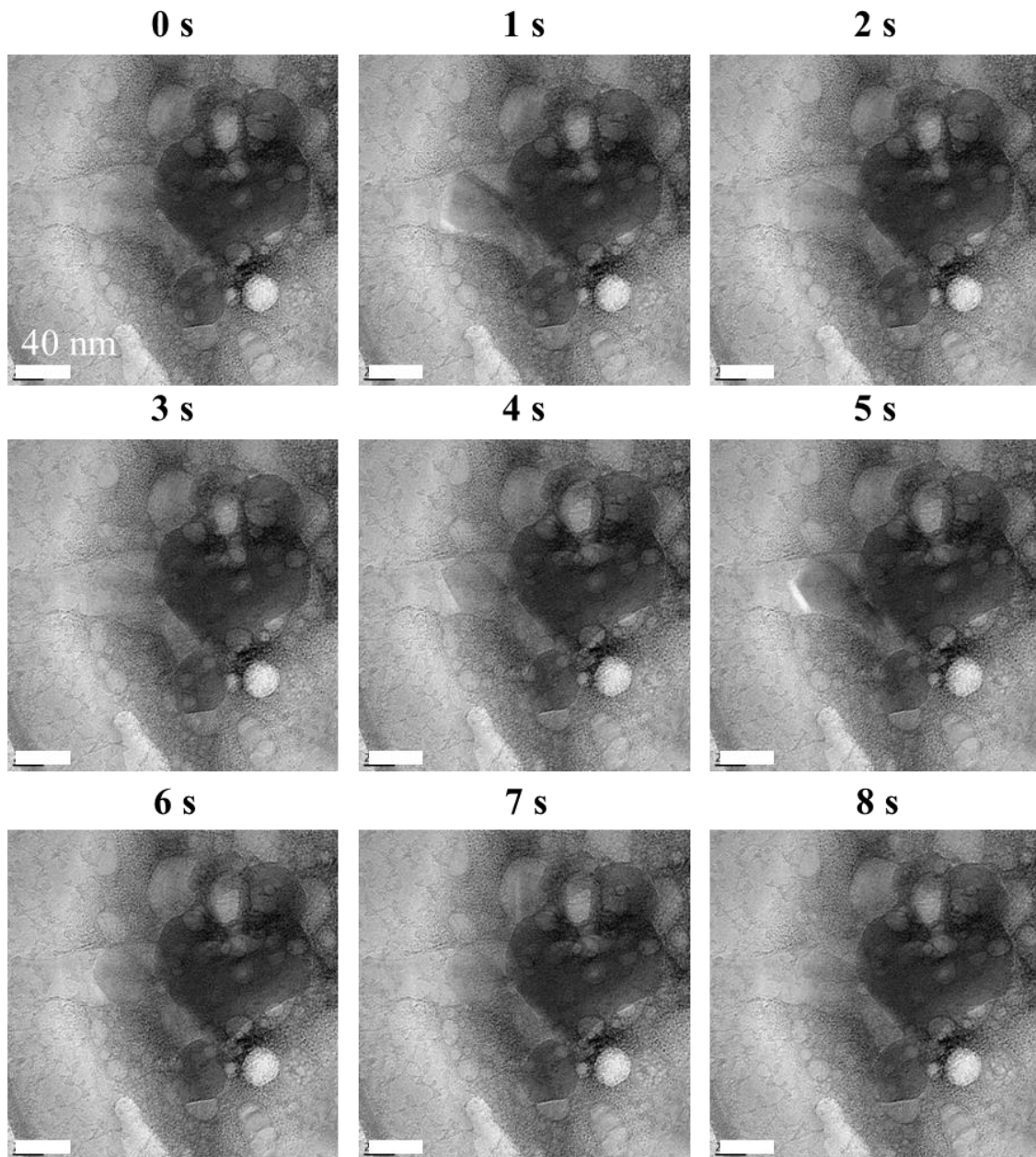


Figure 4-12: Time series of TEM images of clusters.

4-4. Aqueous solution of iron nitride

In our previous work, we succeeded in encapsulating water between graphene layers. Here, we go on to demonstrate various solutions encapsulated inside the graphene liquid cell in order to show the versatility of the graphene liquid cell applied to TEM observations. In this section, we show that the iron nitride aqueous solution is certainly encapsulated by our sandwiching process.

Figure 4-13 shows typical TEM images of encapsulated iron nitride aqueous solution.

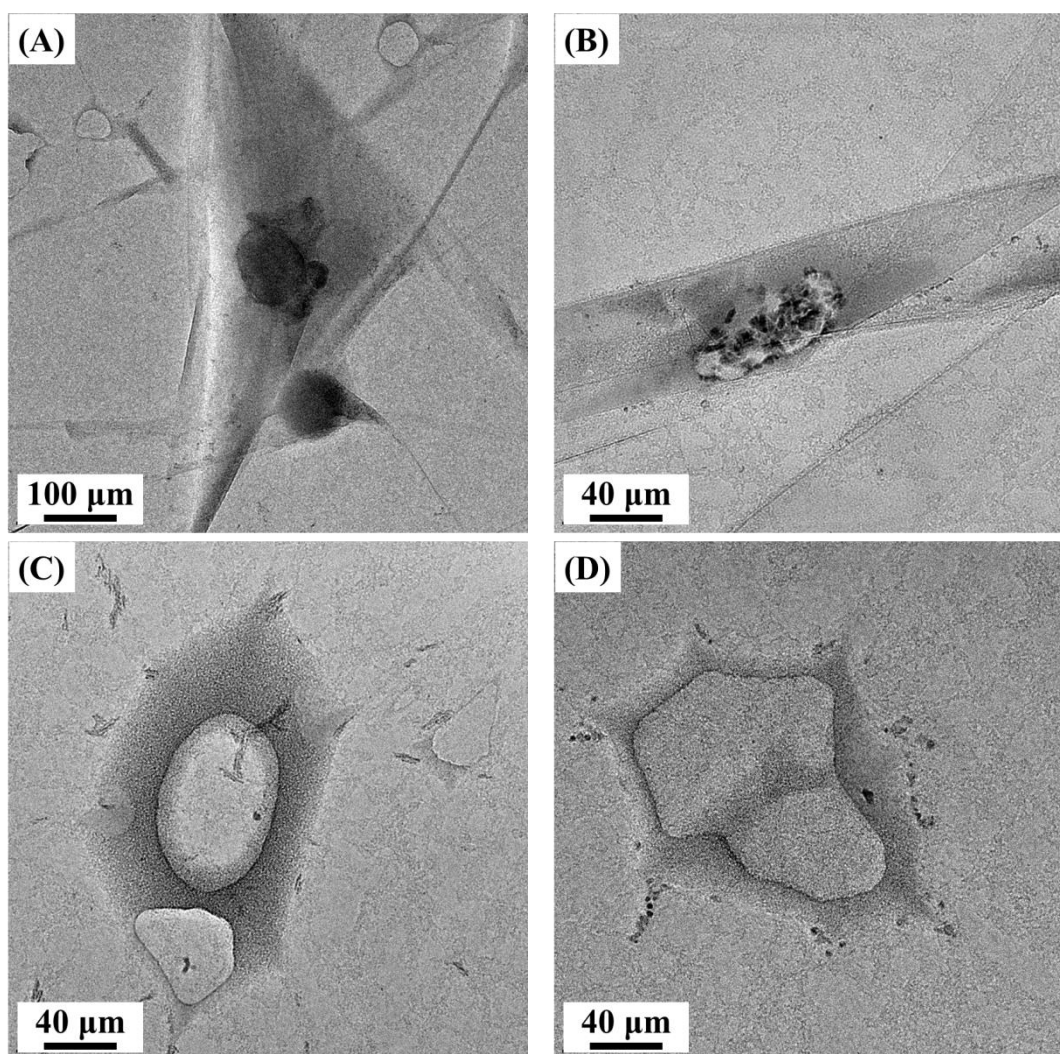


Figure 4-13: Typical TEM images of iron nitride aqueous solution.

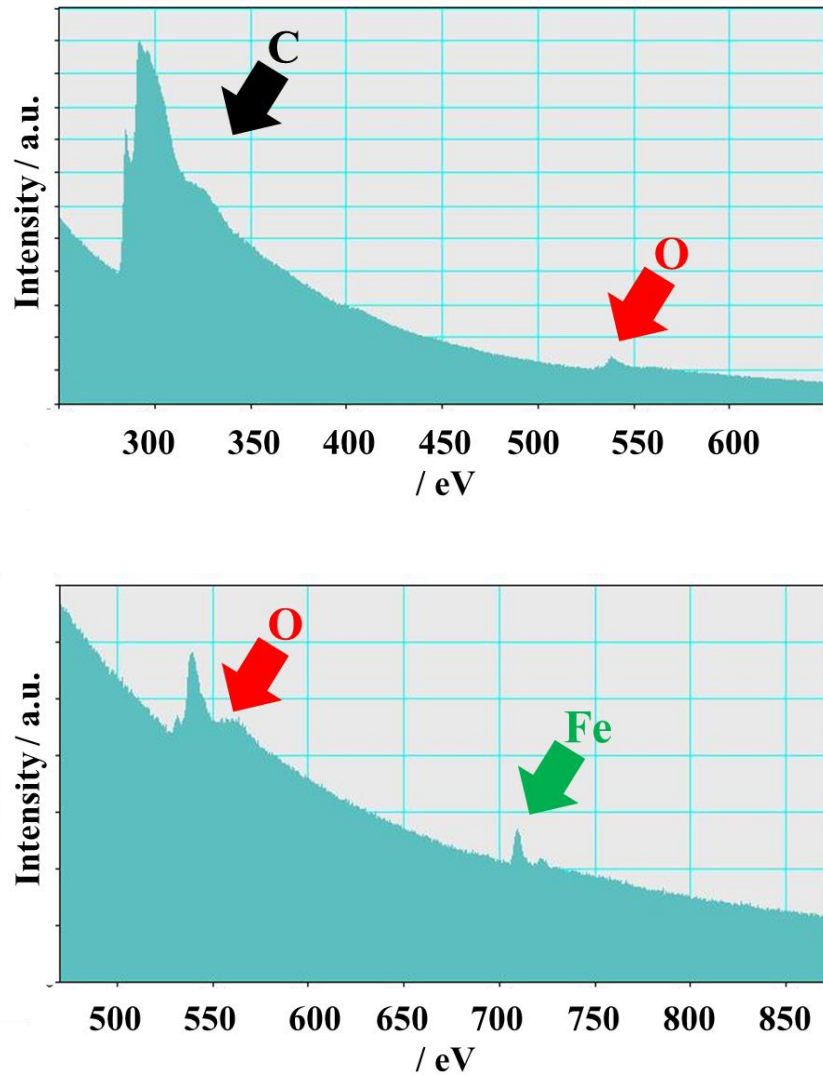
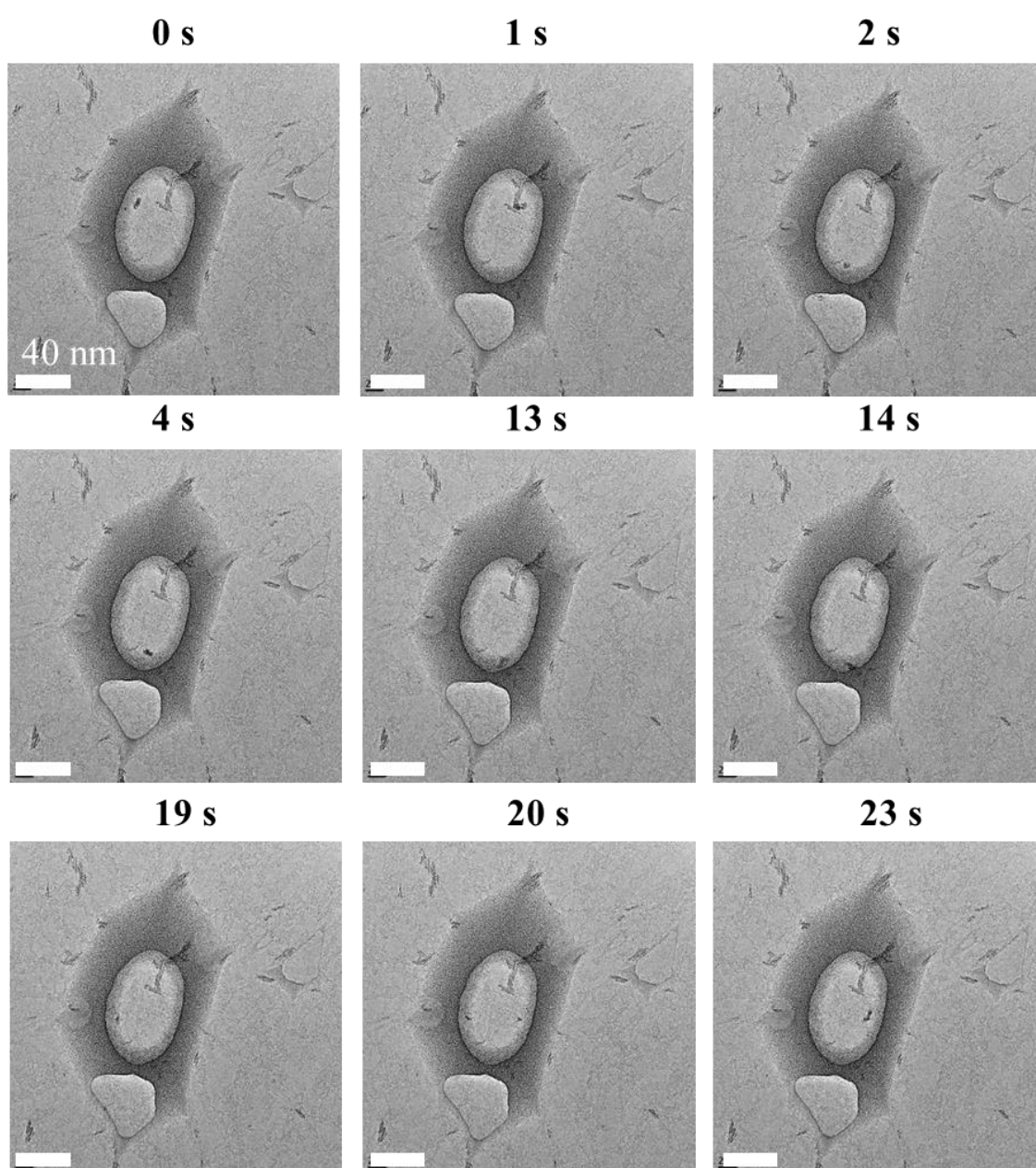


Figure 4-14: EELS spectra of iron nitride aqueous solution.

In Figure 4-13, graphene layers are observed in the background and some liquid pockets are found with amorphous residues, even though the water inside the graphene liquid cell does not evaporate. Compared with ultrapure water, aqueous solutions of iron nitride contain some contamination. We found that many dark spots, which were confirmed to be iron clusters by EELS analysis, exist in the graphene pockets, in

agreement with the TEM images in Figure 4-13. Figure 4-14 shows the EELS spectra of the iron nitride aqueous solution, corresponding to Figure 4-13A. It shows the iron L-edge peaks at approximately 710 eV and 720 eV^[2, 34-35]. We confirmed the sharp oxygen k-edge peaks at 532 eV^[35], which suggests that there are oxygen atoms bonded to iron as hydroxylate. The meaning of hydroxylate in aqueous solution of iron nitride is that water molecules hydrating iron ions exist in the liquid state in this liquid cell.



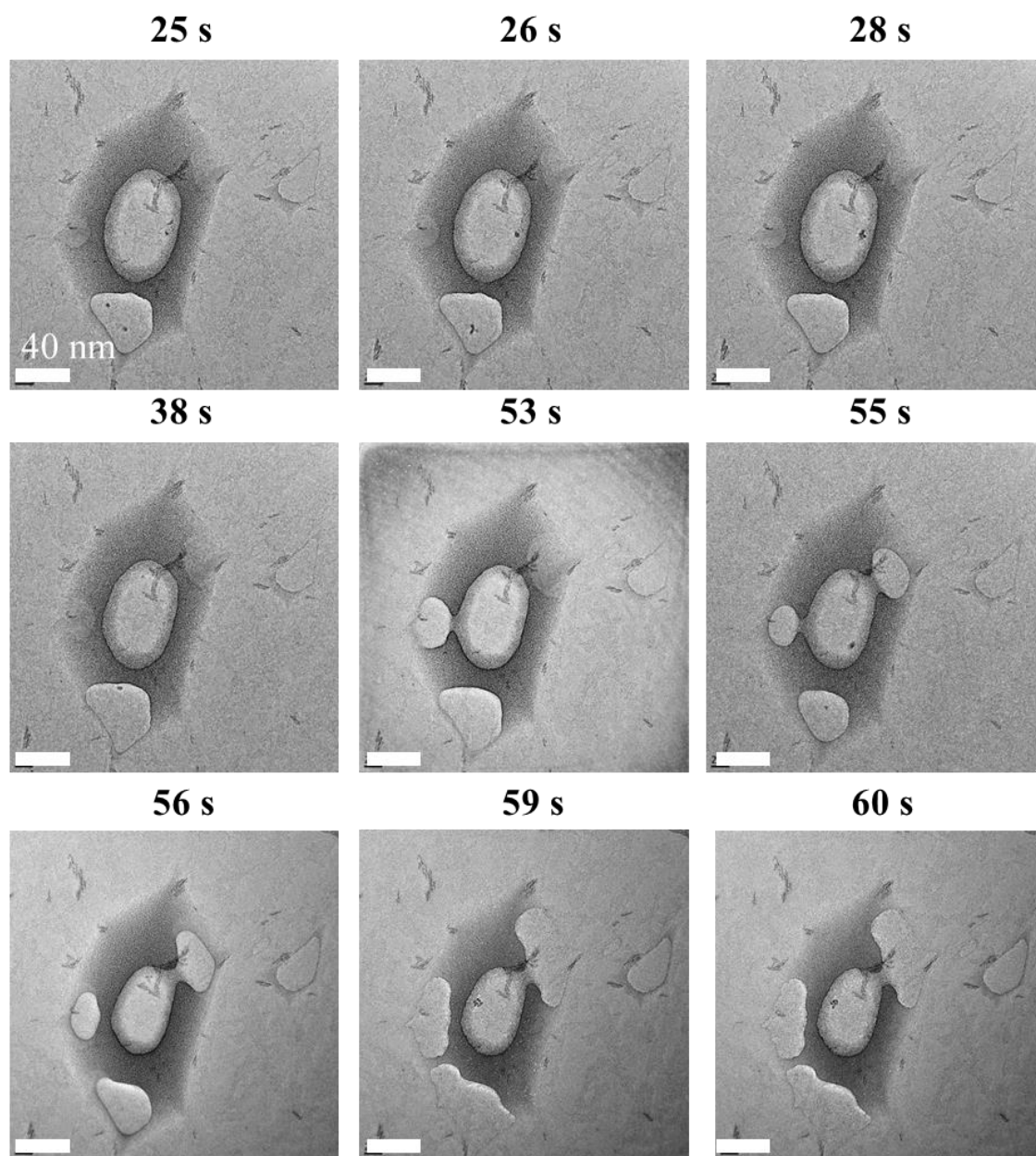


Figure 4-15: Time series of Figure 4-13C.

We observed iron clusters, which were frequently obtained at the edges of bubbles in graphene liquid cells. The clusters undergo repeated formation and dissolution and continue to move until colliding with the graphene liquid cell. The cluster size, as

observed from TEM images, is approximately constant.

We observed that one of the segregated iron nitride clusters that frequently nucleated from liquid water or from the equilibrium reaction of iron nitride rapidly reconstructed. We observed a situation in which clusters repeatedly appeared and disappeared in the graphene liquid cells; however, this interpretation, which is based on TEM observations, is open to argument. The segregation should be observed as a unidirectional reaction, and clusters observed in TEM images should not disappear. Furthermore, we could not obtain TEM images of the equilibrium reaction because such reactions of liquids repeat very rapidly.

Thus, the phenomenon observed in figure 4-15 suggests that iron nitride clusters were formed and reformed because iron nitride aqueous solution was saturated by the decomposition of water. The decomposition of water inside the graphene liquid cell was induced by electron-beam irradiation. In the case of figure (41), we focused the electron beam onto the graphene liquid cell. Decomposition was then induced, resulting in the appearance of some bubbles. Finally, the liquid cell collapsed, resulting in the clusters observed in figure (47). In this supposition, we must estimate the number of molecules of clusters and water. The diameter of five clusters observed in figure (47) was measured to be approximately 5 nm; we therefore inferred that the clusters comprised approximately 1368 molecules. Given that iron nitride can be solved to approximately 2 mol/L at room temperature, 38,035 water molecules must be present in the area in which the cluster moves. The area calculated on the basis of density of water and the number of water molecules is approximately 1676 nm², consistent with average of four layers of water present according to EELS analysis. The area of 1676 nm² is also consistent with the results in figure 4-13. Therefore, the solution inside the graphene

liquid cell is saturated and clusters are precipitated from the solution.

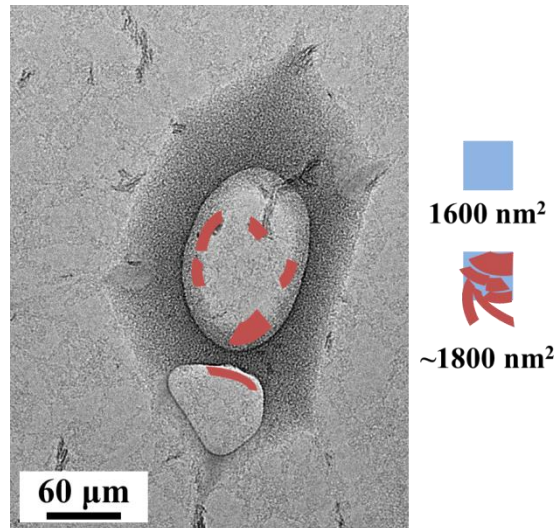
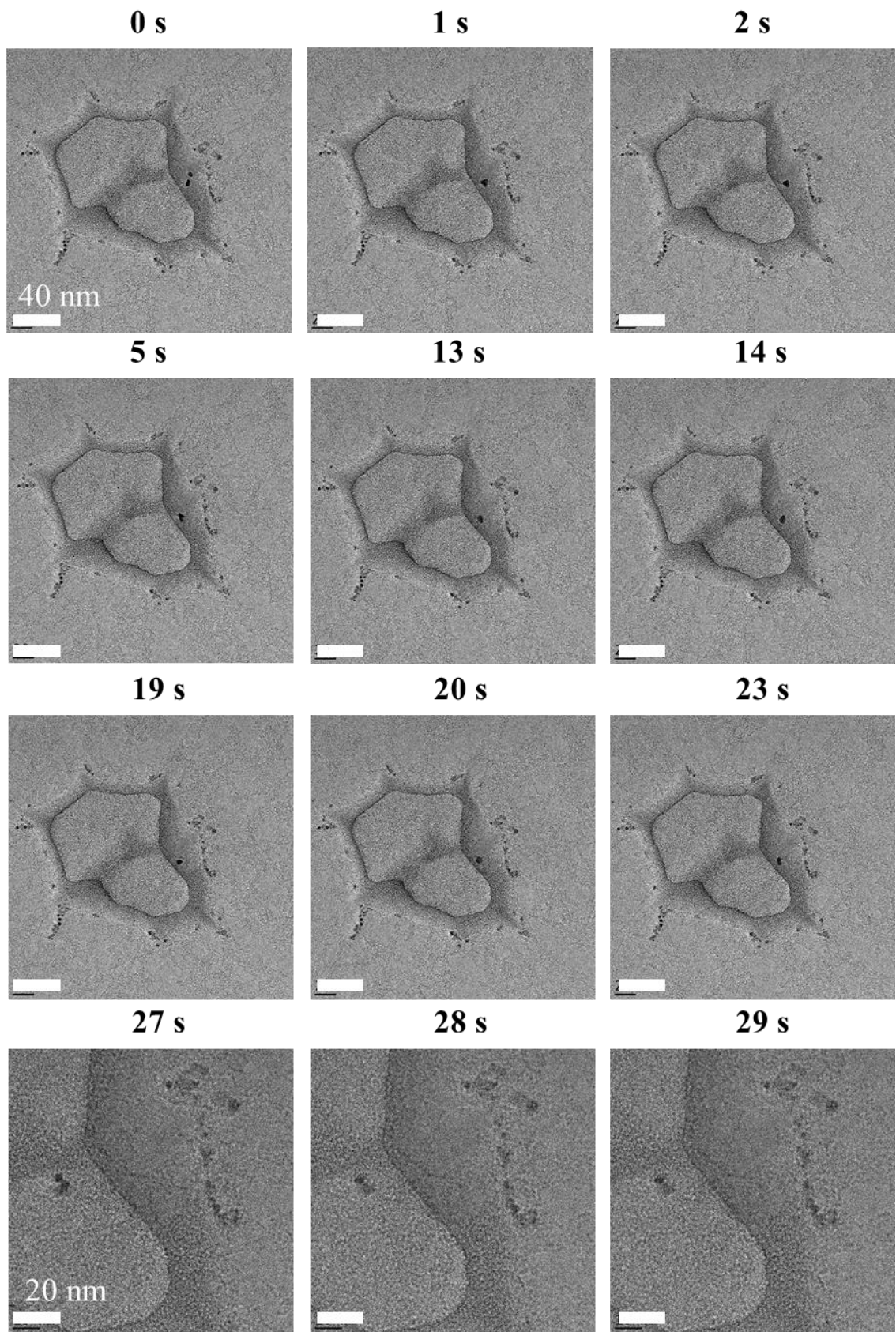


Figure 4-16: The locus image tracking clusters.

A similar phenomenon is observed in figure 4-10D. The time series shown in figure 4-17 indicates a saturated aqueous solution of iron nitride. In figure 4-17, the particle diameter of the iron nitride clusters is approximately 5–8 nm, which is similar to the size observed in figure 4-15. This similarity suggests that 5–8 nm is the critical size for a particle to be precipitated from the saturated solution at room temperature. We propose that the saturated solution bound in a nanosized location may undergo repeated formation and dissolution on this time order.



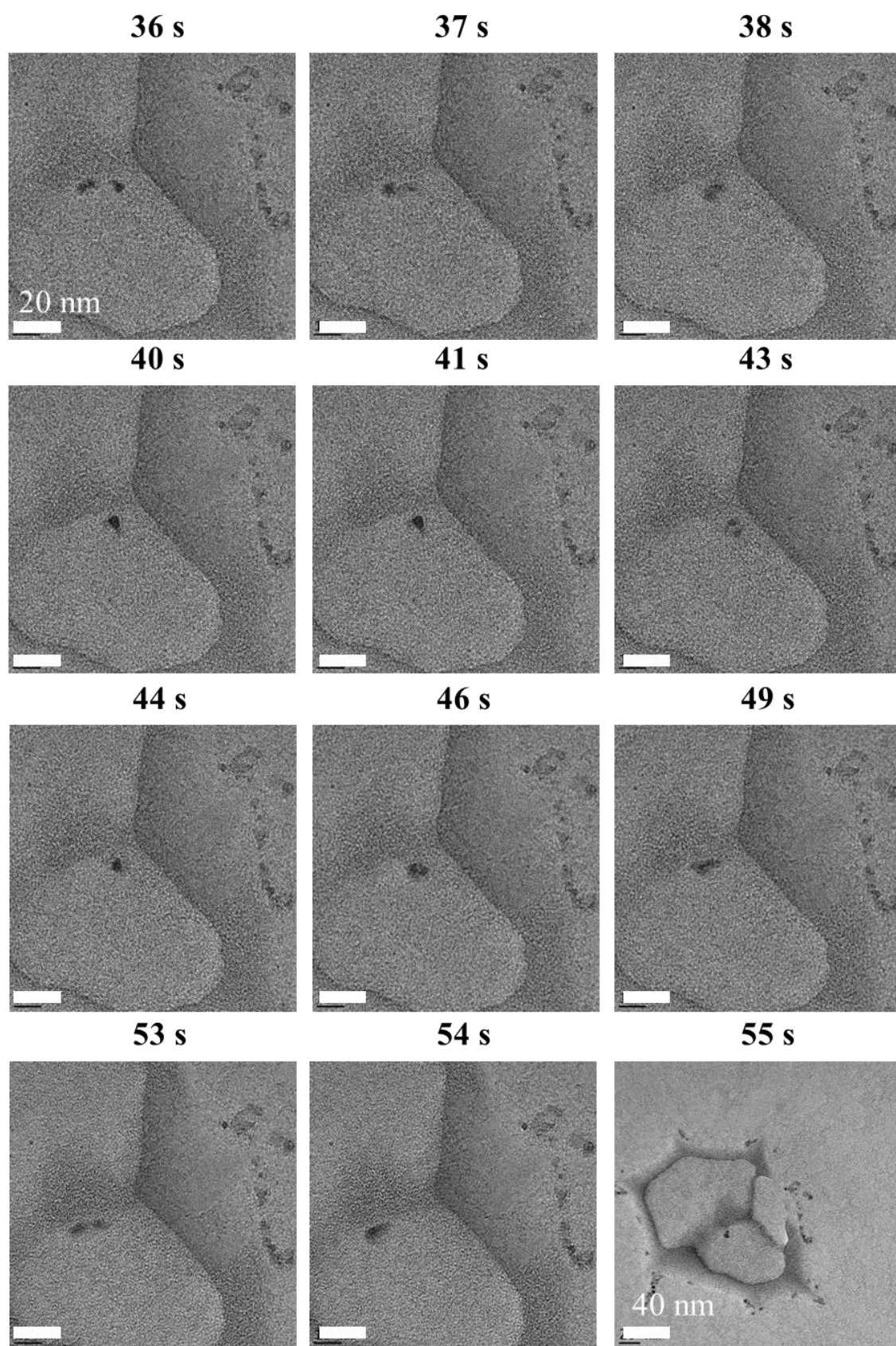


Figure 4-17: Time series of TEM images corresponding to figure 4-13D.

In the following section, we discuss TEM observations of iron nitride aqueous solution at 77 K.

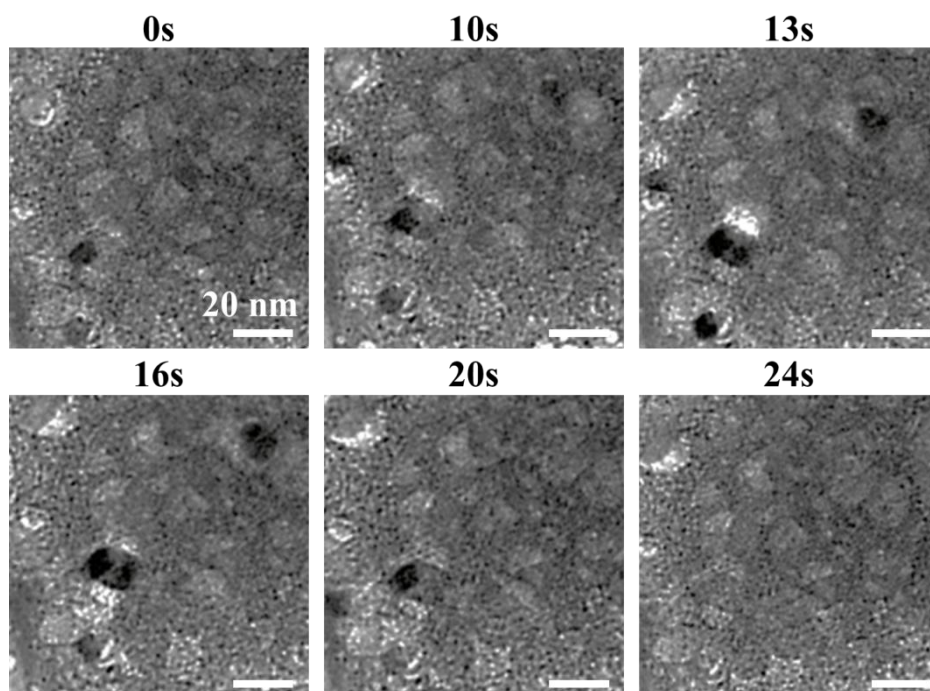
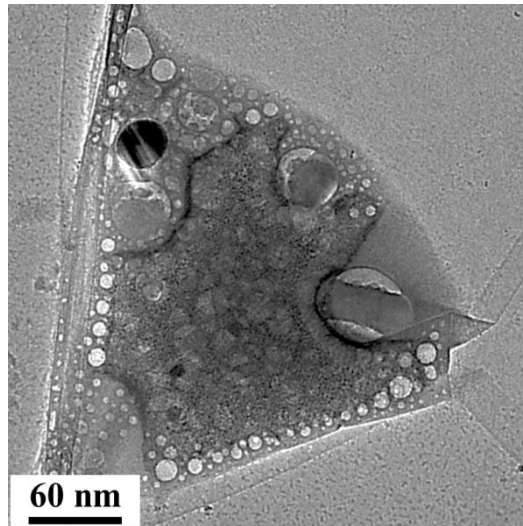
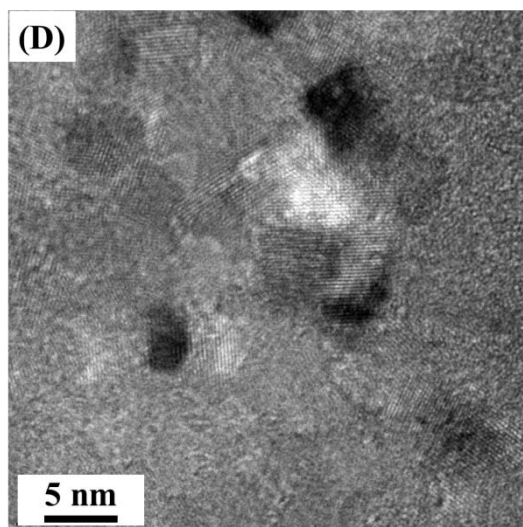
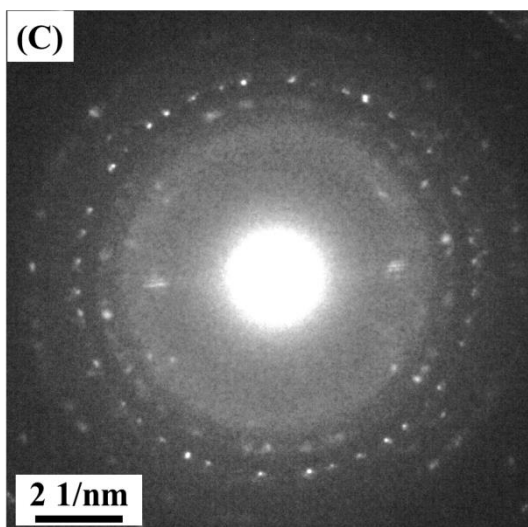
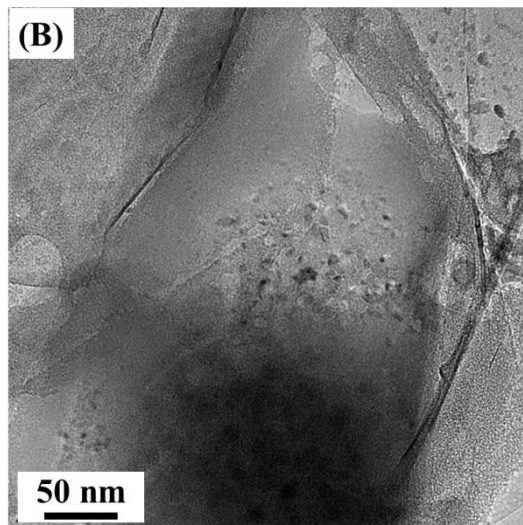
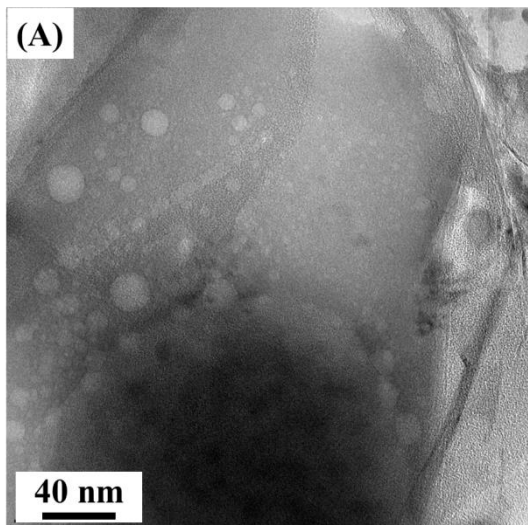


Figure 4-18: Particular TEM images of an iron nitride aqueous solution at 77 K.

Figure 4-18 shows particular TEM images of an iron nitride aqueous solution at 77K. Crystals, which repeatedly form and disappear in the liquid cells, were clearly observed. As a feature of these crystals, their size was determined to be much larger than the cluster size observed at room temperature.

4-5. **Aqueous solution of calcium chloride**

To demonstrate the general versatility of our preparation method, we attempted to sandwich calcium chloride aqueous solution inside a graphene liquid cell. The aqueous calcium chloride solution is observed in the graphene pocket shown in figure 4-19. Figure 4-19(A) shows the effects of evaporation or decomposition by an electron beam at 77 K, and figure 4-19(B) shows numerous crystals. Figures 4-19(C) and (D) show lattice patterns of the graphene liquid cell. Figure 4-19(C) shows the electron diffraction pattern of the crystals in figure 4-19(B), and figure 4-19(D) shows a high-magnification image of the crystals in figure 4-19(B). The electron diffraction pattern shows circular spots of graphene as bright spots located on the middle circle in figure 4-19(C). The graphene pocket consists of a bilayer of graphene, but graphene layer contains wrinkles and bends in the graphene layers, as observed on the right side of figure 4-19(A).



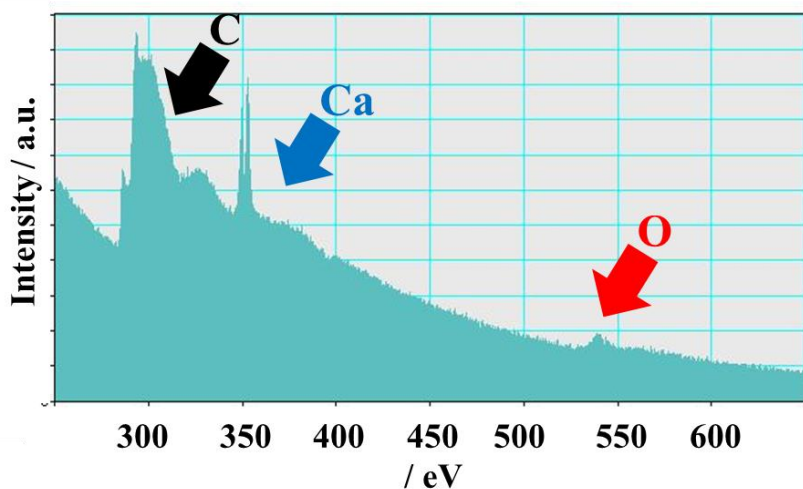


Figure 4-19: TEM images of an aqueous solution of calcium chloride, along with the electron diffraction image and EELS spectrum.

The spots were assigned on the basis of the graphene lattice shown in figures 4-19(C) and (D). According to the electron diffraction image, we observed spots consistent with the (210), (111), and (002) surfaces of a crystal of calcium chloride hexahydrate; the corresponding d -values are 0.25, 0.28, and 0.19 nm, respectively. The EELS spectrum exhibits carbon (284 eV) and oxygen (540 eV) K-edge and calcium L-edge (350 eV) peaks^[36-37]. Two sharp peaks were observed as calcium peaks, and a broad peak (200 eV) was also observed as chlorine K-edge peak.

Figure 4-20 shows a comparison of the crystal structure and a TEM image of calcium chloride hexahydrate. Each angle formed by red lines is 120° , and the length of both red lines represents 0.25 nm. In this observation, we propose that calcium chloride hexahydrate crystals were formed as liquid was evaporated by the electron beam. Therefore, we obtained information about the environment inside the graphene liquid

cell given that the melting point of calcium chloride hexahydrate is known to be 303 K at atmospheric pressure. In addition, a saturated aqueous solution of calcium chloride should form calcium chloride hexahydrate crystals at 218–302 K^[37]. At temperatures above 302 K, calcium chloride dihydrate and tetrahydrate crystals should form. According to these results, water is clearly decomposed via radiolysis by electron-beam irradiation without undergoing a temperature increase. This result is consistent with the fact that water and graphene are known to be good thermal conductors.

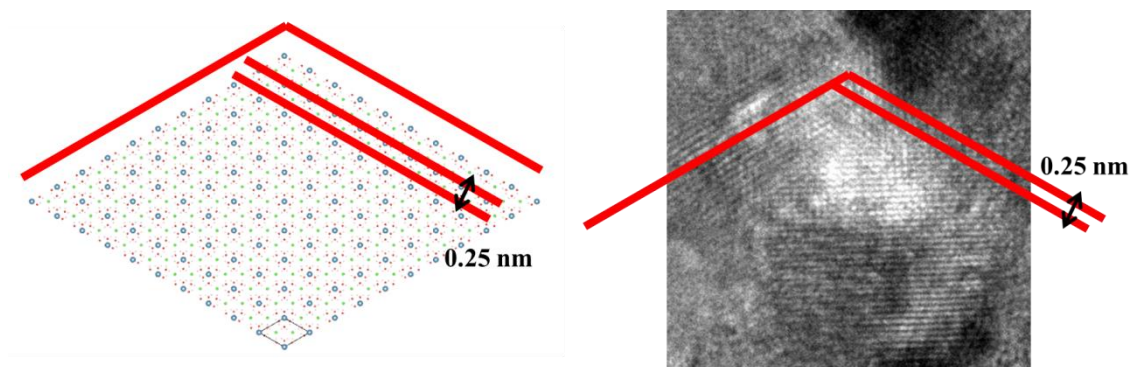


Figure 4-20: Structure image (left) and TEM image (right) of calcium chloride hexahydrate.

4-6. Organic solvents

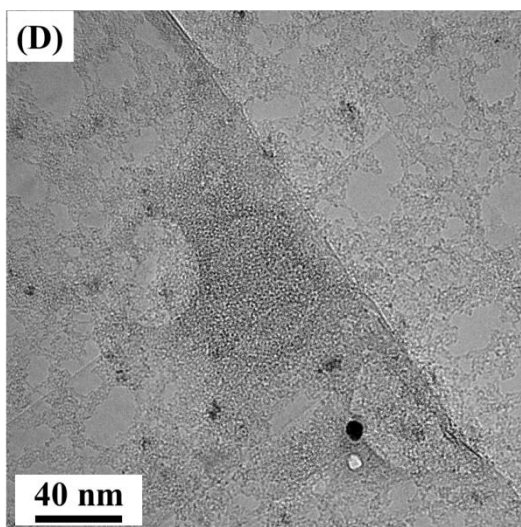
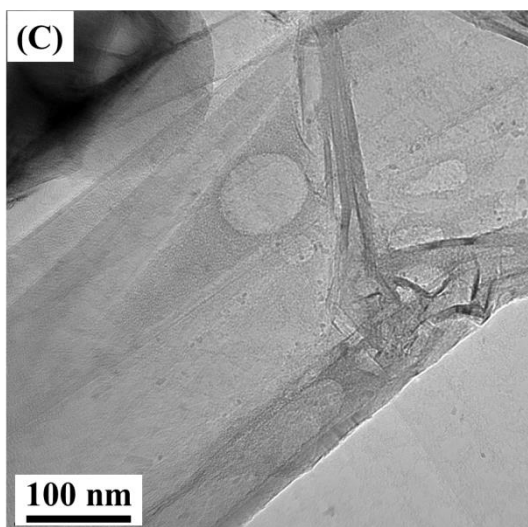
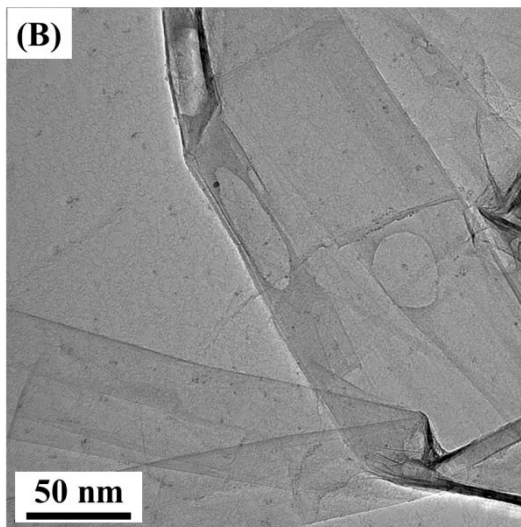
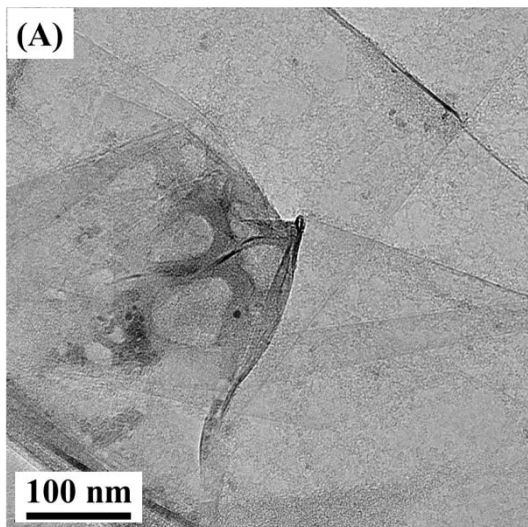
We demonstrate our graphene liquid cell preparation technique utilizing several different organic solvents. However, spray mists of organic solvents is sometimes difficult because many organic solvents are easily vaporized and graphene ruptures when exposed to hydrophobic organic solvents. Therefore, we prepared organic solvent sandwich structures via the capillarity effect. An SiN TEM grid with graphene was prepared using the same process, where the TEM grid was soaked in the organic solvent

under investigation. Another approach to encapsulate organic solvents inside graphene layers is to place a water and organic solvent mixture mist on graphene instead of an aqueous solution mist. In this section, we present TEM images and elemental analysis results for sandwiched graphene liquid cells encapsulating trichloromethane (99.0%, Wako), methanol (99.8%, Wako), and 2-propyl alcohol (99.7%, Wako) as representative organic solvents. These organic solvents are commonly used in various research applications.

4-6-1. Trichloromethane

Trichloromethane, also known as chloroform, is an organic compound with the formula CHCl_3 . Trichloromethane is known to penetrate deep into the gap between graphene and a substrate through wrinkles and bends in the graphene when a polymer such as polycarbonate is removed. Figure 4-21 shows TEM images of trichloromethane encapsulated inside a graphene liquid cell.

We observed several pockets at wrinkles and bends in the graphene layers. The normal liquid cells, which exist at the center of bilayer graphene, were not observed, in contrast to the spray preparation method.



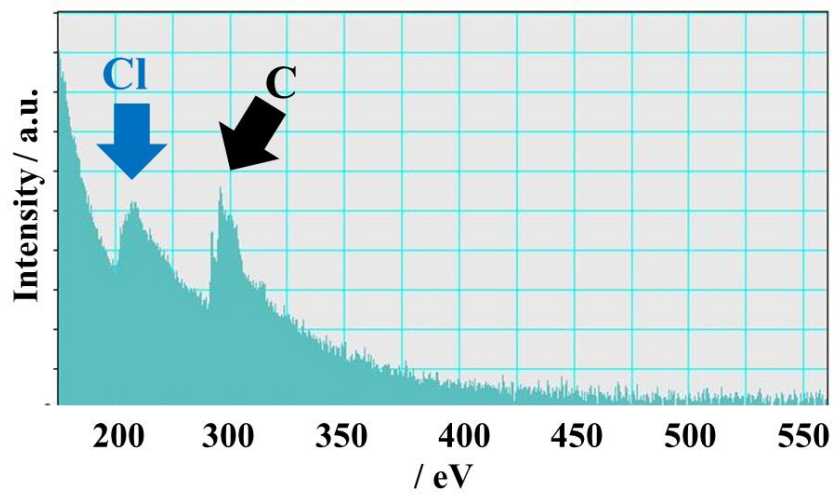
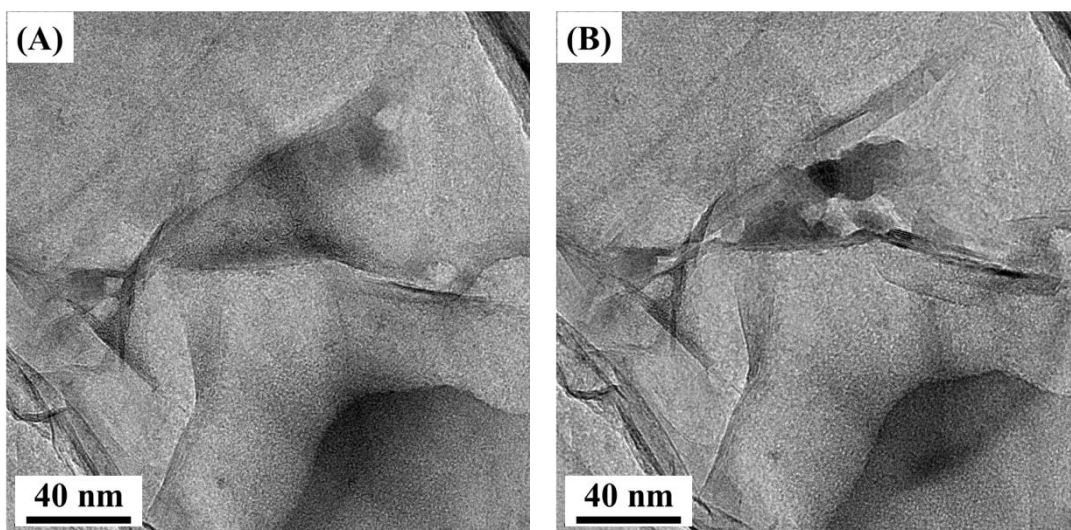


Figure 4-21: Typical TEM images of trichloromethane encapsulated inside a graphene liquid cell, and the EELS spectrum of a droplet of trichloromethane.



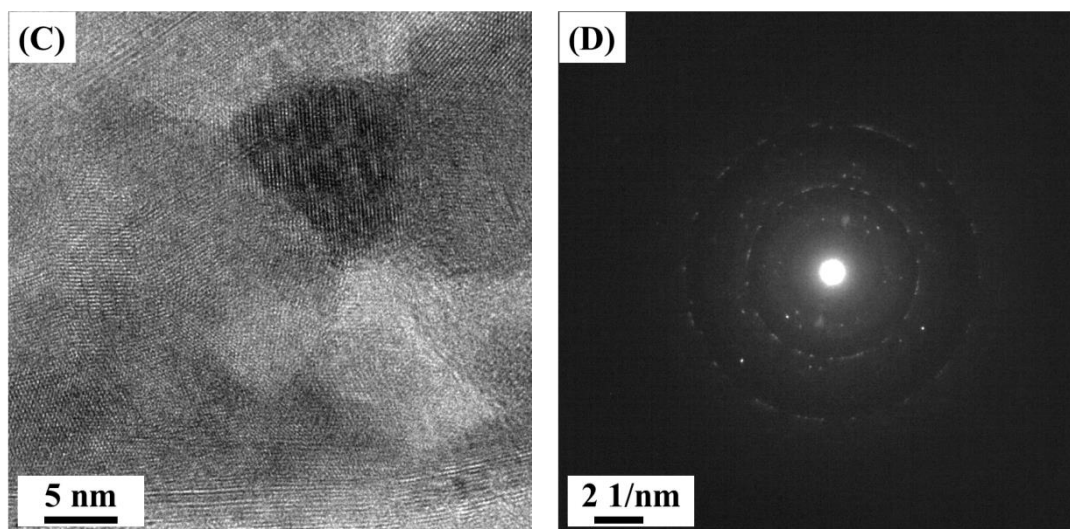


Figure 4-22: TEM images of trichloromethane encapsulated inside a graphene liquid cell, and the corresponding electron diffraction image.

Figure 4-22 shows other TEM images of trichloromethane encapsulated inside a graphene liquid cell. We confirmed that trichloromethane formed crystals under electron-beam irradiation. Before focusing the electron beam on the center of the pocket, we observed some bubbles from the trichloromethane, as shown in figure 4-22(B). These bubbles disappeared immediately, although bending of the graphene and crystallization occurred with the disappearance of the bubbles. Figure 4-22(C) and (D) show high-magnification images of crystals and their electron-diffraction pattern. The lattice patterns in images (C) and (D) indicate that these crystals are trichloromethane. This crystallization is consistent with previous research indicating that the phase transition of trichloromethane at room temperature occurs at approximately 600–790 MPa^[38-39]. We confirmed experimentally that the pressure in the graphene liquid cell is approximately 600–700 MPa, thereby demonstrating the correctness of the assumption

stated in section 4-2. However, the presence of some contaminants were observed in the electron diffraction pattern. In figure 4-22(D), graphene bends are observed as the circular pattern and additional unidentified bright spots are also observed. These contaminants result from the concentration of residues from the sample liquid, such as trichloromethane; impurities at concentrations of approximately 1% cannot be observed by TEM.

4-6-2. Methanol

Methanol is an inexpensive and readily available alcohol with formula CH_3OH . Figure 4-23 shows typical TEM images of methanol encapsulated inside graphene liquid cells. In this sample preparation, we sprayed a methanol and water solution with a ratio of 2:1. Numerous liquid cells are observed in figure 4-23(A); however, the EELS spectrum in figure 4-24(A) indicates that methanol is not present. Figure 4-23(B) also shows liquid cells and the presence of silicon oxide, but methanol is again not detected. By contrast, methanol was detected in the EELS spectrum in figure 4-24(B) of the liquid cell in figure 4-23(C).

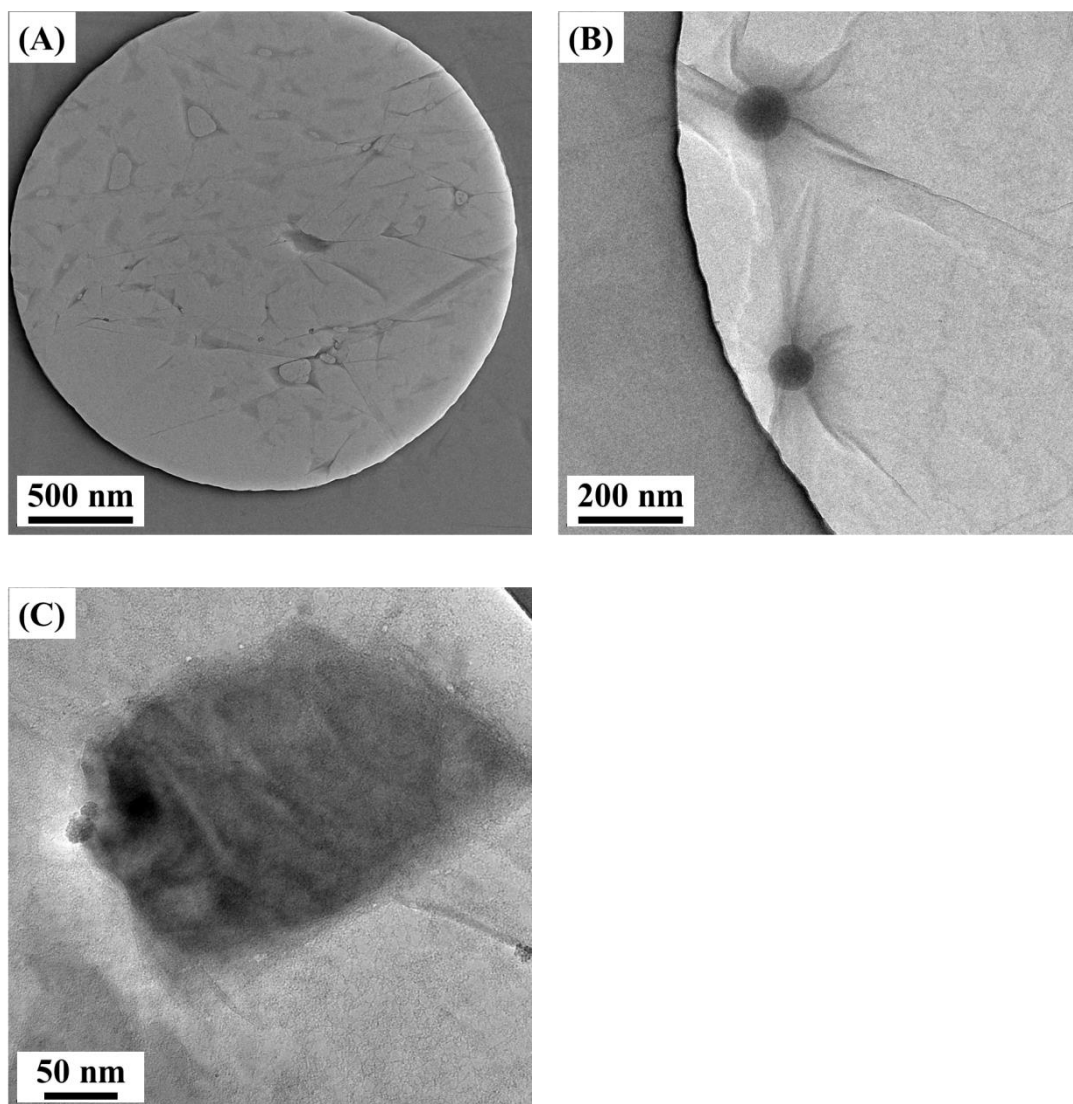


Figure 4-23: Typical TEM images of methanol encapsulated inside graphene liquid cells.

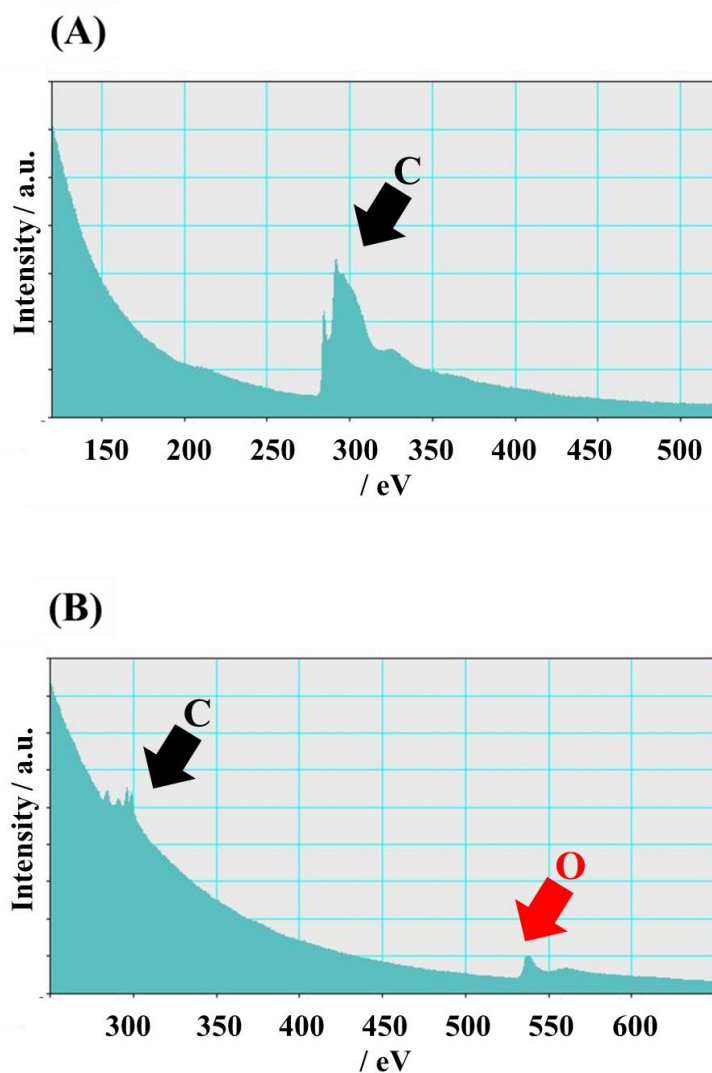


Figure 4-24: EELS spectra of the graphene liquid cells shown in figures 4-23(A) and (C).

Characteristic carbon K-edge peaks^[40], whose peak shape differs substantially from that of graphene or graphene liquid cells, are observed in figure 4-24(B); these peaks are attributed to methanol. The sample sandwiched with the methanol and water mixture solution is also observed to have crystallized, as shown in figure 4-25. However, the crystals observed in this sample contained concentrated contaminants and residues.

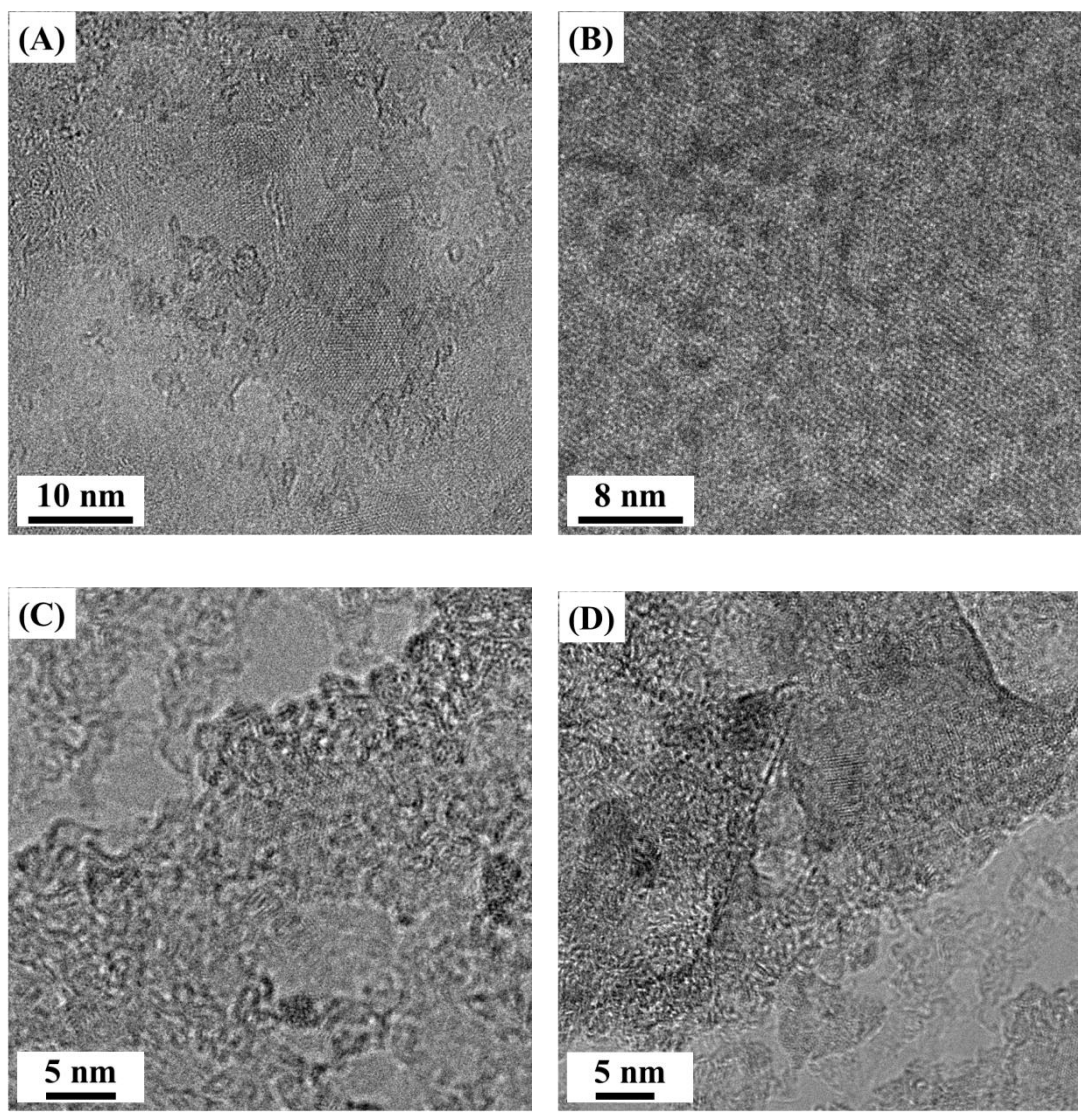


Figure 4-25: TEM images of crystals observed inside graphene liquid cells sandwiched with a methanol and water mixture solution.

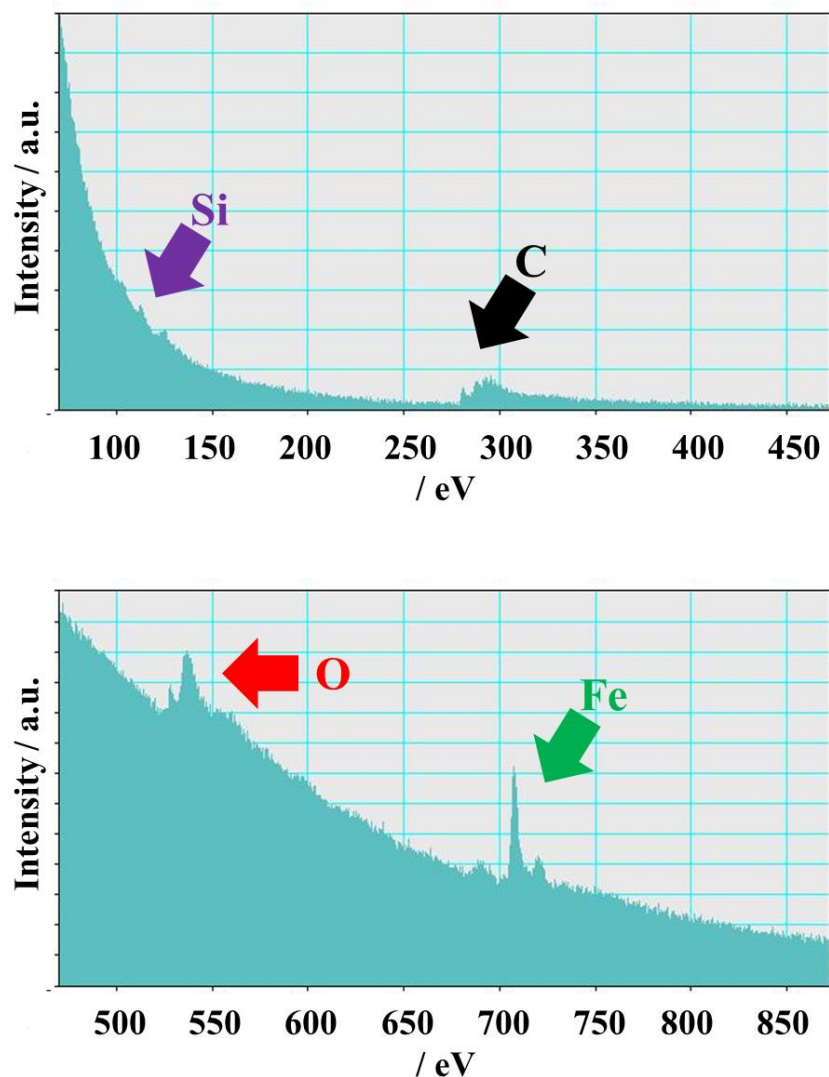


Figure 4-26: EELS spectra corresponding to the graphene liquid cells in figure 4-25(A).

According to the structure information in figure 4-25(A) and the elemental analysis results in figure 4-26, the crystals observed in figure 4-25(A) are composed of $\text{Fe}(\text{OH})_2$ and silicon oxide. By contrast, the crystals observed inside the graphene liquid cells sandwiched with the methanol and water mixture solution are difficult to identify because the composition of crystals with various lattice structures and elemental compositions cannot be determined.

4-6-3. 2-Propyl alcohol

2-Propyl alcohol is also known as isopropanol (IPA) with formula $\text{CH}_3\text{CHOHCH}_3$. Figure 4-27 shows typical TEM images of IPA encapsulated inside graphene liquid cells. In this sample preparation, we sprayed an IPA and water solution with a 2:1 ratio, similar to the method used for the methanol and water solution.

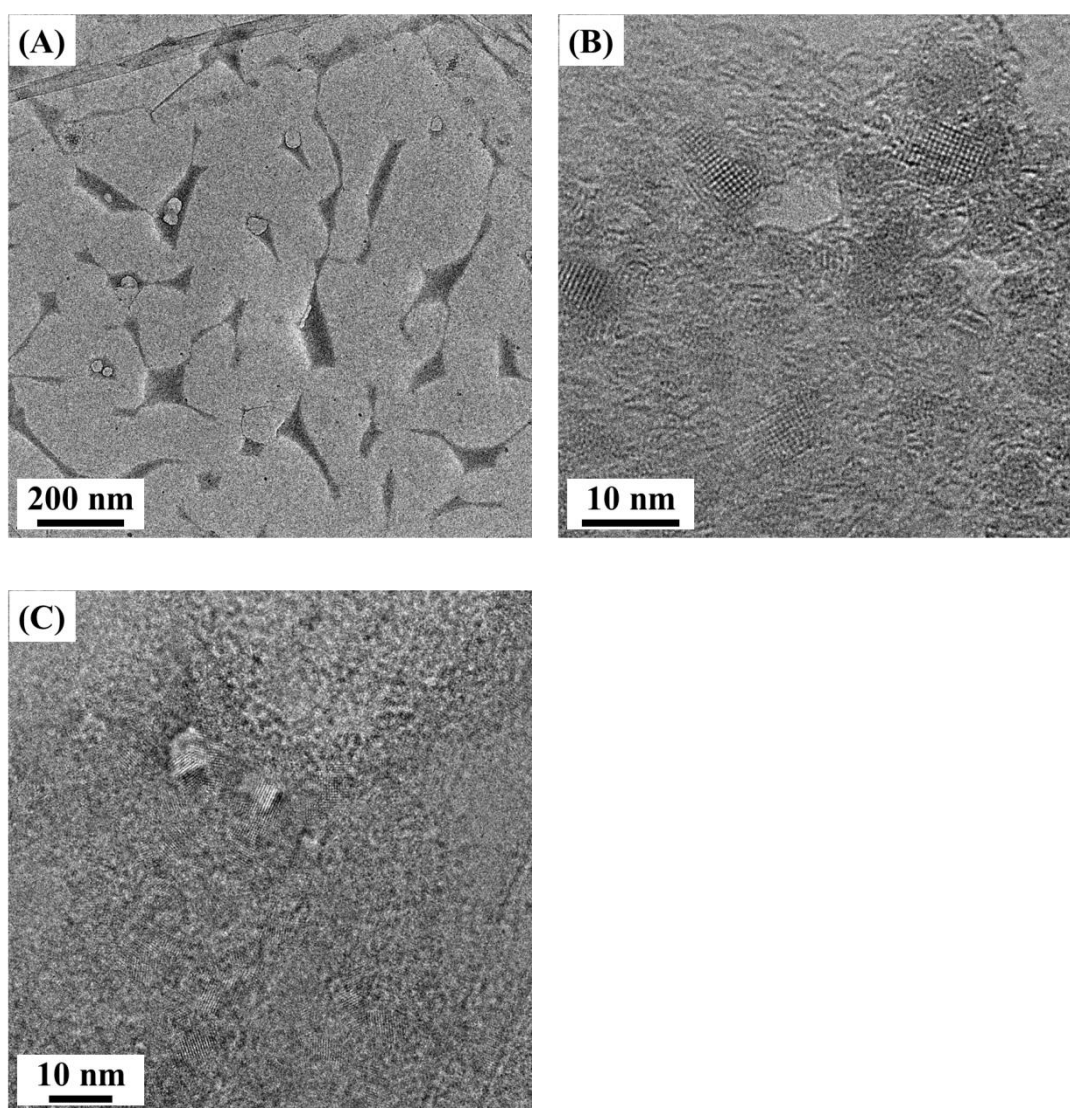


Figure 4-27: Typical TEM images of IPA encapsulated inside graphene liquid cells.

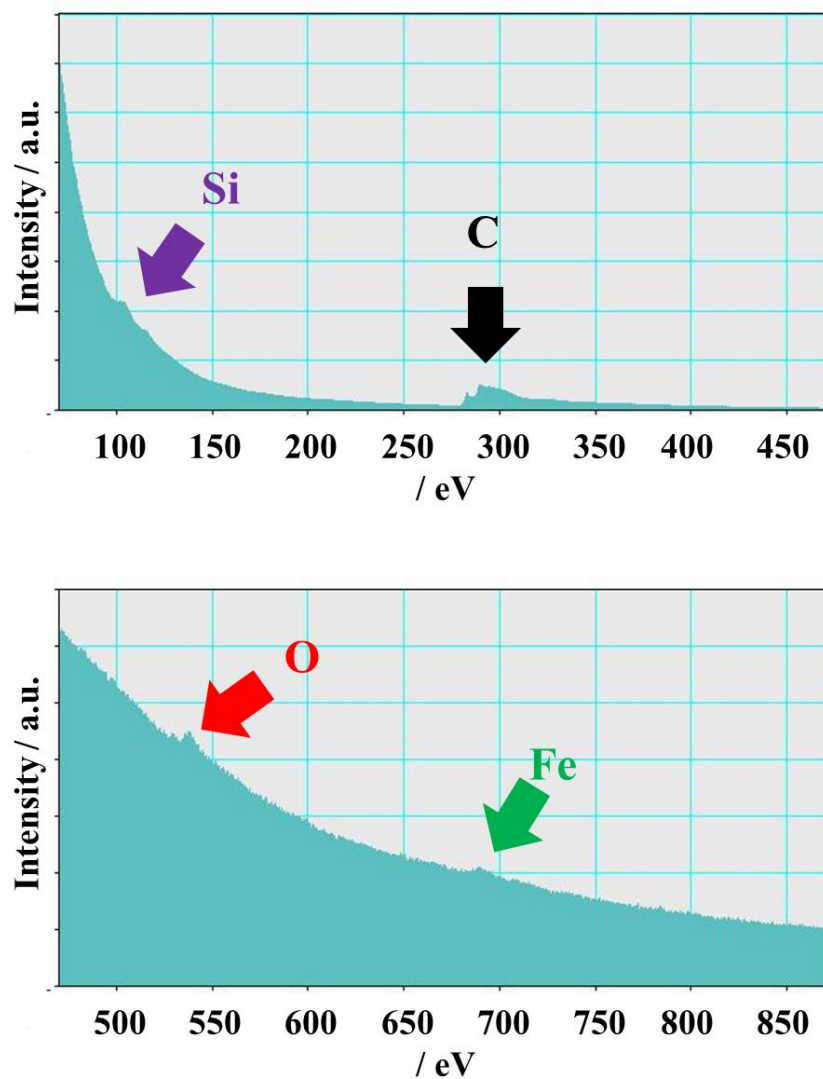
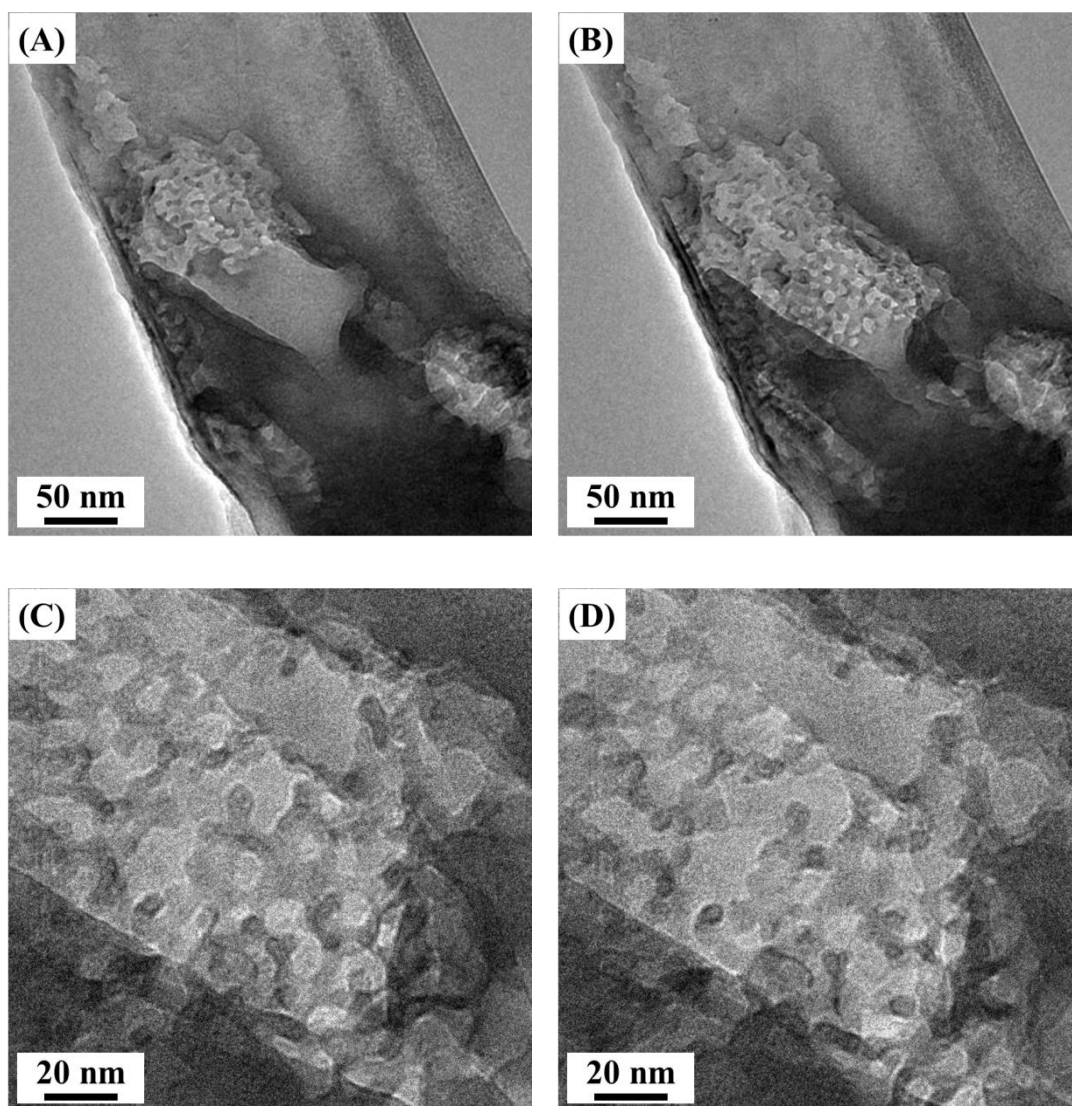


Figure 4-28: EELS spectra corresponding to the TEM images in figure 4-27

Many liquid cells are observed in figure 4-27(A); however, the EELS spectrum shown in figure 4-28 did not indicate the presence of IPA. The same trend was observed in the case of the methanol and water mixture solvent. The crystals observed in figures (B) and (C) do not exhibit a specific composition. Metals or solvents may be present as

contaminants in the IPA because its purity, 99.7%, although their concentrations are not sufficient for them to be observed by TEM.

Figure 4-29 shows a time series of TEM images of IPA encapsulated inside graphene liquid cells. Interestingly, we observed that crystals moved or decomposed under electron-beam irradiation.



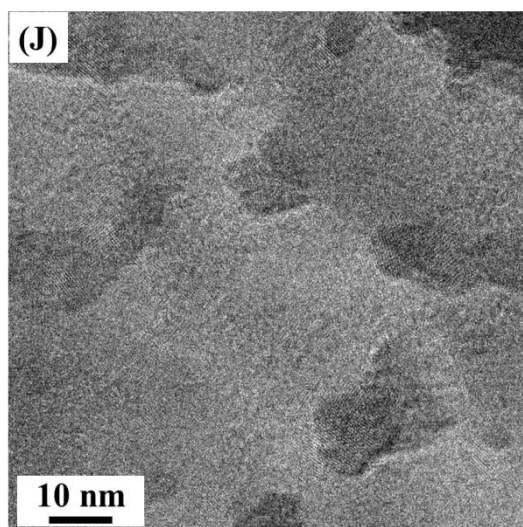
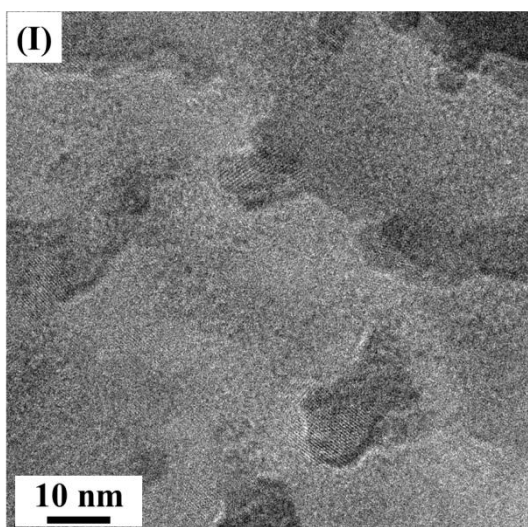
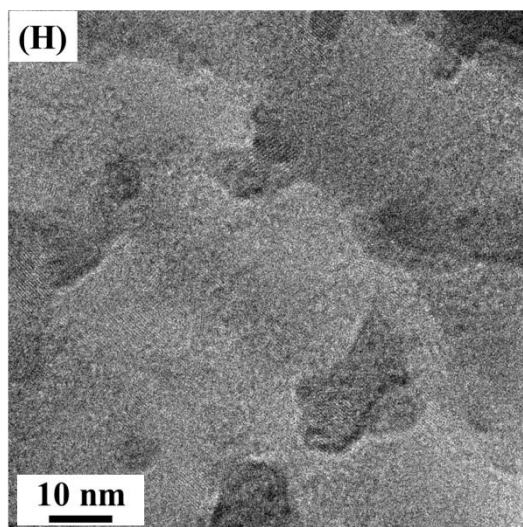
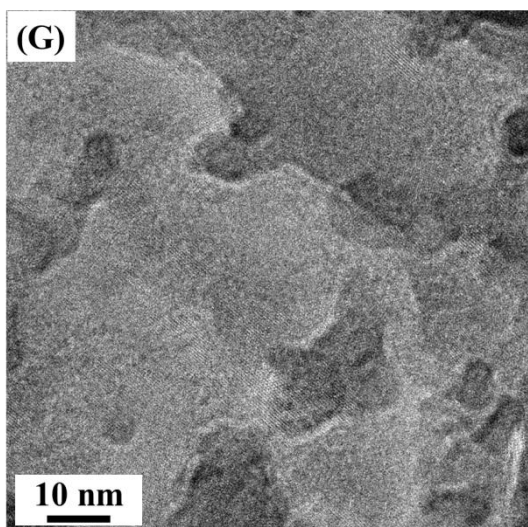
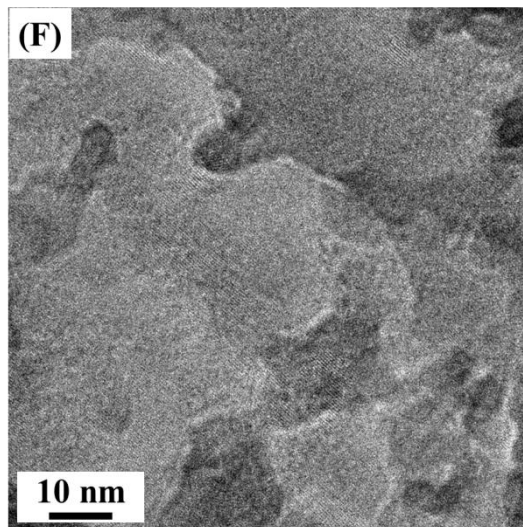
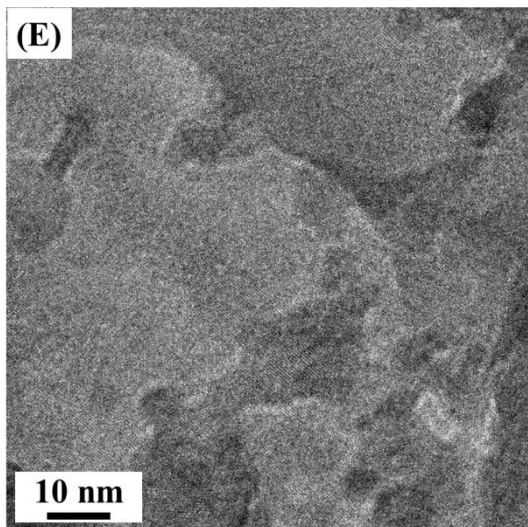


Figure 4-29: Time series of TEM images of IPA encapsulated inside graphene liquid cells.

A clear lattice is evident in figure 4-29; its EELS spectrum, which is shown in figure 4-30, supports the presence of IPA, which shows a particular carbon K-edge. High-magnification TEM images show that crystals were present in almost all of the pocket, as indicated by the crystals in the low-contrast areas in figures 4-29(I) and (J). We presume that this phenomenon indicates the presence of the mixed structure of water and IPA. However, the complex structure of water and alcohol molecules is difficult to observe; furthermore, we cannot determine crystal structure of this crystal in detail.

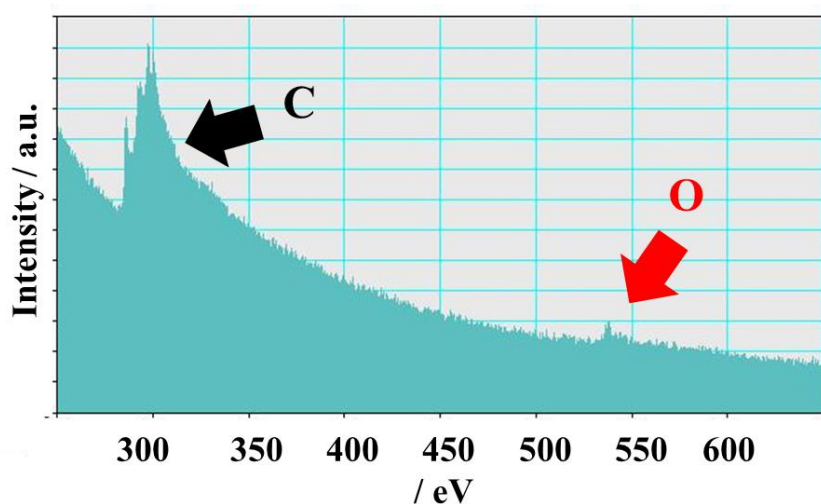


Figure 4-30: EELS spectrum corresponding to figure 4-29.

In summary, we confirmed that various solutions were encapsulated inside graphene liquid cells and we successfully obtained numerous TEM images of liquid and

elemental analysis results confirming the presence of the solutions inside the cells. However, the complex structure of the mixture solutions could not be characterized in detail. Furthermore, we observed some contaminants inside the liquid samples before they were encapsulated inside the graphene liquid cell.

4-7. Phase transitions of liquids

We often observe various crystals in the process of TEM observation of graphene liquid cells. In particular, observed crystals formed from liquids were identified as hexagonal ice. Figure 4-31 shows TEM images of a phase transition. Graphene layers are present in the background and non-structural region of pure water is observed in the center of Figure 4-31(A). Some gold clusters are observed, which we added to pure water for observation of Brownian motion. However, after focusing the electron beam, we obtained a clear lattice image, as shown in Figure 4-31(B).

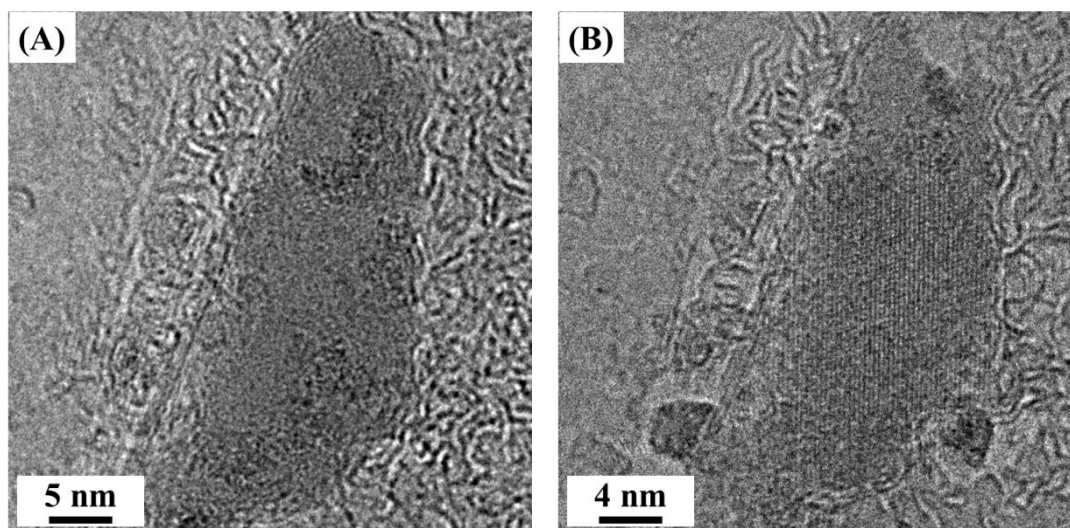


Figure 4-31: TEM images of a phase transition.

Gold clusters are observed at the side of the ice lattice, and remaining liquid water is observed on the upper side of the ice. The electron diffraction image in Figure 4-32 shows the [2-21] incident plane of hexagonal ice, which is denoted with red circles. The lattice spacings of these spots are 0.268 nm and 0.167 nm, and we identified them as the (012) and (-114) surfaces, respectively.

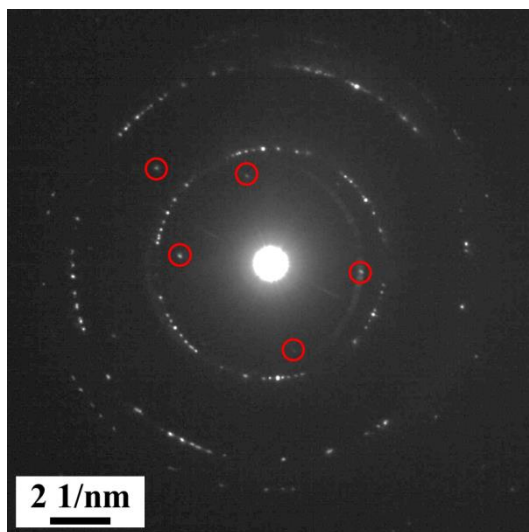


Figure 4-32: Electron diffraction image corresponding to Figure 4-31(B).

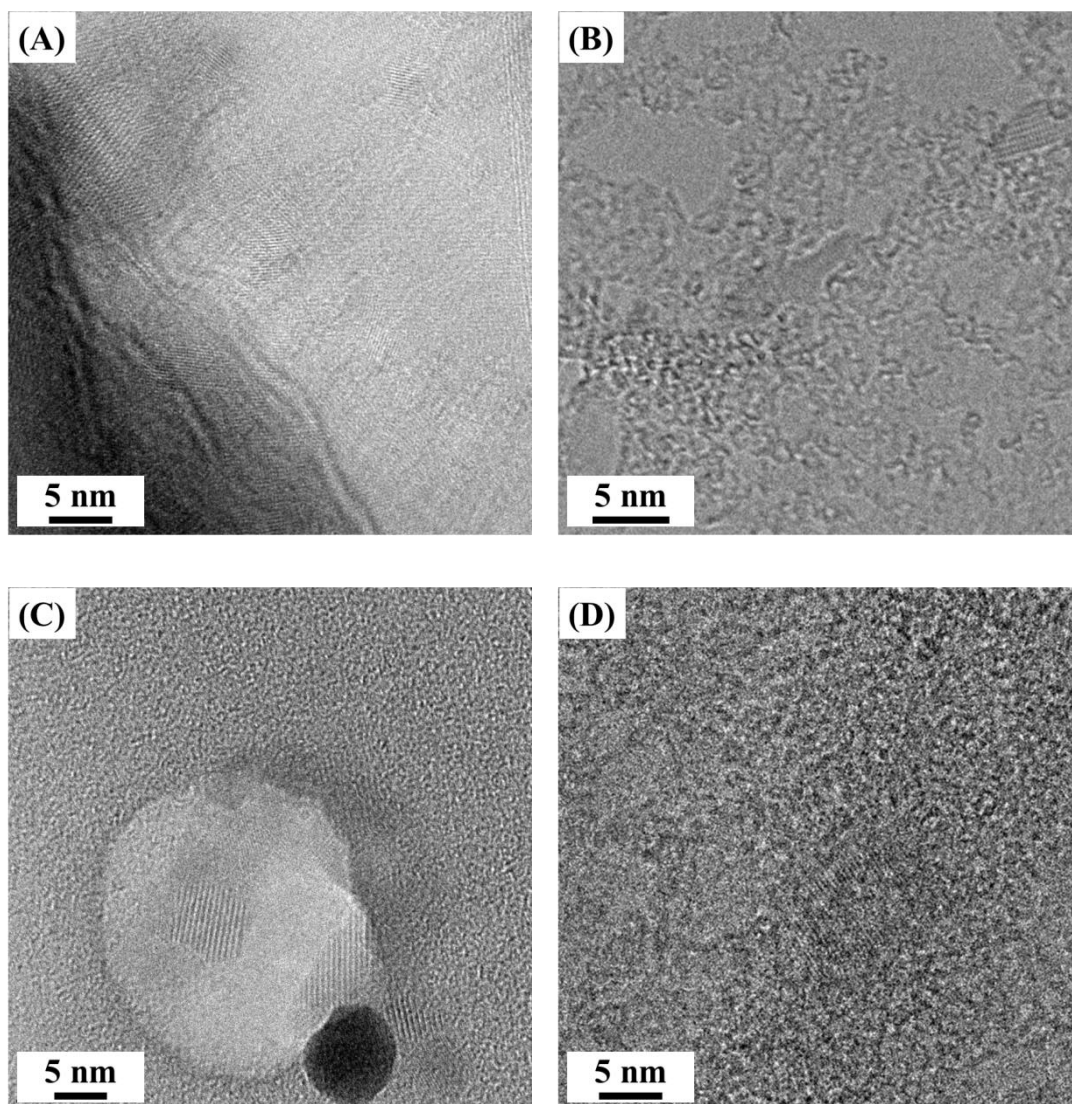
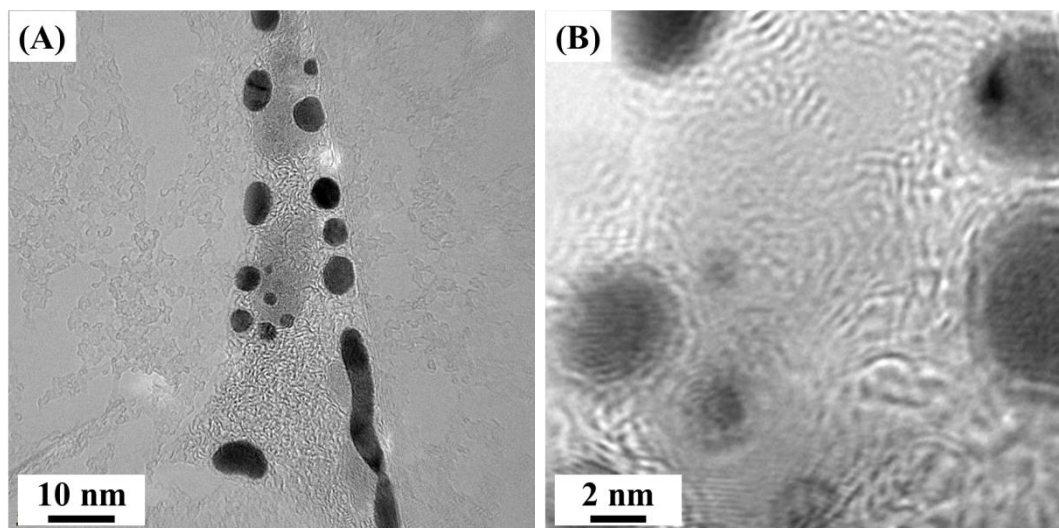


Figure 4-33: Typical TEM images of ice.

We often observed hexagonal ice, as shown in Figure 4-33; however, we could not definitively determine the presence of hexagonal ice. Hexagonal ice is known to form at 273 K under atmospheric pressure, and its melting point is known to decrease with increasing pressure. Our observations at room temperature under high pressure are inconsistent with this common knowledge. In our observations, water droplets and some

contaminants were present when we observed the formation of ice. Therefore, we considered that impurities served as nucleation sites for ice. Furthermore, hexagonal ice can apparently only nucleate on a pure metal because ice was not obtained in aqueous solutions of salt. Accordingly, we attempted to sandwich ultrapure water containing gold particles in liquid graphene cells and observe the formation of hexagonal ice.

A typical TEM image of the graphene cell sandwiching gold and water is shown in the Figure 4-34(A). At a low magnification, gold clusters are observed with a strong contrast, and droplets are surrounded by the clusters. Water quickly generates air bubbles under electron beams, and is observed with contrast lower than the gold. At the time when this image was taken, the droplets did not have a clear lattice structure or amorphous structure but simply appear with a light contrast, as same as in the observation of the ultrapure water.



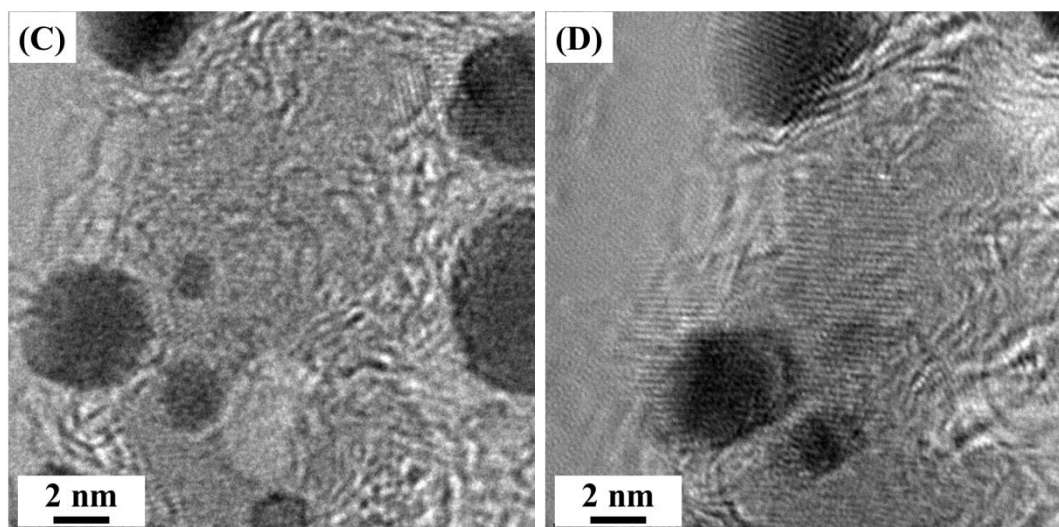


Figure 4-34 : Time series of room temperature TEM image of water droplets with gold particles encapsulated inside graphene sandwich region.

In Figure 4-34, these are the images that were observed respectively after 10, 321, 412, and 840 seconds since we start to observe. Typical low magnification image of water droplets with gold particles is shown in Figure 4-34(A). Black particles show gold and dark contrast regions show water droplets. Graphene layers are in background and they have some amorphous carbon network as can be seen on the both side area in this image. Figure 4-34(B) shows high magnification image with electron beam focusing to the droplet located on the center of Figure 4-34(A). In Figure 4-34(C), we found that the bubble, which is low contrast area in the droplet, appears because of vaporization of water induced by electron beam irradiation. Then the droplet was immediately crystallized for hexagonal ice as shown in Figure 4-34 (D). In Figure 4-34 (D), we can see clear lattice of ice and Moiré structure of graphene layers.

In Figure 4-34, we show the temporal change of the droplets after electron beams are

focused them. The droplets actively generated bubbles just after the electron beams have been focused, showing vaporization of water due to the electron beam induced radiolysis. However, the boiling rapidly decreased at Figure 4-34(D), and the droplet contrast, which had been ambiguous, became clearer. The structure of the droplet shows lattice pattern that is different from the spacing of lattice plane of gold cluster.

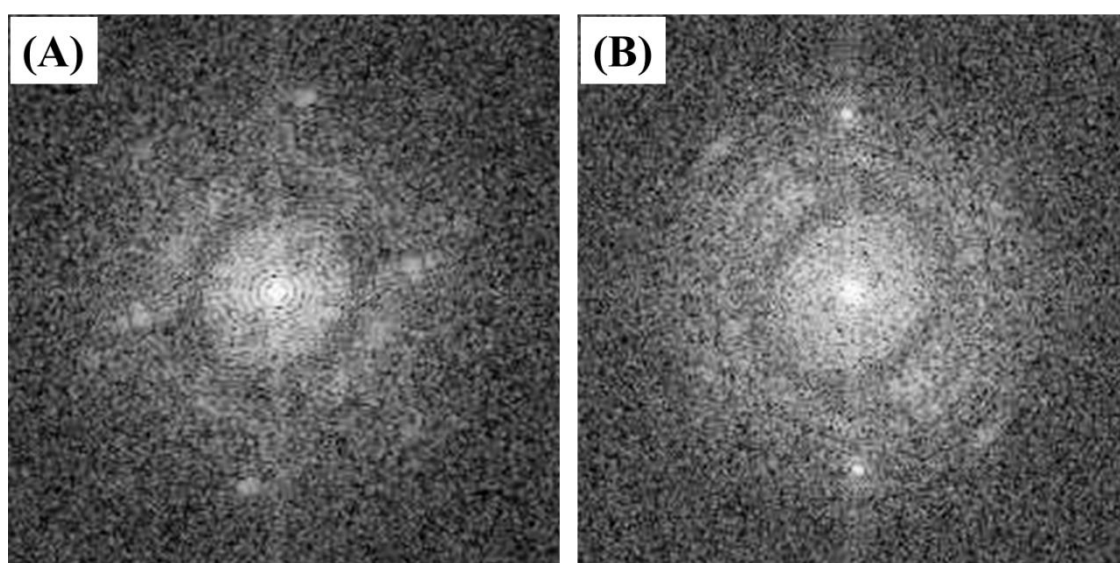


Figure 4-35 : FT images corresponding to Figure 4-34(C) and (D), respectively.

FT image of gold cluster and this droplet are shown in Figure 4-35(A) and 4-35(B). Both figures slightly reveal the hexagonal structures of graphene. Spacing of lattice planes calculated based on the graphene lattice was 0.213 nm, are matching that of polycrystalline gold (111) and hexagonal ice (01-2) and (110) regarding with fig.3(A) and 3(B). We confirm that Figure 4-35(B) is consistent with $[-221]$ incident of hexagonal ice 1h.

We discuss the reason that the water with gold turns into ice. Considerable factors of

formation ice are effect of graphene's hydrophobicity and impurity effect by gold atoms. We hypothesized that the water molecules make strong hydrogen bonds due to graphene's hydrophobicity and that they are also oriented such that their polar groups are is not directed to graphene. It has been confirmed that water could transform into ice even at room temperature under atmospheric pressure if a high voltage is applied. The driving force of this phenomenon was high voltage induced the orientation of the water, which suggest that graphene's hydrophobic interaction with the water could stabilize the ice. Moreover, our EELS analysis of the water revealed an oxygen peak shifts to a higher energy site, compared to the normal water, indicating that the bonding distance between the water molecules is short. However, if only the short distance would contribute to produce the ice, water should turn into ice just by being sandwiched by graphene layers (although it could have done so in absence of electron beams), which is not consistent with what was observed experimentally.

There should be other factors contributing the stability of the ice. We then conjectured that one of the factors for stabilizing the ice was a single atom, such as gold which can stably enter into a hole existing in the hexagonal ice crystals. In other words, the electron beams not only vaporized water but also could have ejected the surface gold atoms into the water or onto the graphene, which might have triggered the transformation from the water to the ice. In our previously research, we confirmed that gold on graphene could have an unstable structure and could be easily vaporized by electron beams. Thus, the ejection of gold atoms probably occurred also in this case.

We show other TEM image and diffraction pattern that suggests transformation of ice in Figure 4-36(A) and 4-36(B). We found that this ice observed from [001] incident has hexagonal pattern of ice lattice agreement with Figure 4-36(A) and its FT image.

However in Figure 4-36(B), diffraction pattern suggests that there is no lattice regarding with (100) but circle pattern of (200) was observed. This phenomenon can be explained that lattice constant a and b of hexagonal ice observed in graphene layer has halved by the insertion of something of atoms. Figure 4-37(A) shows simulation image of electron diffraction pattern of gold and ice complex as shown in Figure 4-37(B) and 4-37(C).

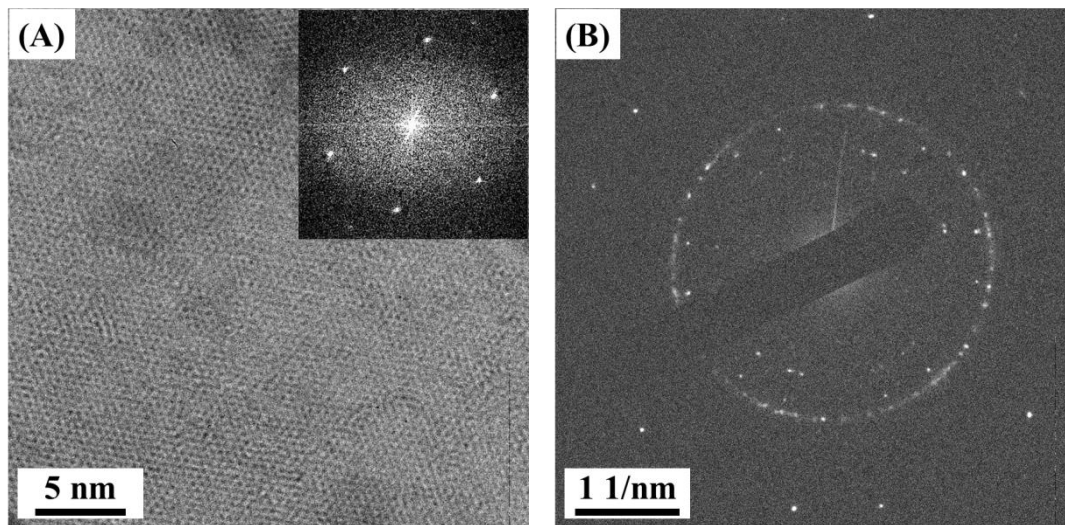


Figure 4-36 : High magnification TEM image of ice [001] incident and its electron diffraction image.

(A) High magnification TEM image of ice shows hexagonal patterns, which are identified with [001] incident of ice (1h). Insert image shows FT image and their pattern are consistent with (100), (010), and (1-10) surface of ice, which are determined on the basis of graphene lattice.

(B) The electron diffraction image of Fig. (A) A twin hexagonal patterns shows the graphene sandwiched structure which is made of two sheets of single-layer graphene. The d value of the circle pattern, which shows polycrystalline ice, is determined to (200) surface of ice (1h).

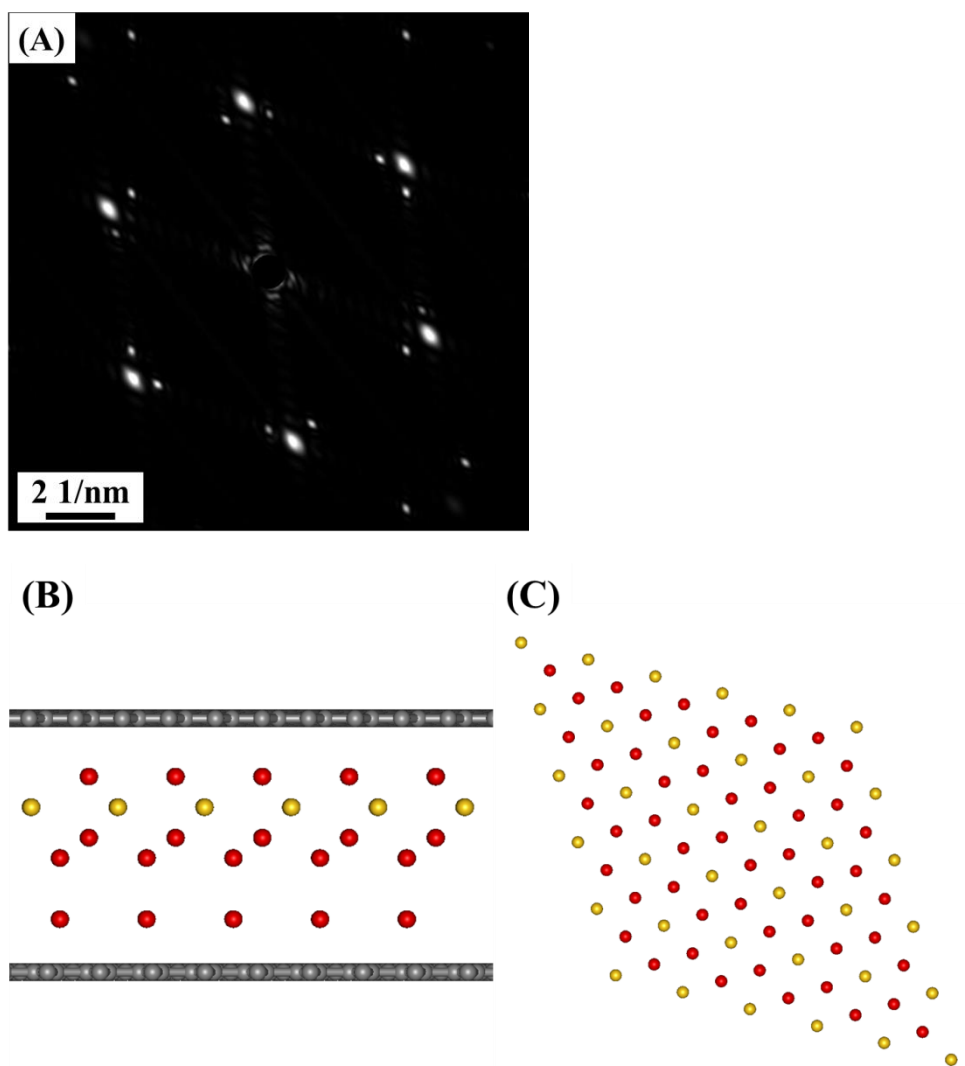


Figure 4-37 : The electron diffraction simulation image and its structural image of ice with gold encapsulated between graphene layers.

(A) The electron diffraction simulation image of ice with gold atoms. The original structural images of ice with gold encapsulated in graphene layers are shown in (B) and (C). Fig. (B) shows side view and Fig. (C) shows top view removed graphene layers in order to clarify the structure of ice with gold atoms. Red bolls exhibit oxygen atoms of ice and yellow bolls exhibit gold atoms. In these images, hydrogen atoms are omitted. In Fig. (A), twin hexagonal patterns show the graphene sandwiched structure which is made of two sheets of single-layer graphene and the d value of extraneous spots are consisted with the circle spots shown in Fig. 4(B).

The other TEM images as shown in Figure 4-38(A) and 4-38(B) support the above hypothesis, too. Figure 4-38(A) shows polycrystalline ice and 4-38(B) shows ice and gold nanocluster. We got Figure 4-38(B) after focusing electron beam to the center of image 4-38(A) in the same intensity as in Figure 4-34(B). We found that Figure 4-38(A) has flat contrast of ice lattice but Figure 4-38(B) has ice with dark contrasts came from gold clusters. Thus we guess gold clusters came from vaporized ice crystal. Gold atoms have hidden in the hole of hexagonal ice.

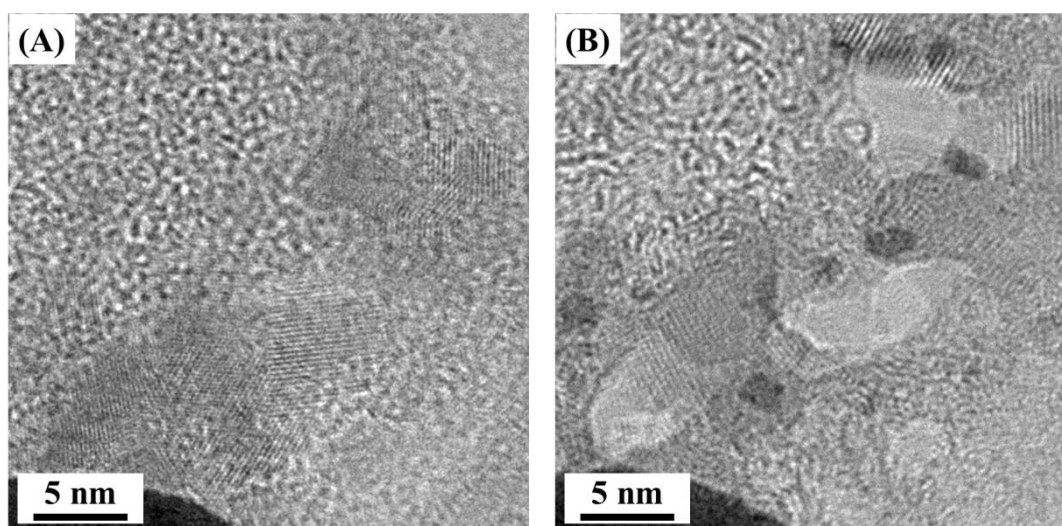


Figure 4-38 : High magnification TEM images of ice.

The fact that the spot which should be found in the electron beam diffraction image was absent can also be explained by the existence of gold in the hole of the ice crystals. In general, water molecules make a cluster when gathering around a core. However, in a system between graphene layers, a tight and hydrophobic space which enhances orientation of surface molecules, formation of clusters with a 3-dimensional and regular structure is difficult.

4-8. DFT calculation of ice with gold

The density functional method was used for the calculations. We studied the stability of the system by comparing the results of calculations conducted separately for hexagonal ice and gold with those for hexagonal ice with gold encapsulated in the space at the hexagonal lattice center. We used the Gaussian software for the DFT calculations, along with the 6-31G** and SDD basis functions for water and gold, respectively. We utilized B3LYP and PBE/PBE as exchange–correlation functionals. The speculated structure, in which gold atoms exist in ice, is shown in Figure 4-39; its atomic coordinates are reported in Table 2. The coordinates of the gold atoms were optimized using a basis function and exchange–correlation functional, although coordinates of hydrogen atoms did not converge because hydrogen atoms are delocalized in hexagonal ice.

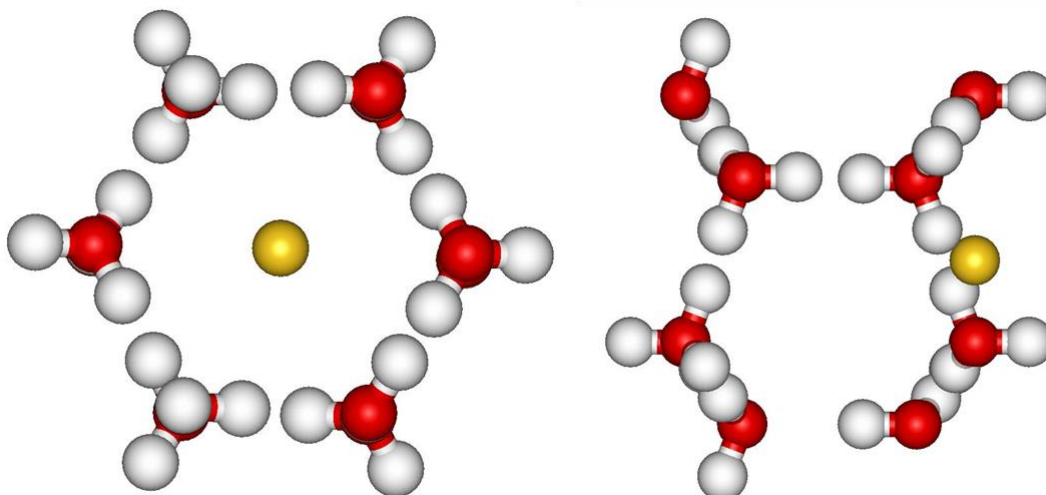


Figure 4-39: Structural model of water with a gold atom; the gold, oxygen, and hydrogen atoms

are shown as yellow, red, and white balls, respectively.

	x	y	z
H	0.4009	3.214	8.6554
H	4.9119	5.8184	6.0403
H	2.6564	1.9118	4.9824
H	0.4009	5.8184	4.9824
H	4.9119	3.214	2.3673
H	2.6564	7.1206	2.3673
H	4.9119	4.0396	7.4948
H	2.6564	7.9462	7.4948
H	2.6564	1.0862	7.2009
H	0.4009	4.9928	7.2009
H	1.9414	6.7078	7.4948
H	3.3713	2.3246	7.2009
H	1.1158	2.8012	7.4948
H	5.6268	2.8012	7.4948
H	-0.3141	6.2312	7.2009
H	4.1969	6.2312	7.2009
H	4.9119	4.9928	3.8218
H	0.4009	4.0396	3.5279
H	1.1158	6.2312	3.8218
H	5.6268	6.2312	3.8218
H	-0.3141	2.8012	3.5279
H	4.1969	2.8012	3.5279
H	1.9414	2.3246	3.8218
H	3.3713	6.7078	3.5279
O	0.4009	3.214	7.8052
O	4.9119	3.214	7.8052
O	2.6564	7.1206	7.8052
O	2.6564	1.9118	6.8905
O	0.4009	5.8184	6.8905
O	4.9119	5.8184	6.8905
O	2.6564	1.9118	4.1322

O	0.4009	5.8184	4.1322
O	4.9119	5.8184	4.1322
O	0.4009	3.214	3.2175
O	4.9119	3.214	3.2175
O	2.6564	7.1206	3.2175
Au	2.6564	4.5162	3.2175

Table 2 : Configuration atomic coordinate corresponding to Figure 4-39.

We obtained the total energies of the gold in ice as $-14,674$ eV and $-14,213$ eV. The sums of the energies of the ice with the same structure and gold were $-14,668$ eV and $-14,196$ eV. The difference energies of the gold in ice and the ice with gold were calculated as -6.16 eV and -16.9 eV, respectively, in each exchange–correlation functional. These results suggest that the gold in the ice crystal hole is stabilized.

We calculated the stability of gold in an ice structure by utilizing the VASP in the same Gaussian calculation. In this calculation, we utilized PBE-GGA and PBE-sol as the exchange–correlation functionals. The speculated structure is shown in Figure 4-40, and its configuration atomic coordinates are reported in Table 3. The coordinates were optimized using the exchange–correlation functional and a pseudo potential.

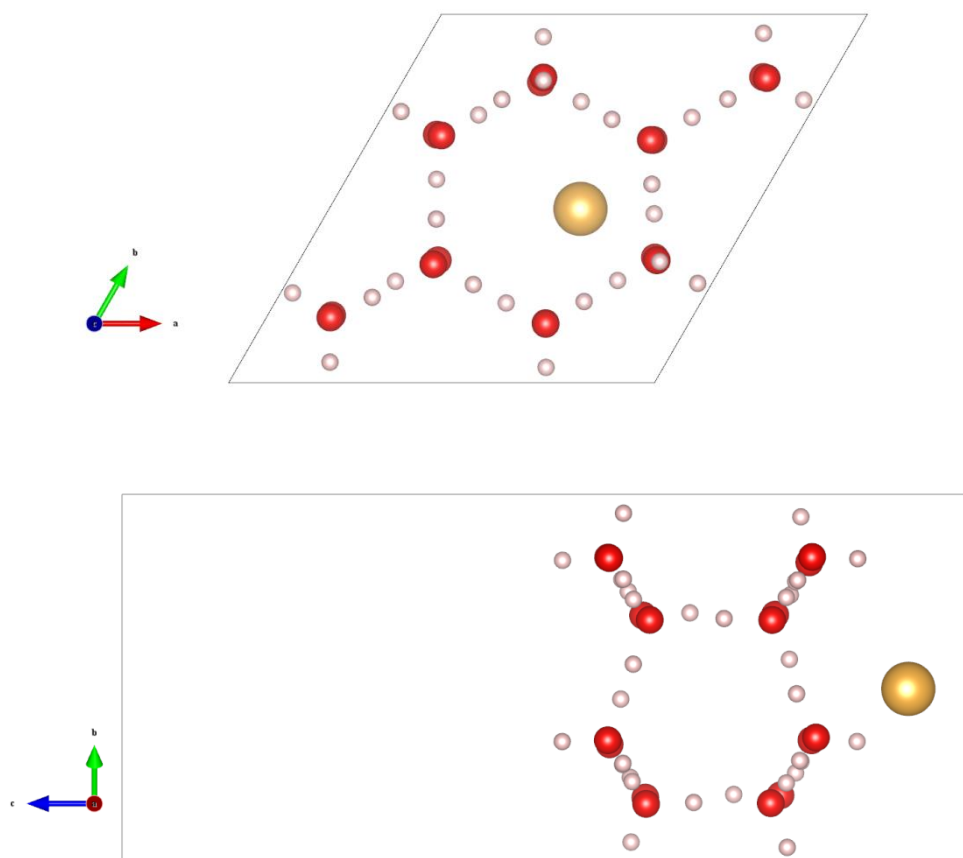


Figure 4-40: Structural model of water with a gold atom; the gold, oxygen, and hydrogen atoms are shown as yellow, red, and white balls, respectively. The box shows the unit cell.

	x	y	z
H	9.06369	2.57481	8.64146
H	6.70665	1.26043	5.92029
H	4.44845	5.25312	5.99308
H	2.10941	1.46556	5.15578
H	8.95787	5.13849	5.37534
H	4.55825	2.59283	2.61267
H	11.25978	6.43819	2.61525
H	6.66616	6.4007	8.64308
H	4.39433	3.47062	7.41049
H	11.2651	7.42212	7.36419
H	2.14356	0.41219	7.23702

H	8.9176	4.16282	7.20008
H	5.7327	5.96011	7.39756
H	10.50053	6.00456	7.35822
H	3.06107	1.81765	7.24592
H	7.51199	1.71466	7.24382
H	9.90544	2.08969	7.37062
H	5.19186	2.06954	7.38469
H	8.05273	5.56862	7.18792
H	3.61812	5.73571	7.29536
H	6.696	0.30405	4.03975
H	4.38616	4.26358	3.99111
H	8.93871	3.65792	3.89274
H	6.64794	7.28049	3.76277
H	9.78867	5.60141	4.03711
H	5.29046	5.64859	3.96976
H	8.12716	2.18299	3.82846
H	3.50036	2.16277	3.76723
H	1.33699	1.92873	3.81419
H	5.84764	1.70626	4.05727
H	7.46036	5.90173	3.8615
H	12.12768	5.9616	3.87542
O	9.01493	2.59029	7.67611
O	6.65684	6.45376	7.67028
O	4.32017	2.49901	7.62431
O	11.33558	6.45084	7.63496
O	2.13702	1.37154	6.93392
O	8.91104	5.13044	6.89363
O	6.68246	1.23121	6.94638
O	4.48791	5.22901	6.99959
O	2.16399	1.47012	4.15738
O	8.96647	5.10869	4.33365
O	6.70103	1.26593	4.35317
O	4.37709	5.22763	4.28791
O	8.89819	2.70293	3.45707
O	6.58817	6.31118	3.61194
O	4.42833	2.6023	3.57887

O	11.24573	6.46274	3.5853
Au	7.52458	3.54622	1.81774

Table 3 : Configuration atomic coordinate corresponding to Figure 4-40.

The total energies of gold in ice shown in figure 4-40 are -236.962 eV and -240.439 eV. By contrast, the total energies of the ice with a gold atom that is far from ice are -236.825 eV and -240.145 eV. The difference energy of gold in ice and ice with gold were calculated to be -0.13714 eV/unit cell and -0.292353 eV/unit cell. These results indicate that the ice was stabilized by the additional gold atom in each DFT calculation.

4-9. **Conclusion**

In conclusion, using TEM observations of nanosized droplets under high pressure, we demonstrated the possibility of graphene liquid cells and the viability of our sample preparation method. We confirmed that various solutions were encapsulated in graphene liquid cells. Some clusters were observed in aqueous solutions of iron nitride and calcium chloride. TEM observations revealed that iron nitride clusters repeatedly appear and disappear in the graphene liquid cell. By contrast, calcium chloride crystallizes as calcium chloride hexahydrate, which precipitates from saturated solution at 218–302 K. We estimated that the pressure of our graphene liquid cell, according to the van der Waals interaction of the graphene layers, is approximately 600–700 MPa. TEM observations of a trichloromethane-sandwiched liquid cell at room temperature suggested that the pressure inside the liquid cell was 600–790 MPa, consistent with our estimation.

Using TEM observations, electron diffraction, and elemental analysis by EELS and EDs, we observed the phase transition of water encapsulated inside graphene layers. Gold atoms diffused onto graphene via electron-beam irradiation functioned as nucleation sites for ice, which crystallized as hexagonal ice, I_h . Furthermore, we confirmed by DFT calculations that ice with gold should be stabilized compared to ice and gold.

4-10. **References**

- [1] M. H. Nielsen, D. Li, H. Zhang, S. Aloni, T. Han, C. Frandsen, J. Seto, J. F. Banfield, H. Cölfen, J. J. De Yoreo, *Microsc. Microanal.* **2014**, *20*, 425-436.
- [2] C. Wang, Q. Qiao, T. Shokuhfar, R. F. Klie, *Adv. Mater.* **2014**, *26*, 3410-3414.
- [3] J. M. Yuk, Q. Zhou, J. Chang, P. Ercius, A. P. Alivisatos, A. Zettl, *ACS Nano* **2015**.
- [4] J. M. Yuk, H. K. Seo, J. W. Choi, J. Y. Lee, *ACS nano* **2014**, *8*, 7478-7485.
- [5] J. Wu, W. Gao, J. Wen, D. J. Miller, P. Lu, J.-M. Zuo, H. Yang, *Nano Lett.* **2015**, *15*, 2711-2715.
- [6] M. Koshino, T. Tanaka, N. Solin, K. Suenaga, H. Isobe, E. Nakamura, *Science* **2007**, *316*, 853-853.
- [7] N. De Jonge, D. B. Peckys, G. Kremers, D. Piston, *Proc. Natl. Acad. Sci.* **2009**, *106*, 2159-2164.
- [8] H. Zheng, S. A. Claridge, A. M. Minor, A. P. Alivisatos, U. Dahmen, *Nano Lett.* **2009**, *9*, 2460-2465.
- [9] N. de Jonge, F. M. Ross, *Nature nanotech.* **2011**, *6*, 695-704.
- [10] K. Klein, I. Anderson, N. De Jonge, *JMic* **2011**, *242*, 117-123.
- [11] J. M. Yuk, J. Park, P. Ercius, K. Kim, D. J. Hellebusch, M. F. Crommie, J. Y. Lee, A. Zettl, A. P. Alivisatos, *Science* **2012**, *336*, 61-64.
- [12] J. Park, H. Zheng, W. C. Lee, P. L. Geissler, E. Rabani, A. P. Alivisatos, *Acs Nano* **2012**, *6*, 2078-2085.
- [13] R. Ludwig, *Angew. Chem. Int. Ed.* **2001**, *40*, 1808-1827.
- [14] A. I. Kolesnikov, J.-M. Zanotti, C.-K. Loong, P. Thiyagarajan, A. P. Moravsky, R. O. Loutfy, C. J. Burnham, *Phys. Rev. Lett.* **2004**, *93*, 035503.
- [15] M. Yoshizawa, T. Kusukawa, M. Kawano, T. Ohhara, I. Tanaka, K. Kurihara, N. Niimura, M. Fujita, *J. Am. Chem. Soc.* **2005**, *127*, 2798-2799.
- [16] Y. Maniwa, K. Matsuda, H. Kyakuno, S. Ogasawara, T. Hibi, H. Kadowaki, S. Suzuki, Y. Achiba, H. Kataura, *Nat Mater* **2007**, *6*, 135-141.
- [17] D. Takaiwa, I. Hatano, K. Koga, H. Tanaka, *Proc. Natl. Acad. Sci.* **2008**, *105*, 39-43.
- [18] X. Lin, A. Groß, *Surf Sci.* **2012**, *606*, 886-891.
- [19] T. Tokushima, Y. Horikawa, O. Takahashi, H. Arai, K. Sadakane, Y. Harada, Y. Takata, S. Shin, *PCCP* **2014**, *16*, 10753-10761.
- [20] M. Watkins, D. Pan, E. Wang, A. Michaelides, J. VandeVondele, B. Slater, *Nature materials* **2011**, *10*, 794-798.
- [21] J. Gustafsson, G. Arvidson, G. Karlsson, M. Almgren, *Biochimica et Biophysica*

- Acta (BBA)-Biomembranes* **1995**, *1235*, 305-312.
- [22] C. L. Jackson, H. D. Chanzy, F. P. Booy, B. J. Drake, D. A. Tomalia, B. J. Bauer, E. J. Amis, *Macromolecules* **1998**, *31*, 6259-6265.
- [23] R. H. Somani, B. S. Hsiao, A. Nogales, S. Srinivas, A. H. Tsou, I. Sics, F. J. Balta-Calleja, T. A. Ezquerra, *Macromolecules* **2000**, *33*, 9385-9394.
- [24] J. L. Milne, M. J. Borgia, A. Bartesaghi, E. E. Tran, L. A. Earl, D. M. Schauder, J. Lengyel, J. Pierson, A. Patwardhan, S. Subramaniam, *FEBS J.* **2013**, *280*, 28-45.
- [25] S. Helvig, I. D. Azmi, S. M. Moghimi, A. Yagmur, *AIMS Biophysics* **2015**, *2*, 116-130.
- [26] T. Sasaki, H. Sawada, F. Hosokawa, Y. Sato, K. Suenaga, *Ultmi* **2014**, *145*, 50-55.
- [27] D. Parsons, *Science* **1974**, *186*, 407-414.
- [28] K. L. Liu, C. C. Wu, Y. J. Huang, H. L. Peng, H. Y. Chang, P. Chang, L. Hsu, T. R. Yew, *Lab Chip* **2008**, *8*, 1915-1921.
- [29] G. Algara-Siller, O. Lehtinen, F. Wang, R. Nair, U. Kaiser, H. Wu, A. Geim, I. Grigorieva, *Nature* **2015**, *519*, 443-445.
- [30] W. Zhou, K. Yin, C. Wang, Y. Zhang, T. Xu, A. Borisevich, L. Sun, J. C. Idrobo, M. F. Chisholm, S. T. Pantelides, *Nature* **2015**, *528*, E1-E2.
- [31] Y. Sasaki, R. Kitaura, Y. Yamamoto, S. Arai, S. Suzuki, Y. Miyata, H. Shinohara, *Appl. Phys. Express* **2012**, *5*, 065103.
- [32] U. Bergmann, P. Wernet, P. Glatzel, M. Cavalleri, L. G. M. Pettersson, A. Nilsson, S. P. Cramer, *PhRvB* **2002**, *66*.
- [33] T. Tokushima, Y. Harada, O. Takahashi, Y. Senba, H. Ohashi, L. G. Pettersson, A. Nilsson, S. Shin, *Chem. Phys. Lett.* **2008**, *460*, 387-400.
- [34] C. Colliex, T. Manoubi, C. Ortiz, *PhRvB* **1991**, *44*, 11402-11411.
- [35] E. C. Todd, D. M. Sherman, J. A. Purton, *Geochim. Cosmochim. Acta* **2003**, *67*, 2137-2146.
- [36] H. Shuman, A. P. Somlyo, *Ultmi* **1987**, *21*, 23-32.
- [37] J. K nstler, S. Seifert, T. Reich, H. Funke, B. Johannsen, in *Workshop Proceedings Grenoble, France*, pp. 10-12.
- [38] H. Shimizu, K. Matsumoto, *The Journal of Physical Chemistry* **1984**, *88*, 2934-2936.
- [39] K. F. Dziubek, A. Katrusiak, *The Journal of Physical Chemistry B* **2008**, *112*, 12001-12009.
- [40] B. A. Sexton, *Surf Sci.* **1981**, *102*, 271-281.

List of publications

Supplemental publications

1) Yuki Sasaki¹, Ryo Kitaura¹, Jong Min Yuk^{2,3,4}, Alex Zettl^{2,3,4} and Hisanori Shinohara¹, Efficient preparation of graphene liquid cell utilizing direct transfer with large-area well-stitch graphene, *Chem. Phys. Lett.*, accepted.

2) Y. Sasaki¹, R. Kitaura², S. Arai³, K. Yamamoto⁴, S. Suzuki¹, Y. Miyata⁵ and H. Shinohara⁶, Preparation and Observation of an Atomic Layer of Gold Formed on the Surface of Graphene, *Appl. Phys. Express*, 5, 065103, (2012).

Reference publication

1) P. W. Dunk¹, N. K. Kaiser², C. L. Hendrickson^{1,2}, J. P. Quinn², C. P. Ewels³, Y. Nakanishi⁴, Y. Sasaki⁴, H. Shinohara⁴, A. G. Marshall^{1,2}, and H. W. Kroto¹, Closed network growth of fullerenes, *Nature Communications*, 3,855, (2012).